

Signal-Processing Theory for the TurboRogue Receiver

J. B. Thomas

April 1, 1995



National Aeronautics and
Space Administration
Jet Propulsion Laboratory
California Institute of Technology
Pasadena, California

(NASA-CR-198882) SIGNAL-PROCESSING
THEORY FOR THE TURBOROGUE RECEIVER
(JPL) 97 p

N95-30581

Unclass

G3/32 00566666

*11-22-CR
56666
p. 94*

JPL Publication 95-6

Signal-Processing Theory for the TurboRogue Receiver

J. B. Thomas

April 1, 1995



National Aeronautics and
Space Administration

Jet Propulsion Laboratory
California Institute of Technology
Pasadena, California

The research described in this publication was carried out by the Jet Propulsion Laboratory, California Institute of Technology, under a contract with the National Aeronautics and Space Administration.

Reference herein to any specific commercial product, process, or service by trade name, trademark, manufacturer, or otherwise, does not constitute or imply its endorsement by the United States Government or the Jet Propulsion Laboratory, California Institute of Technology.

ACKNOWLEDGMENTS

The author is grateful to T. P. Yunck and C. E. Dunn for their helpful suggestions after reading a preliminary version of this report and to Diana Meyers for her skillful editing in producing the final report. D. J. Spitzmesser collaborated in the design of the analog front end. The TurboRogue receiver was implemented in a collaborative effort by JPL and Allen Osborne Associates.

ABSTRACT

Signal-processing theory for the TurboRogue receiver is presented. The signal form is traced from its formation at the GPS satellite, to the receiver antenna, and then through the various stages of the receiver, including extraction of phase and delay. The analysis treats the effects of ionosphere, troposphere, signal quantization, receiver components, and system noise, covering processing in both the "code mode" when the P code is not encrypted and in the "P-codeless mode" when the P code is encrypted. As a possible future improvement to the current analog front end, an example of a highly digital front end is analyzed.

SYMBOL DEFINITIONS

Roman

- A_-, A_0, A_+ = early, prompt, and late correlation amplitudes, measured
- A_c = amplitude factor defined in Eq. (4.23)
- A_m = maximum correlation amplitude, Eq. (7.1) or Eq. (7.20)
- a_n = P-code chip value, ± 1
- $A_p(f)$ = P-code Fourier component, Eq. (2.6)
- A_x = amplitude factor defined by Eq. (5.7)
- \tilde{C} = quantized counterrotation phasor, Eq. (4.2)
- c_1 = coefficient of fundamental in quantized counterrotation sinusoid
- f = frequency
- f_d = Doppler-shifted baseband frequency
- f_h = nominal downconversion frequency
- f_L = L-band carrier frequency
- f_p = P-code chip rate = $1/T_p$
- $G_A(v_d)$ = effective complex filter introduced by antenna
- $G(f)$ = composite bandpass amplitude, Eq. (3.12)
- $G_R(f_d)$ = effective aggregate complex filter introduced by receiver before sampler
- $G_S(f)$ = effective aggregate filter introduced by GPS satellite
- $H(f, f')$ = definition in Eq. (4.16)
- k_B = Boltzmann's constant
- k_p = constant in equation to convert from correlation amplitudes to residual delay
- l = lag offset relative to model delay
- L_c = SNR loss due to quantization of counter-rotation sums, Eq. (7.6)
- L_s = SNR loss due to sampling quantization, Eq. (7.7)

L_x	=	model delay offsetting L1 during cross-correlation of L1 and L2
N	=	$(N_S - 1)/2$
N_c	=	number of chips in accumulation
N_s	=	number of sample points in accumulation interval
$P(t)$	=	P-code sequence
P_N	=	average noise power entering the sampler, per quadrature component
P'_N	=	total noise power at RF at insertion
P_S	=	average baseband signal power per quadrature component before receiver filtering
q_M	=	proportionality constant accounting for sampling quantization in low-SNR limit
R_{cx}	=	ratio of code and P-codeless SNRs, Eq. (7.26)
$\bar{R}_p(\tau)$	=	time-averaged P-code autocorrelation function, Eq. (2.14)
$R_p(t, \tau)$	=	autocorrelation function for P code, Eq. (2.12)
s	=	sample interval = $(20.456)^{-1} \mu s$
S_c	=	definition in Eq. (4.8)
$S_I(t)$	=	ideal unfiltered L-band signal, Eq. (2.15)
SNR_{20}	=	"18-ms" voltage SNR
SNR_V	=	voltage SNR, Eq. (7.5)
SNR_x	=	maximum voltage SNR for L1*L2 correlation, Eq. (7.23)
$S_p(f)$	=	P-code power spectrum, Eq. (2.11)
$S_R(t)$	=	signal received by the TR antenna, Eq. (2.19)
$S_T(t)$	=	transmitted L-band signal, Eq. (2.18)
S_x	=	definition of Eq. (5.4)
T	=	accumulation interval
t	=	true time
\bar{t}	=	true time at interval center

T_p	=	$(10.23)^{-1} \mu\text{s}$ = P-code chip interval
t_R	=	receiver time as indicated by sampler
T_s	=	system temperature
$u_l(t_R)$	=	correlation sum, Eq. (4.5)
\tilde{V}_k	=	quantized baseband voltage representing signal after sampling, $k = 1$ for L1 and $k = 2$ for L2
$V_m(t_R, l)$	=	model signal generated by receiver, Eq. (4.1)
$V(t)$	=	complex voltage representing signal at baseband, Eq. (3.2)
W	=	effective double-sided noise bandwidth
\tilde{x}	=	quantized value for quantity x
x_1, x_2	=	quantity x for L1 and L2, respectively

Greek

α_f	=	loss in signal power due to receiver filtering
$\Delta\phi_I$	=	difference of instrumental phase between L1 and L2, defined by Eq. (5.5)
$\overline{\Delta\phi_I}$	=	bandpass average of $\Delta\phi_I$
η	=	noise added to signal, at baseband before sampler
$\Lambda(\tau)$	=	triangle function
σ_A	=	1- σ amplitude error, Eq. (7.15)
σ_n	=	RMS noise on either component of baseband signal before sampling
σ_τ	=	1- σ delay error, Eq. (7.19) or Eq. (7.20)
σ_u	=	1- σ error on correlation sum
σ_ϕ	=	1- σ system-noise error in phase, Eq. (7.14)
τ	=	combined delay, Eq. (2.20)
τ'	=	combined delay, Eq. (3.7)

$\hat{\tau}$	=	measured value for total delay, Eq. (6.9)
τ_a	=	aggregate group delay, Eq. (3.14)
τ_e	=	group delay due to ionosphere
τ_g	=	geometric delay from satellite to receiver
τ_I	=	composite instrumental group delay
τ_m	=	model group delay generated by receiver
τ_{p2}	=	actual value for P2 group delay derived from P2-P1 group delay, Eq. (6.24)
$\hat{\tau}_{p2}$	=	measured value for P2 group delay derived from P2-P1 group delay, Eq. (6.23)
τ_r	=	residual delay = difference of aggregate group delay and model delay, Eq. (4.24) and Eq. (5.9)
τ_R	=	error in receiver clock relative to true time, Eq. (3.5)
$\hat{\tau}_r$	=	measured value for residual delay, Eq. (6.7)
τ_s	=	error in GPS satellite clock relative to true time
τ_t	=	tropospheric delay
τ_ϕ	=	actual value for phase delay, Eq. (6.6)
$\hat{\tau}_\phi$	=	measured value for phase delay, Eq. (6.5)
τ'_ϕ	=	aggregate phase delay, Eq. (3.16)
τ^x_ϕ	=	actual value for L2 phase delay derived from L1*L2 phase, Eq. (6.19)
$\hat{\tau}^x_\phi$	=	measured value for L2 phase delay derived from L1*L2 phase
$\hat{\tau}_x$	=	measured value for total P2-P1 group delay, Eq. (6.20)
τ_x	=	actual value for total P2-P1 group delay, Eq. (6.21)
ν_d	=	Doppler-shifted frequency at RF, Eq. (3.3)
ϕ	=	actual value for total carrier phase, Eq. (6.4)
$\hat{\phi}$	=	measured value for total carrier phase, Eq. (6.3) or Eq. (6.11)

- φ_a = aggregate baseband carrier phase, Eq. (3.15)
- φ_d = difference of aggregate baseband phase and model phase, Eq. (4.10) or Eq. (5.8)
- φ_e = ionospheric phase shift
- φ_h = downconversion phase, Eq. (3.1)
- φ_{hd} = drift in downconversion phase relative to f_{ht} , Eq. (3.1)
- φ_I = composite instrumental phase shift excluding τ_I term
- $\overline{\varphi_I}$ = bandpass average of φ_I
- $\hat{\varphi}_{L1}^C$ = measured value for total C/A carrier phase
- φ_{L2}^x = actual value for total L2 carrier phase derived from L1*L2 carrier phase and C/A carrier phase, Eq. (6.17)
- $\hat{\varphi}_{L2}^x$ = measured value for total L2 carrier phase derived from L1*L2 carrier phase and C/A carrier phase, Eq. (6.16)
- φ_m = model carrier phase generated by receiver
- $\hat{\varphi}_r$ = measured value for residual phase, Eq. (6.1)
- φ_s = phase instability introduced by satellite, excluding frequency reference
- φ_x = actual value for L1*L2 carrier phase, Eq. (6.14)
- $\hat{\varphi}_x$ = measured value for L1*L2 carrier phase, Eq. (6.13)
- ψ = "correction" term in φ_{L2}^x , Eq. (6.18)

Other

- $\langle \rangle$ = ensemble average over both noise and code
- $\langle \rangle_\eta$ = ensemble average over noise, η
- $\langle \rangle_p$ = ensemble average over possible code values

CONTENTS

Section	Page
1 INTRODUCTION	1-1
2 THE GPS SIGNAL	2-1
2.1 Ideal P Code	2-1
2.2 Spectral Analysis of the Ideal P Code	2-3
2.3 Autocorrelation of the Ideal P Code	2-4
2.4 The Received Signal	2-5
3 FRONT-END PROCESSING	3-1
3.1 Functional Description of the Analog Front End	3-1
3.2 Mathematical Model for the Analog Front End	3-1
3.3 Mathematical Model for the Sampled Signal	3-5
3.4 Reformulation of the Sampled Signal	3-6
4 CORRELATION IN THE CODE MODE	4-1
4.1 Model Signal	4-1
4.2 Correlation Sum	4-2
4.3 Correlation Function	4-2
4.4 Discussion of the Correlation Function	4-7
5 CROSS-CORRELATION IN THE P-CODELESS MODE	5-1
5.1 Correlation Sum	5-1
5.2 Correlation Function	5-2
5.3 Discussion of the L1*L2 Correlation Function	5-3
6 OBSERVABLE EXTRACTION	6-1
6.1 Code Mode	6-1
6.1.1 Phase Extraction	6-1
6.1.2 Delay Extraction	6-2

6.2	P-Codeless Mode	6-3
6.2.1	Phase Extraction	6-3
6.2.2	Delay Extraction	6-5
7	SYSTEM-NOISE ANALYSIS	7-1
7.1	Code Mode	7-1
7.1.1	Signal-to-Noise Ratio	7-1
7.1.2	System-Noise Error in Phase	7-3
7.1.3	System-Noise Error in Group Delay	7-4
7.2	P-Codeless Mode	7-5
7.2.1	Signal-to-Noise Ratio	7-5
7.2.2	System-Noise Error in Phase	7-7
7.2.3	System-Noise Error in Delay	7-7

Appendices

A	Example of a Highly Digital Front End	A-1
B	Quantization Effects	B-1
C	Noise-Correlation Analysis	C-1
D	Quadrature Noise Statistics	D-1
E	The C/A Correlation Function	E-1

Figures

2-1	Illustration of the Autocorrelation of a P-Chip Sequence	2-2
2-2	The P-Chip Function	2-3
2-3	The Time-Averaged Autocorrelation Function for the P Code	2-6
3-1	Block Diagram for the Analog Front End	3-2
3-2	Amplitude and Phase Response of the TurboRogue Baseband Butterworth Filter	3-3
4-1	Schematic Illustration of the $\text{sinc}_x/\text{sinc}_y$ Functions	4-5
4-2	P-Code Correlation Function for the TurboRogue Receiver with the Analog Front End	4-8
4-3	Code-Noise-Free C/A-code Correlation Function for the TurboRogue Receiver With the Analog Front End	4-10

5-1	L1*L2 Correlation Function for the TurboRogue Receiver With the Analog Front End	5-5
6-1	Table Lookup Operations for the L1*L2 Delay	6-6
6-2	Table Lookup Function for the L1*L2 Delay	6-7
A-1	Block Diagram for the Example of a Highly Digital Front End	A-2
A-2	Schematic Illustration of Quadrature Sampling Downconversion of a Sinusoid.....	A-4
A-3	Schematic Illustration of Sampling Downconversion in the Frequency Domain	A-5
B-1	Quantization Functions for Two-level and Three-level Quantization	B-2
B-2	The Three-level Counterrotation Sinusoids	B-9
E-1	Power Spectrum of the C/A Code for Satellite 1, with 1-kHz Spacing	E-5
E-2	Power Spectra of the C/A Code for Satellites 1, 15, and 22, with 35-kHz Resolution	E-6
E-3	C/A Correlation Amplitude vs. Lag for Satellites 1, 15, and 22, Referenced to Code-Noise Free Response	E-7

SECTION 1

INTRODUCTION

This report presents the nonrelativistic theory for signal processing in the TurboRogue (TR) receiver. The signal form is traced from the Global Positioning System (GPS) satellite to the receiver antenna, and then through the various stages in the receiver, including extraction of phase and delay. The analysis includes the effects of the ionosphere, the troposphere, discrete sampling, instrumentation, and system noise. The theory covers processing in the "code mode" when the P code is known and in the "P-codeless mode" when the P code is encrypted.

Section 2 analyzes the GPS signal by performing a spectral decomposition and autocorrelation of the ideal P code and propagating the signal from the GPS spacecraft to the receiver, with the inclusion of both troposphere and ionosphere effects. Section 3 analyzes receiver front-end processing, tracing the signal from reception at RF to sampled form at baseband. Section 4 presents correlation theory for the code mode when the sampled signal is cross-correlated with a model signal generated by the receiver on the basis of feedback in phase and delay. Section 5 presents correlation theory for the P-codeless mode in which the L1 and L2 signals are cross-correlated. Section 6 describes extraction of the phase and delay observables in both the code mode and P-codeless mode and presents the corresponding theoretical expressions containing the various terms contributing to each observable. Section 7 analyzes the effects of system noise, including signal-to-noise ratios (SNRs), phase errors, and delay errors for both the code mode and the P-codeless mode.

As an example of a possible future improvement to the current analog front end, Appendix A presents the theory for a particular design of a highly digital front end. Appendix B analyzes the effects of two-level and three-level quantization in the analog-to-digital conversion of the received signal and of three-level quantization of the counterrotation sinusoids. Appendix C presents noise correlation analysis, including correlation of noise between samples and correlation of noise on correlation sums with different lags. Appendix D analyzes the correlation of noise between the quadrature components of the baseband signal. Appendix E formulates the correlation function for the clear/acquisition (C/A) channel.

SECTION 2

THE GPS SIGNAL

2.1 Ideal P Code¹

The ideal, unfiltered P code, which is generated at a rate of $f_p = 10.23$ MHz, consists of a pseudorandom sequence of chips, each with a value -1 or +1 and a width of $T_p = 1/f_p = (10.23)^{-1} \mu\text{s}$, as illustrated by plot (a) in Fig. 2-1. A particular P-code sequence can be expressed in its ideal form as

$$P(t) = \sum_n a_n B(t-t_n) \quad (2.1)$$

where the time argument t is true time, $B(t)$ is the chip function shown in Fig. 2-2, and the coefficients a_n are the chip values of -1 or +1. As indicated by Eq. (2.1), the chip centers fall at true-time values t_n , which are equally spaced and given by

$$t_n = n T_p - \frac{T_p}{2} \quad (2.2)$$

in which n is an integer whose range is sufficient to cover the time interval of interest. As implied in this time relation, the rising edge of a chip that falls at an integer-second boundary will be aligned with that boundary when the GPS clock has zero error with respect to true time. Satellite clock error will be accounted for below.

The chip values a_n will be approximated as random variables with zero mean:

$$\langle a_n \rangle_p = 0 \quad (2.3)$$

and with no correlation between different chips:

$$\langle a_j a_n \rangle_p = \delta_{jn} \quad (2.4)$$

where $\langle \rangle_p$ indicates an ensemble average over possible chip values and δ_{jn} is the Kronecker delta function. A given P-code sequence is generated for one week before the sequence is repeated. As developed below, the code sequences leaving the GPS satellites do not have the ideal form in Eq. (2.1) but are filtered to some degree.

An expression similar to Eq. (2.1) also describes a C/A-code sequence with its chip width of $(1.023)^{-1} \mu\text{s}$ and a sequence repetition interval of a millisecond. With regard to correlation analysis, processing of the P and C/A data are very similar. As outlined in Appendix E, however, the short (1-ms) repetition interval for the C/A sequences becomes a complication, but most aspects of the results remain the same.

¹ For an explanation of symbols used in this document, see page v, "Symbol Definitions."

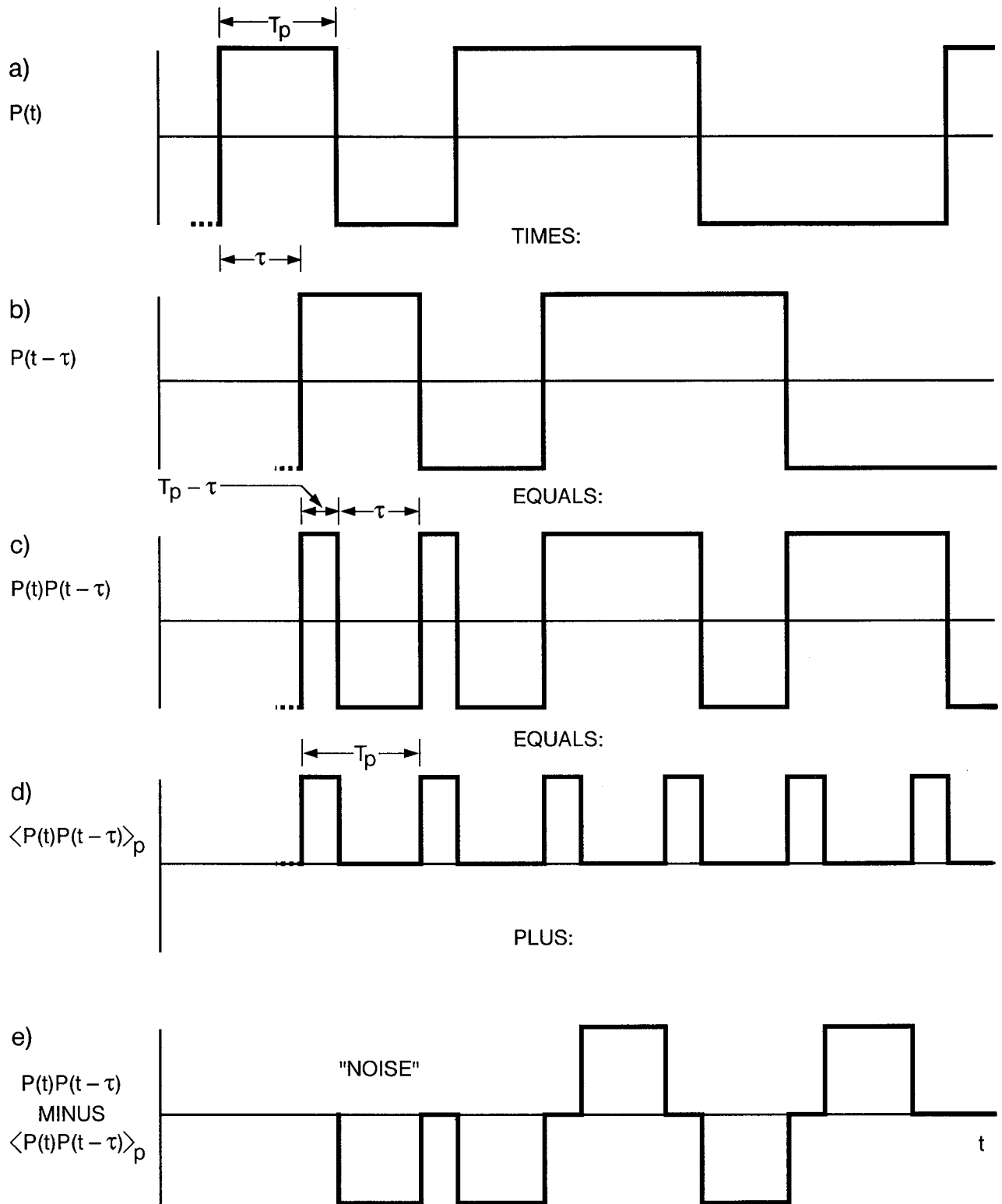


Figure 2-1. Illustration of the Autocorrelation of a P-Chip Sequence

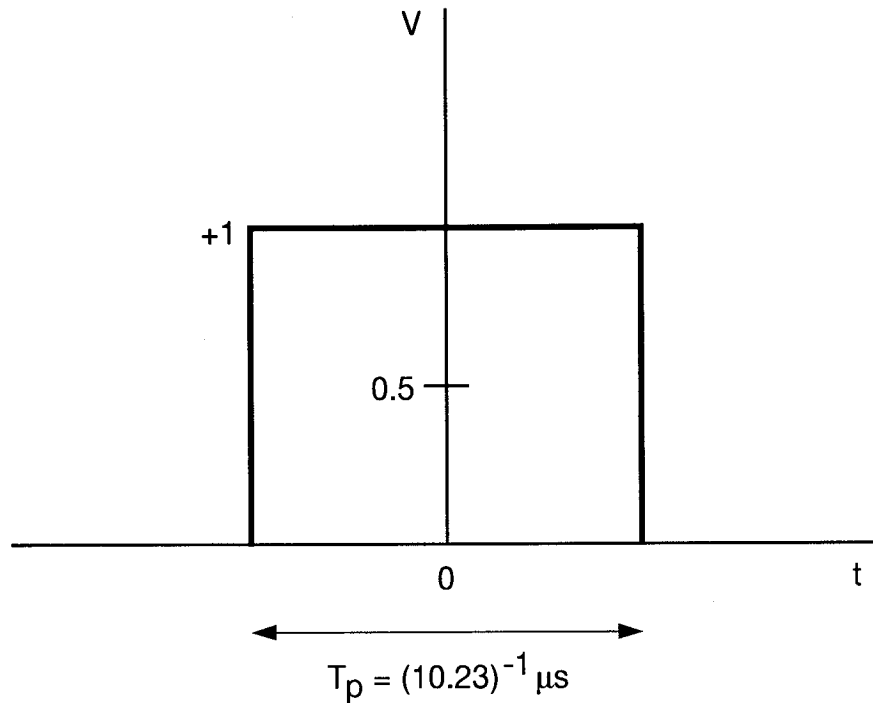


Figure 2-2. The P-Chip Function

2.2 Spectral Analysis of the Ideal P Code

A Fourier transform of a given P-code sequence, over the chips in an "accumulation interval" with center at true time t and length T , is given by

$$A_p(f) = \int_{t-T/2}^{t+T/2} P(t) e^{-2\pi i f t} dt \quad (2.5)$$

As assumed below, the accumulation interval will correspond to a correlation interval (e.g., 18 ms) applied during data reduction. With the use of Eq. (2.1), the transform is given to excellent approximation by

$$A_p(f) = T_p \frac{\sin(\pi f T_p)}{\pi f T_p} \sum_k^{N_c} a_k e^{-2\pi i f t_k} \quad (2.6)$$

where the sum over k applies only to chips within the transform interval and N_c is the total number of chips in the interval. (A box will be used to enclose equations of particular significance.) This equation is not exact since the two end chips in the transform interval may not fall completely in the interval. This effect is negligible since the interval contains so many chips (e.g., about 180,000 in 18 ms). The frequency components will vary from correlation

interval to correlation interval as a function of the particular values for a_k (i.e., the particular P-code sequence within the interval), but will have zero mean over many intervals. The power spectrum, however, averages to a $(\sin x/x)^2$ form, as shown below.

Based on Eq. (2.6), the correlation between spectral components at different frequencies is given by

$$\langle A_p^*(f) A_p(f') \rangle_p = T_p^2 \frac{\sin(\pi f T_p)}{\pi f T_p} \frac{\sin(\pi f' T_p)}{\pi f' T_p} \sum_{j,k} \langle a_j a_k \rangle_p e^{2\pi i(f t_j - f' t_k)} \quad (2.7)$$

By using the assumption in Eq. (2.4) and the definition of t_k in Eq. (2.2), one obtains

$$\langle A_p^*(f) A_p(f') \rangle_p = T_p^2 \frac{\sin(\pi f T_p)}{\pi f T_p} \frac{\sin(\pi f' T_p)}{\pi f' T_p} e^{\pi i(f-f)T_p} \sum_k^{N_c} e^{2\pi i(f-f')k T_p} \quad (2.8)$$

One can show that the sum becomes

$$e^{\pi i(f-f)T_p} \sum_k^{N_c} e^{2\pi i(f-f')k T_p} = e^{2\pi i(f-f')\bar{t}} \frac{\sin[N_c \pi(f-f')T_p]}{\sin[\pi(f-f')T_p]} \quad (2.9)$$

where \bar{t} is true time at the middle of the interval. This equation can be substituted in Eq. (2.8) to yield

$$\langle A_p^*(f) A_p(f') \rangle_p = T_p^2 e^{2\pi i(f-f')\bar{t}} \frac{\sin(\pi f T_p)}{\pi f T_p} \frac{\sin(\pi f' T_p)}{\pi f' T_p} \frac{\sin[N_c \pi(f-f')T_p]}{\sin[\pi(f-f')T_p]} \quad (2.10)$$

One can show (see Subsection 4.3) that the $\sin x/\sin y$ function can be accurately approximated by a sum of Dirac delta functions with a spacing of 10.23 MHz, provided N_c is very large. Thus, the correlation between frequency components is substantial only when $f - f' = n * 10.23$ MHz, where n is an integer.

The power spectrum is obtained by setting $f = f'$, which gives

$$S_p(f) = T_p \Gamma \left[\frac{\sin(\pi f T_p)}{\pi f T_p} \right]^2 \quad (2.11)$$

where the total accumulation time is given by $T = N_c T_p$. Thus, on average, the power spectrum of the ideal P code is a $(\sin x/x)^2$ function with a first zero crossing at $(T_p)^{-1}$.

2.3 Autocorrelation of the Ideal P Code

The autocorrelation function of the ideal P code is defined by

$$R_p(t, \tau) \equiv \langle P(t)P(t+\tau) \rangle_p \quad (2.12)$$

Autocorrelation of an example P-code sequence is illustrated in Fig. 2-1. Plot (b) offsets the P-code sequence in plot (a) by a selected delay τ , while plot (c) shows the product of plot (a) and plot (b). Plot (d) shows the autocorrelation function obtained by averaging plot (c) over all possible P-code sequences. Plot (e) shows the particular "noise" sequence that separates plot (c) from plot (d). As implied, the "noise" sequence averages to zero over all possible P-code sequences.

For $0 < \tau < T_p$, the autocorrelation function has a period T_p as a function of time and a value of either 0 or 1, as illustrated in plot (d) for a particular value of τ . For $\tau = 0$, the autocorrelation function in plot (d) would be 1.0 at all times. For $\tau > T_p$, the autocorrelation function would be zero.

Averaging over a time interval containing a very large number of chips produces the time-averaged autocorrelation function

$$\bar{R}_p(\tau) \equiv \frac{1}{T} \int_{-T/2}^{T/2} R_p(t, \tau) dt \quad (2.13)$$

Since the width of the positive pulses in plot (d) decreases as τ increases according to $T_p - \tau$, the time-averaged autocorrelation function becomes

$$\boxed{\bar{R}_p(\tau) = \Lambda(\tau)} \quad (2.14)$$

where $\Lambda(\tau)$ is the triangle function shown in Fig. 2-3. The Fourier transform of a triangle function is $(\sin x/x)^2$ function like that in Eq. (2.11), as one would expect.

If all P-code frequency components were present in the signal (i.e., an ideal P code), this exact triangle function would describe the amplitude response produced by correlating the received GPS signal with an ideal model code. As shown below, filtering modifies the triangle response and smooths the sharp corners.

2.4 The Received Signal

This subsection develops the spectral form of the GPS signal arriving at the receiver, including geometric, tropospheric, and ionospheric effects.

The form for the ideal unfiltered P code is given by Eq. (2.1). When modulated on an ideal carrier at L band, the ideal P signal becomes

$$S_1(t) = P(t) \cos(2\pi f_L t) \quad (2.15)$$

where f_L is the L-band frequency. The L2 signal is constructed solely of a P signal of this form while the L1 signal is a sum of such a P component and a similar C/A component. The C/A component is the same form as Eq. (2.15), but has a C/A pseudorandom sequence in place of $P(t)$ and a carrier 90° out of phase with the P component (see Eq. (E.14) in Appendix E of this

document). The C/A component is transmitted with a power nominally 3 dB greater than the L1-P component.

The spectral decomposition of the P code can be written as

$$P(t) = \int_{-\infty}^{\infty} A_p(f) e^{2\pi i f t} df \quad (2.16)$$

where the Fourier components are given in Eq. (2.6). This expression can be used to recast the ideal unfiltered L-band signal in Eq. (2.15) in the form

$$S_I(t) = \int_{-\infty}^{\infty} A_p(f) e^{2\pi i (f_L + f)t} df + \text{c.c.} \quad (2.17)$$

where c.c. denotes complex conjugate of the first term. The relation, $A_p^*(f) = A_p(-f)$, which is valid for a real signal like $P(t)$, has been used to obtain this formulation. In addition, an amplitude factor of 1/2 has been neglected since subsequent signal amplification at the spacecraft will lead to an overall gain factor as modeled below.

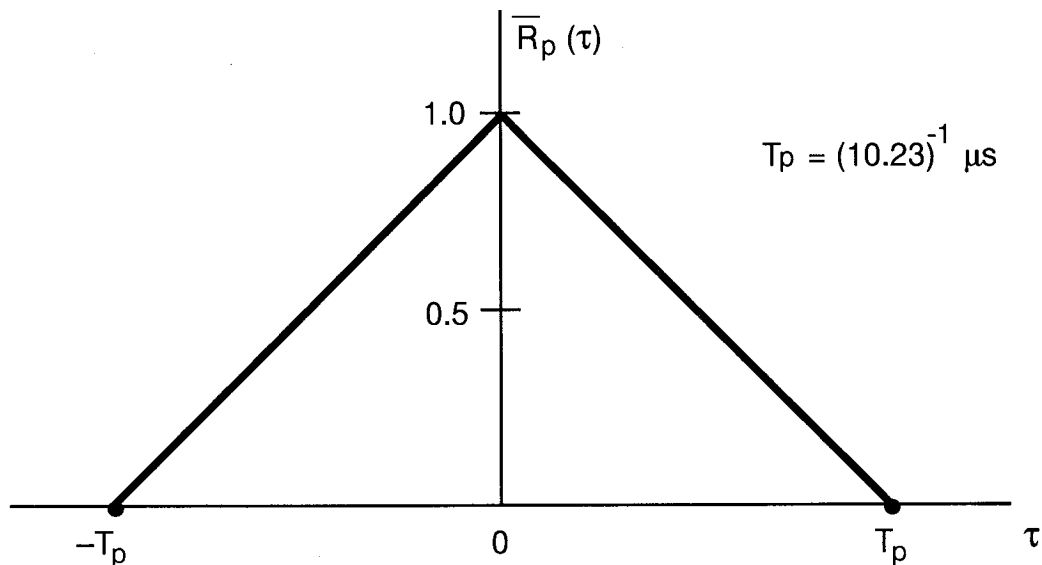


Figure 2-3. The Time-Averaged Autocorrelation Function for the P Code

The signal leaving the spacecraft is filtered so that only the main lobe and a fraction of the first sidelobes remain. If $G_S(f)$ represents the effective aggregate (complex) filter and amplification introduced by the spacecraft, the transmitted signal as it leaves the spacecraft can be cast in the form

$$S_T(t) = \int_{-\infty}^{\infty} G_S(f) A_p(f) e^{2\pi i [(f_L + f)(t + \tau_s) + \varphi_s]} df + c.c. \quad (2.18)$$

where φ_s represents phase instability in the satellite frequency system, excluding the frequency reference. The spacecraft filter is reportedly a six-pole Chebychev with 0.01-dB ripple and a 3-dB double-sided bandwidth of about 36 MHz. A clock offset τ_s has been included to represent the error in the satellite clock relative to true time. (Satellite time = true time + τ_s .) For simplicity, this expression neglects the multiplicative data-bit factor contained in the actual GPS signal. The following analysis assumes that a correlation interval is less than a data-bit width and that data-bit synchronization has been established. In this case, the data-bit factor would only change the analysis by a multiplicative sign factor throughout the equations.

In transit to the ground, the signal is retarded by a geometric delay, τ_g , and a tropospheric delay, τ_t , and is advanced in phase by an ionospheric phase shift, φ_e . After incorporation of these effects, the received signal arriving at the receiver antenna at true time t can be written in the form

$$S_R(t) = \int_{-\infty}^{\infty} G_S(f) A_p(f) e^{2\pi i [(f_L + f)(t - \tau) + \varphi_s + \varphi_e]} df + c.c. \quad (2.19)$$

where the combined delay is given by

$$\tau = \tau_g + \tau_t - \tau_s \quad (2.20)$$

Decreases in signal strength in transit are absorbed in G_S . The RF signal in Eq. (2.19) is collected by the receiver antenna for processing.

SECTION 3

FRONT-END PROCESSING

This section analyzes the steps in the TurboRogue front end that take the signal from reception at RF down to its form after baseband sampling. The current analog front end is analyzed in this section and an example of a highly digital front end is analyzed in Appendix A of this document.

3.1 Functional Description of the Analog Front End

The receiver antenna collects the GPS signal as input to the analog processing, as shown in Fig. 3-1. The output from the antenna is passed through an RF bandpass filter spanning 1075 to 1725 MHz to eliminate out-of-band RF interference (RFI). The signal is then amplified by a gallium-arsenide field-effect transistor (GaAs FET). System temperature, which includes all noise sources, is *nominally* 200 K for L1 and 225 K for L2. The resulting signal is power divided into L1 and L2 branches and each branch is downconverted to baseband with a quadrature mixer in a double-sideband mode with a fixed-frequency local-oscillator (LO) signal. The four resulting baseband signals are each passed through a low-pass seven-pole Butterworth filter with a single-sided bandwidth of 9.6 MHz, as plotted in Fig. 3-2. The four filtered signals are then each hard limited and "sign" sampled (1-bit quantization) at a rate of 20.456 MS/s. (MS/s will be used to denote 10^6 samples per second.) The same L1 samples are processed by the digital signal processor to obtain both the C/A and the P observables.

To carry out this processing, three frequencies are required: the "sample-clock" rate at $f_s = 20.456$ MHz and two LO (downconversion) signals, $f_{h1} = 1575.112$ MHz for L1 and $f_{h2} = 1227.36$ MHz for L2. The frequency-and-timing subsystem generates 20.456 MHz from a 5-MHz reference and then generates the two LOs by simple multiplication of the sample-clock rate. That is, the L1 LO is generated by the multiplication $77f_s$ (which equals $f_{L1} - 308$ kHz) and L2 by $60f_s$ (which equals $f_{L2} - 240$ kHz, where f_{L1} and f_{L2} are the zero-Doppler carriers at RF).

Care must be taken in selecting the sampling frequencies and downconversion frequencies. The sampling frequency must be essentially incommensurate with the code chip rate (i.e., 20.456 MHz vs. 10.23 MHz) so that discrete-sampling errors will be negligible. Theoretical verification of the adequacy of 20.456 MHz is presented below in Subsection 4.3. To produce positive baseband carrier frequencies, each downconversion frequency is offset from its respective carrier (by 308 kHz for L1 and 240 kHz for L2). The large resulting positive baseband carrier frequencies reduce to negligible levels the errors caused by the three-level quantization of counterrotation sinusoids applied in subsequent processing. Subappendix B.2 estimates the errors introduced by carrier counterrotation.

3.2 Mathematical Model for the Analog Front End

As described in the preceding subsection, the receiver front end passes the received signal represented by Eq. 2.19 through amplifiers and filters and downconverts from L band to baseband. This subsection models the composite effect of the antenna and front-end steps as a linear process that can be formulated as a single overall complex system filter and a single effective phase and frequency shift representing the downconversion process.

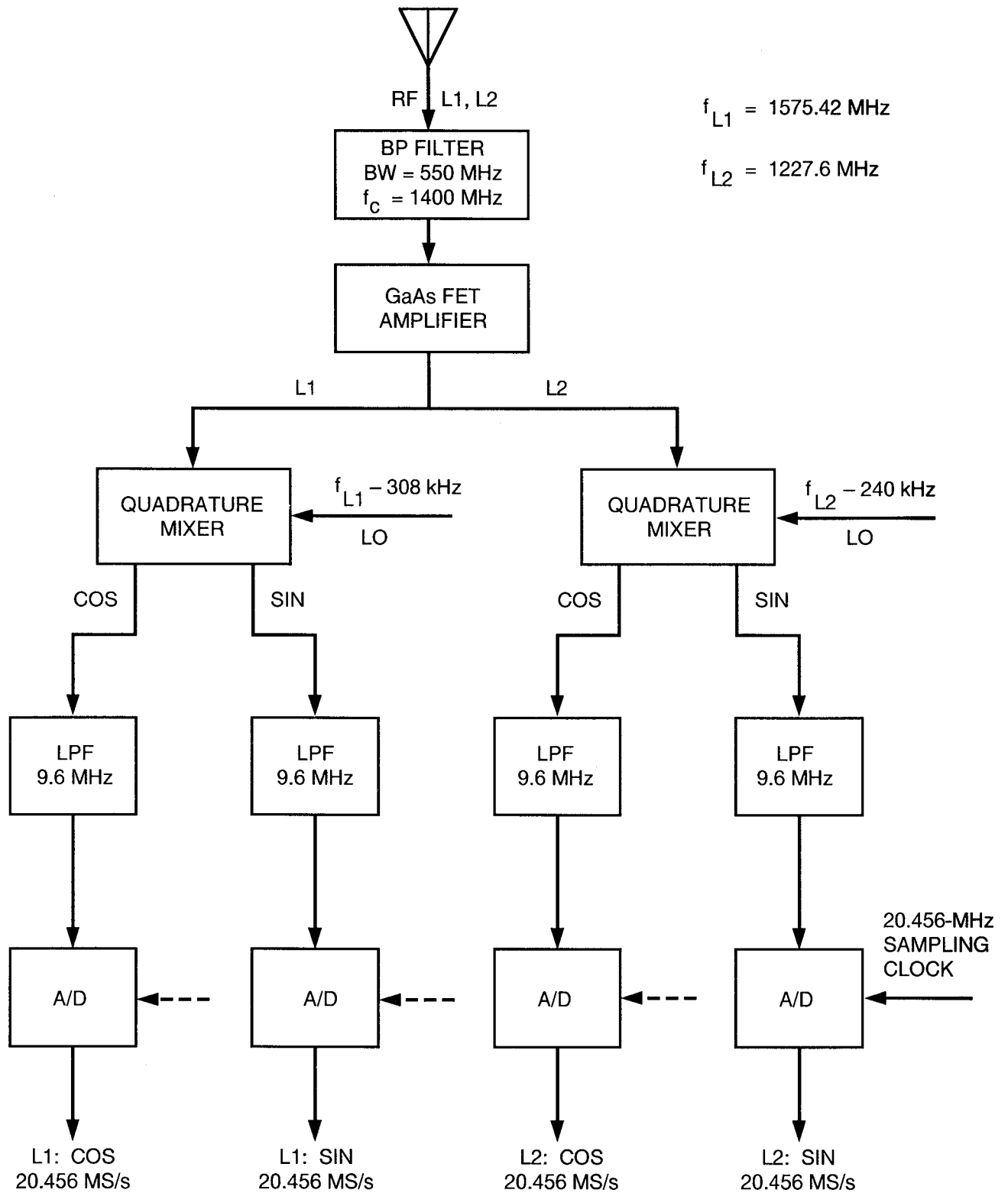


Figure 3-1. Block Diagram for the Analog Front End

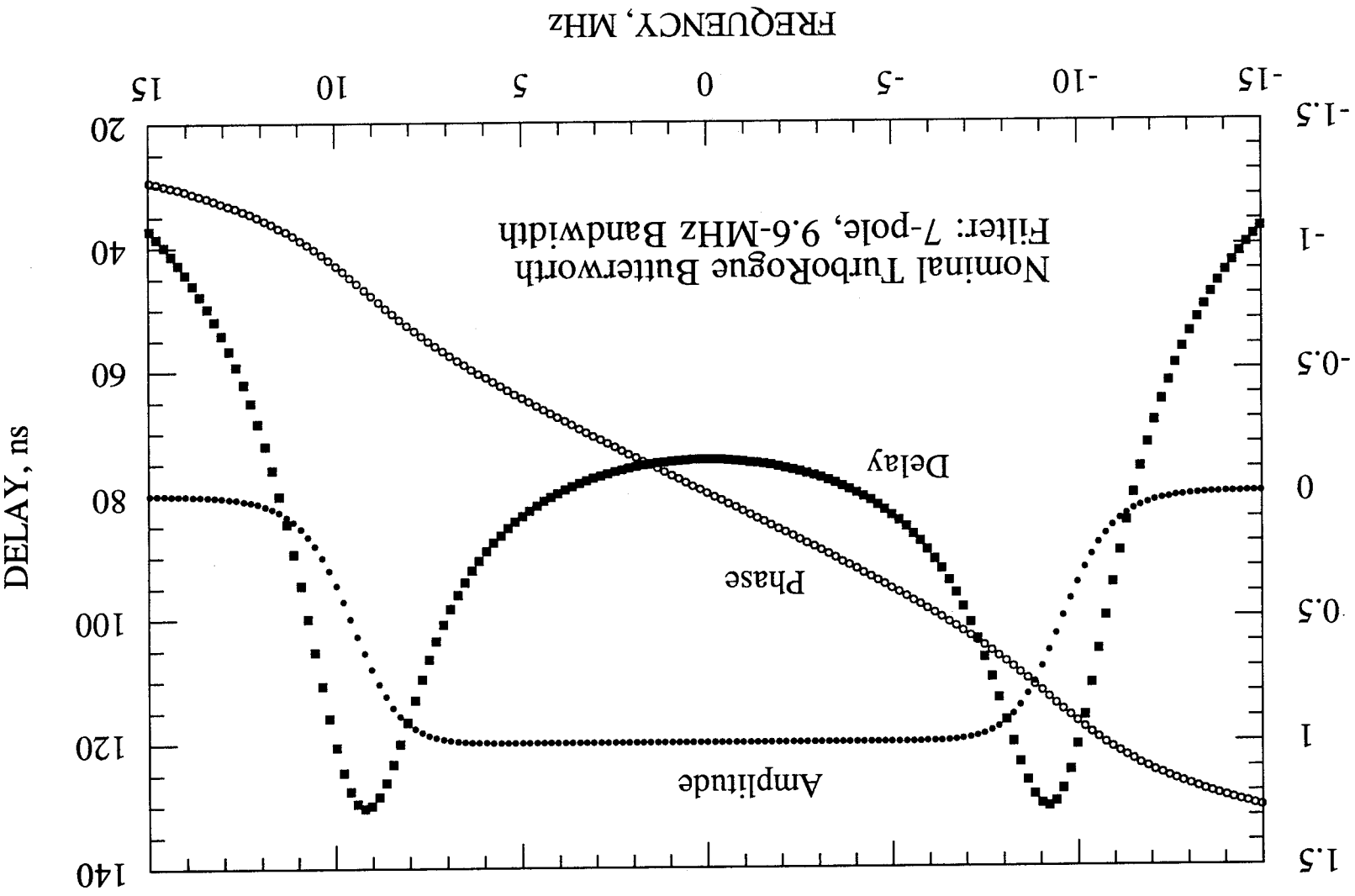


Figure 3-2. Amplitude and Phase Response of the TurboRogue Baseband Butterworth Filter

Downconversion can be modeled in the following way: Let the downconversion phase at the mixer be denoted by φ_h . Because the frequency reference of the receiver is very stable, downconversion phase can be represented by a time function with the ostensibly linear form

$$\varphi_h \equiv f_h t + \varphi_{hd} \quad (3.1)$$

where f_h is the nominal downconversion frequency and φ_{hd} is a slowly varying drift relative to the nominal linear function associated with f_h . The quadrature mixer multiplies the (real) received RF voltage by $\cos \varphi_h$ and by $\sin \varphi_h$, a process that can be modeled in complex form as a multiplication by $e^{-2\pi i \varphi_h}$. When the expression in Eq. (2.19) is multiplied by $e^{-2\pi i \varphi_h}$, the multiplication and integral can be interchanged in both the first term and the c.c. term so that the multiplication is applied separately to each frequency component. For each frequency component, one obtains a small difference frequency from the first term and a large sum frequency from the c.c. term. Since the large sum-frequency term is eliminated by filters following the mixer, only the difference frequency term must be retained in the analysis.

The preceding $e^{-2\pi i \varphi_h}$ model for downconversion from RF assumes perfect 90° separation of the sine and cosine mixing signals. In practice, the analog front end will produce sinusoids that deviate from perfect 90° separation. This offset from 90° will be called the quadrature-separation error. A quadrature-separation error introduces incoherency between the two final complex correlation sums obtained by processing the two quadrature components. Relative to a perfect amplitude of 1.0, the lowered output amplitude would be $\cos(\Delta\theta/2)$, where $\Delta\theta$ is the quadrature-separation error in radians. When $\Delta\theta$ is 16°, the voltage signal-to-noise ratio (SNR) is reduced by about 1%. According to D. J. Spitzmesser (Spitzmesser, 1994), the quadrature-separation error for the TurboRogue receiver is about 5° or less, which would cause an amplitude loss of about 0.1% or less. This result indicates that the quadrature-separation error for TR is of little ultimate importance and it will therefore be ignored in the following analysis.

Antenna gain and possible antenna filtering, phase shifting and delays will be modeled by a complex antenna filter, G_A , that is a function of RF frequency. Similarly, all amplification, filtering, phase shifts, and delays due to the front end will be modeled with a single complex filter, G_R . This front-end filter consists of a product of the filters at successive stages as well as phasors representing other phase shifts and delays. Frequency-component identification for the front-end filter, however, will be specified by means of a Doppler-shifted baseband frequency, and, as a consequence, a translation is required to make an association with the corresponding RF frequency preceding downconversion. This convention is motivated by the fact that the dominant filter is the "narrow" Butterworth filter applied at baseband.

As indicated in Fig. 3-1, each L-band channel has two quadrature components and each of these components has a separate Butterworth filter. According to Spitzmesser (Spitzmesser, 1994), the four Butterworth filters are not identical but are matched to within about 7% with respect to bandwidth. To account for the differences, a detailed analysis would provide a separate function for each of these filters. One can show, however, that the final effective filter for a given L-band channel is a straight average of the two Butterworth filters for that channel. Thus, for simplicity in analysis without sacrifice of accuracy, it will be assumed at this point that the two Butterworth filters for a given L-band channel are identical, each with a response equal to the average of the two actual filters.

Another potential concern is how well delay and phase shifts are matched between sine and cosine components in their paths from the RF branching point to baseband sampling. According to Spitzmesser (Spitzmesser, 1994), the path length for each component is only about 20 cm, and the two paths are matched to about 3 cm (0.1 ns). The relative path difference within the quadrature mixer before mixing is about 0.1 cm or less, and the corresponding relative phase

shift is about $0.1 \text{ cm}/20 \text{ cm} = 0.005$ cycles (1.8°) The relative phase shift after mixing is about $300 \text{ kHz} * 0.1 \text{ ns} = 30 \mu\text{cycles}$. These relative phase and relative delay values are too small to cause significant loss of amplitude. Observed delay will contain the average of the two component delays and this implicit average delay, combined with other delays, will be either calibrated, differenced out, or estimated in subsequent processing. Thus, none of these effects is of ultimate importance and for this reason, none will be separately modeled.

The preceding discussion indicates that the antenna and front end can be modeled by inserting the antenna filter and the composite receiver filter into the integrand of Eq. (2.19) and multiplying by $e^{-2\pi i \phi_h}$. Since filtering in the front end removes the sum-frequency term resulting from the c.c. term, the complex voltage (real and imaginary) at baseband becomes

$$V(t) = \int_{-\infty}^{\infty} G_R(f_d) G_A(v_d) G_S(f) A_p(f) e^{2\pi i [(f_L+f)(t-\tau) + \phi_s + \phi_e - \phi_h]} df + \eta \quad (3.2)$$

where the Doppler-shifted frequency at RF corresponding to f , the baseband variable of integration, is given by

$$v_d = (f_L + f)(1 - \dot{\tau}) + \dot{\phi}_s + \dot{\phi}_e \quad (3.3)$$

in which the top dot denotes time derivative. The corresponding baseband frequency is given by

$$f_d = v_d - f_h \quad (3.4)$$

The complex term η represents all noise, after the downconversion and filtering operations, including the noise picked up by the antenna and the noise added by the receiver. Almost all of the noise contributed by the receiver is added at RF. Analyses of the effects of the noise term are presented in Section 7, Appendix C, and Appendix D of this document.

3.3 Mathematical Model for the Sampled Signal

The baseband signal theoretically represented by Eq. (3.2) is hard limited and sign sampled at a sample rate of 20.456 MHz. Timing for the sampler is derived from the receiver clock, which will have an offset from true time. True time t and receiver time t_R (as indicated by the sampler) will be related by

$$t_R = t + \tau_R \quad (3.5)$$

where τ_R is the error in the receiver clock. A quantized complex sample value at time t_R will be denoted by $\tilde{V}(t_R)$. For a particular time t_R , the theoretical form for the voltage V is obtained by substituting $t_R - \tau_R$ in place of true time t in the right-hand side of Eq. (3.2).

As discussed in Appendix B for low SNR signals, the sampled voltage after averaging over noise is approximately proportional to the signal component divided by the root-mean-square (RMS) noise. Thus, when the complex voltage in Eq. (3.2) is subjected to two-level quantization in each quadrature component and then to an ensemble average over noise, η , the theoretical form for the averaged complex voltage becomes

$$\langle \tilde{V}(t_R) \rangle_{\eta} \approx \frac{q_M}{\sigma_{\eta}} \int_{-\infty}^{\infty} G_R(f_d) G_A(v_d) G_S(f) A_p(f) e^{2\pi i[(f_L+f)(t_R-\tau') + \varphi_s + \varphi_e - \varphi_h]} df \quad (3.6)$$

where the tilde on V denotes amplitude quantization, $\langle \rangle_{\eta}$ denotes average over noise and σ_{η} is RMS noise on either quadrature component. (It will be assumed that RMS noise is the same for the two components. The fact that this assumption is only approximately valid does not change the results of the following analysis, since only single-sample SNR matters in 1-bit sampling, and single-sample SNR is the same for the two components.) Delay has been redefined to incorporate the sampler clock error that enters when true time is replaced with sampler time:

$$\tau' = \tau + \tau_R = \tau_g + \tau_t - \tau_s + \tau_R \quad (3.7)$$

As derived in Appendix B, the proportionality factor q_M accounts for sampling quantization and is given by

$$q_M = \sqrt{\frac{2}{\pi}} \quad (3.8)$$

for two-level quantization.

3.4 Reformulation of the Sampled Signal

Subsequent analysis can be clarified by explicitly defining and collecting terms of like nature in the signal component. First expand the ionosphere phase about the carrier frequency

$$\varphi_e(f_L+f) \approx \varphi_e(f_L) + \frac{\partial \varphi_e}{\partial f} f \quad (3.9)$$

which becomes

$$\varphi_e(f_L+f) \approx \varphi_e(f_L) - \tau_e f \quad (3.10)$$

where τ_e is the group delay due to the ionosphere. Next, reformulate and consolidate the bandpass filters

$$G_R(f_d) G_A(v_d) G_S(f) \equiv G(f) e^{-2\pi i(f \tau_I - \varphi_I)} \quad (3.11)$$

where the composite bandpass amplitude is defined as

$$G(f) \equiv |G_R(f_d) G_A(v_d) G_S(f)| \quad (3.12)$$

and τ_I is the overall instrumental group delay, including spacecraft, antenna, and receiver. The frequency-dependent term φ_I is the instrumental phase effect that remains after removing the linear phase-versus-frequency function associated with τ_I . Note that the bandpass amplitude, the instrumental phase, and the effective instrumental delay can potentially depend on Doppler shift, as indicated in Eq. (3.11) by the Doppler-shifted arguments, f_d and v_d .

The effective delay introduced by the Butterworth filter described in Subsection 3.1 is about 77 ns for the P code. This delay is the approximate theoretical value for the Butterworth filter itself and does not include other instrumental delays introduced by the front end.

When Eqs. (3.10) and (3.11) are substituted in Eq. (3.6), the noise-averaged baseband signal becomes

$$\langle \tilde{V}(t_R) \rangle_{\eta} = \frac{q_M}{\sigma_{\eta}} e^{2\pi i \phi_a} \int_{-\infty}^{\infty} G(f) A_p(f) e^{2\pi i [f(t_R - \tau_a) + \phi]} df \quad (3.13)$$

where aggregate group delay is defined by

$$\tau_a \equiv \tau_g + \tau_t - \tau_s + \tau_R + \tau_e + \tau_I \quad (3.14)$$

and aggregate baseband carrier phase by

$$\phi_a \equiv f_L(t_R - \tau'_{\phi}) - \phi_h \quad (3.15)$$

in which aggregate phase delay is given by

$$\tau'_{\phi} \equiv \tau_g + \tau_t - \tau_s + \tau_R - f_L^{-1}[\phi_s + \phi_e(f_L)] \quad (3.16)$$

All time-varying quantities are evaluated at sample time, t_R .

Equation (3.13) indicates that the baseband signal consists of a product of a carrier factor with a rate of $f_L(1 - \tau'_{\phi}) - f_h$ and a code factor involving an integral over the Fourier components of the P code. This formulation has representative variables for the major effects encountered in processing GPS signals. Note, however, that a bandpass-averaged instrumental phase shift emerges from the integral, and, furthermore, the best definition of an effective instrumental delay can be application dependent.

SECTION 4

CORRELATION IN THE CODE MODE

When the P code is known, the receiver correlates the baseband samples with a model signal consisting of the appropriate P-code sequence, offset by a model delay, and a carrier phasor incorporating a model phase. Model phase and model delay are supplied in real time as feedback by delay- and phase-locked loops operating on correlation output. This report will not treat feedback theory, but will assume that model phase and model delay are adequately provided by loops operating on correlation output. Correlation analysis for the C/A code, which is slightly different than P-code analysis, is presented in Appendix E.

4.1 Model Signal

The model signal generated by the receiver at receiver (sampler) time t_R has the form

$$V_m(t_R, l) = P(t_R - \tau_m - ls) \tilde{C}(\varphi_m) \quad (4.1)$$

where P is the ideal P-code function in Eq. (2.1), τ_m is the feedback model for total group delay at time t_R , l is a lag offset relative to the model delay, s is the sample interval of $(20.456)^{-1} \mu\text{s}$, and φ_m is the feedback model for phase at time t_R . Note that the receiver generates the code sequence as a function of t_R , as though t_R were true time. The model signal is generated for each of three lags (-1, 0, +1) in the TurboRogue receiver. As a function of time, the generated model code consists of the sequence of -1s and +1s specific to the satellite being tracked, but with effectively instantaneous transitions between chips (i.e., with no filtering), as implied by Eqs. (2.1) and (4.1). Further, the P-code sequence is generated with a delay that is effectively exactly equal to the model delay generated by the feedback loops. Over a correlation interval of 18 ms, the receiver generates both the model delay and the model phase as linear time functions.

The model signal contains both sine and cosine components in order to provide quadrature counterrotation of the carrier of the sampled signal. The complex quantity, \tilde{C} , is a quantized counterrotation phasor defined by

$$\tilde{C}(\varphi_m) \equiv \tilde{\text{c}}\tilde{\text{o}}\tilde{\text{s}}(\varphi_m) - i \tilde{\text{s}}\tilde{\text{i}}\tilde{\text{n}}(\varphi_m) \quad (4.2)$$

where the tildes indicate three-level quantization, as explained in Appendix B. The quantized phasor can be expanded in terms of the harmonics of the fundamental in the form

$$\tilde{C}(\varphi_m) = c_1 e^{-2\pi i \varphi_m} + \text{harmonics} \quad (4.3)$$

where $c_1 = 1.176$ is the coefficient of the fundamental for the chosen three-level quantization.

Remembering that $P(t)$ is real, one can take the complex conjugate of Eq. (2.16), substitute the result in Eq. (4.1), and obtain a useful form for the receiver model in terms of frequency components:

$$V_m(t_R, l) = \tilde{C}(\varphi_m) \int_{-\infty}^{\infty} A_p^*(f') e^{-2\pi i f'(t_R - \tau_m - ls)} df' \quad (4.4)$$

where $A_p(f)$ represents the Fourier components in Eq. (2.6) pertaining to the particular code sequence within the correlation interval. Note that the receiver time argument in Eq. (4.1) has been substituted directly in Eq. (2.16) without including the difference, τ_R , between receiver time and true time. This procedure is based on the fact that the receiver generates its P code exactly as represented in Eqs. (2.1) and (2.16) but on the basis of its own time scale: receiver time. No bandpass filtering is included in this equation because the receiver generates a P-code sequence that is essentially an ideal sequence.

4.2 Correlation Sum

At each sample point, the receiver generates the model signal in Eq. (4.1) and multiplies it by the sampled signal. For each lag value, the resulting product is accumulated for all points within a correlation interval to obtain a correlation sum, computed as

$$u_l(t_R) = \sum_{k=-N}^N \tilde{V}(t_R + ks) V_m(t_R + ks, l) \quad (4.5)$$

where \tilde{V} is the complex sampled signal, t_R is now the receiver time at the center of the sum interval, and the index k covers the sample points within the correlation interval. The correlation interval, whose length (integration time) will be denoted by T , is 18-ms long and contains about 360,000 sample points for the current implementation of the TurboRogue receiver. In Eq. (4.5), it is assumed without significant loss of generality that the interval contains an odd number of samples with the total number given by $N_s = 2N + 1$. The integration time is related to total number of samples by $T = N_s s$. Since the sampled signal and model signal are complex, the correlation sums are complex.

4.3 Correlation Function

The correlation function is obtained by taking an ensemble average of the correlation sums in Eq. (4.5) with respect to all possible noise patterns and P-code sequences. An ensemble average over noise gives

$$\langle u_l(t_R) \rangle_{\eta} = \sum_{k=-N}^N \langle \tilde{V}(t_R + ks) \rangle_{\eta} V_m(t_R + ks, l) \quad (4.6)$$

where $\langle \rangle_{\eta}$ denotes the noise average. On the right side, the noise average has been interchanged with the sum and applied to the only factor containing noise, the sampled signal. After substitution of Eqs. (3.13), (4.3), and (4.4), and application of an ensemble average over code, Eq. (4.6) becomes

$$\langle u_l(t_R) \rangle = c_1 \frac{qM}{\sigma_\eta} \int_{-\infty}^{\infty} \int_{-\infty}^{\infty} G(f) \langle A_p(f) A_p^*(f') \rangle_p S_c df df' \quad (4.7)$$

where

$$S_c \equiv \sum_{k=-N}^N e^{2\pi i [\varphi_a - \varphi_m + (f-f')(t_R+ks) - f\tau_a + f'(\tau_m+ls) + \varphi_l]} \quad (4.8)$$

in which the phase and delay functions are evaluated at time $t_R + ks$. The unlabeled brackets $\langle \rangle$ denote ensemble average over both noise and code, while $\langle \rangle_p$ denotes ensemble average only over code. To reach this form, the sum and integrals have been interchanged and only the Fourier components within the integral have been treated as random variables subject to the ensemble average over code. Further, only the fundamental of the counterrotation phasor in Eq. (4.3) has been retained under the assumption that the higher harmonics are filtered out by the sum over the correlation interval.

Counterrotated phase in Eq. (4.8) can be expanded about the center time to yield

$$\varphi_a(t_R+ks) - \varphi_m(t_R+ks) \approx \varphi_d + \dot{\varphi}_d ks \quad (4.9)$$

where the phase difference at interval center t_R is defined by

$$\varphi_d \equiv \varphi_a(t_R) - \varphi_m(t_R) \quad (4.10)$$

and where $\dot{\varphi}_d$ is the feedback error for phase rate across the interval (i.e., the last equation but with top dots). Similarly, the delay terms in Eq. (4.8) can be expanded to yield

$$f\tau_a(t_R+ks) - f'\tau_m(t_R+ks) \approx f [\tau_a(t_R) + \dot{\tau}_a ks] - f' [\tau_m(t_R) + \dot{\tau}_m ks] \quad (4.11)$$

which becomes

$$f\tau_a(t_R+ks) - f'\tau_m(t_R+ks) \approx f\tau_a(t_R) - f'\tau_m(t_R) + (f-f')\dot{\tau}_a ks \quad (4.12)$$

where, in the last equation, it has been assumed that the model delay rate very accurately tracks actual delay rate. One can show that this approximation is acceptable for even the worst-case errors in delay rate (< 5 ns/s).

When Eqs. (4.9) and (4.12) are substituted in Eq. (4.8), one obtains

$$S_c \approx e^{2\pi i [\varphi_d + (f-f')t_R - f\tau_a + f'(\tau_m+ls) + \varphi_l]} \sum_{k=-N}^N e^{2\pi i [(f-f')(1-\dot{\tau}_a) + \dot{\varphi}_d] ks} \quad (4.13)$$

where τ_a and τ_m are now evaluated at interval center. The sum in this equation can be evaluated in a manner similar to the derivation of Eq. (2.9), which yields

$$S_c \approx e^{2\pi i[\phi_d + (f-f')t_R - f\tau_a + f'(\tau_m + l_s) + \phi_l]} \frac{\sin[N_s \pi[(f-f')(1-\dot{\tau}_a) + \dot{\phi}_d]s]}{\sin[\pi[(f-f')(1-\dot{\tau}_a) + \dot{\phi}_d]s]} \quad (4.14)$$

where N_s is the total number of sample points in the interval.

When Eq.(4.14) and the expectation value in Eq. (2.10) are substituted in Eq. (4.7), one obtains

$$\langle u_l(t_R) \rangle = c_1 \frac{q_M}{\sigma_\eta} T_p^2 e^{2\pi i \phi_d} \int_{-\infty}^{\infty} \int_{-\infty}^{\infty} H(f, f') e^{2\pi i[(f-f')\tau_R - f\tau_a + f'(\tau_m + l_s) + \phi_l]} df df' \quad (4.15)$$

where the two-dimensional "filter" function is defined as

$$H(f, f') \equiv G(f) \frac{\sin(\pi f T_p)}{\pi f T_p} \frac{\sin(\pi f' T_p)}{\pi f' T_p} \frac{\sin[N_c \pi (f-f') T_p]}{\sin[\pi (f-f') T_p]} \frac{\sin[N_s \pi[(f-f')(1-\dot{\tau}_a) + \dot{\phi}_d]s]}{\sin[\pi[(f-f')(1-\dot{\tau}_a) + \dot{\phi}_d]s]} \quad (4.16)$$

Equation (3.5) has been used to replace $t_R - \bar{t}$ with τ_R .

In order to schematically illustrate the nature of the "sinx/siny" functions in Eq. (4.16), Fig. 4-1 plots Eq. 4.16 as a function of $f - f'$ for an unrealistically small correlation interval ($N_s = 22$) and for an excessive sample rate of 22.456 MS/s. These plots show that both of the two sinx/siny functions are "comb" functions consisting of a sequence of equally spaced peaks, with a peak spacing of 10.23 MHz for the first sinx/siny function and about 22.456 MHz for the second. Peak height is given by the number of chips ($N_c = 10$) for the first sinx/siny function and by the number of samples ($N_s = 22$) for the second. For both, the width is $1/T$, where T is the length of the correlation interval. For an actual correlation interval (e.g., $T = 18$ ms and a P sample rate of 20.456 MHz), these peaks become extremely high (e.g., about 10^5 larger than intervening peaks) and extremely narrow relative to the chip rate and sample rate (e.g, 55 Hz versus 10.23 MHz). For the example shown in Fig. 4-1, note that only the "origin" peaks at $f-f'=0$ line up between the two sinx/siny functions in Eq. (4.16), while the other peaks do not line up. This absence of peak coincidence away from $f-f'=0$, which is a consequence of the effective incommensurability between 10.23 Mhz and 22.456 MS/s, leaves only the origin peaks to make a significant contribution to the integral. If only the origin peaks are significant, the system has been successfully designed so that discrete sampling effects are negligible.

For the actual sample rate of 20.456 MS/s, one can also show that only the origin peaks are significant. For *zero Doppler*, the commensurability ratio for the sample rate and chip rate reduces to

$$\frac{f_p}{f_s} = \frac{s}{T_p} = \frac{10230000}{20456000} = \frac{5115}{10228} \quad (4.17)$$

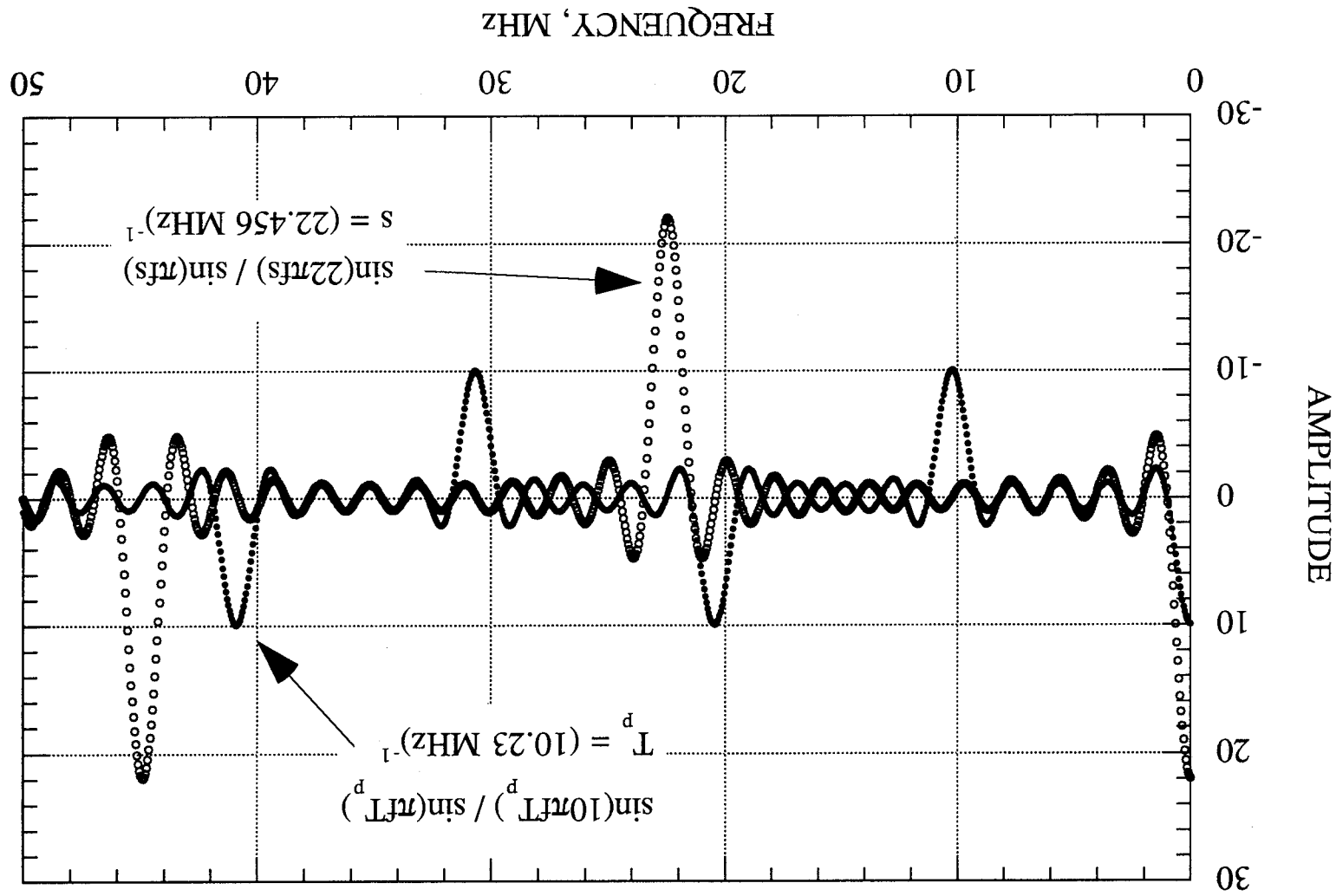
after common factors have been removed. Given this result, one can easily show for zero Doppler that the first coincidence of peaks for $|f-f'|$ above zero occurs at

$$|f - f'| = 5115 * 20.456 \text{MHz} = 10228 * 10.23 \text{MHz} \quad (4.18)$$

or equivalently

$$|f - f'| = 104.63244 \text{GHz} \quad (4.19)$$

Figure 4-1. Schematic Illustration of the sinc/siny Functions



For $|f - f'|$ to be this large, the magnitude of either f or f' must be greater than about 52 GHz. Because of the filtering effect of G and the two sinc/x functions at high frequencies in Eq. (4.16), this particular coincidence peak and other coincidence peaks at even higher multiples are reduced to negligible influence in the integral. For example, for a first coincidence peak with $f' = 52$ GHz, the sinc/x filter supplies an attenuation of about 0.00006 (-84 dB). One can show that an amplitude error of 0.00006 leads to a delay error on the order of 1 mm.

Inserting nonzero values of Doppler (represented by delay rate, $\dot{\tau}_a$) will improve effective incommensurability. Delay rate for ground-based receivers, for example, is less than 3 $\mu\text{s}/\text{s}$. One can show that a Doppler effect this size will shift the peaks of the sinc/siny function by an amount too small to align any peaks that were not already aligned for zero Doppler. More importantly, Doppler shifting will dealign peaks that would have been coincident (but are not at the origin) for zero Doppler and thereby reduce commensurability effects to even smaller levels. On the basis of Eq.(4.16), one can easily show that Doppler reduces the amplitude of a given product of coincident peaks by a factor of about $\pi \Delta f \dot{\tau}_a T_I$ or more, where T_I is the integration interval and where $\Delta f = |f - f'|$ is the frequency difference at the peak. For the very small Doppler value of 1.5 Hz ($\dot{\tau}_a = 1$ ns/s) and the short integration time of 1 s, for example, the reduction factor is equal to 327 at the first coincident peak at 104 GHz. Thus, even for very small Doppler values, the commensurability error is greatly reduced by the Doppler effect.

The preceding analysis indicates that commensurability of sample rate and chip rate will introduce delay errors on the order of 1 mm for the worst case of zero Doppler and even smaller delay errors when Doppler is included.

When in lock, the rate-error term $\dot{\phi}_d$ in Eq. (4.16) is not large enough to cause peaks to completely dealign, but can cause amplitude loss. This loss is accounted for below in the final form for the correlation function.

When the number of sample points N_s is very large, and when the sample rate and the chip rate are essentially incommensurate, as indicated, the above considerations show that the product of the two sinc/siny functions reduces to a spike function at $f - f' = 0$. By approximating the two sinc/siny functions by sinc/x functions near $f - f' = 0$ and approximating the first of these two sinc/x functions by a Dirac delta function (assuming N_c is very large), one can show that this product can be accurately approximated, within the significant ranges of the two sinc/x filters in Eq. (4.16), by

$$\frac{\sin[N_c \pi (f - f') T_p]}{\sin[\pi (f - f') T_p]} \frac{\sin[N_s \pi [(f - f')(1 - \dot{\tau}_a) + \dot{\phi}_d] s]}{\sin[\pi [(f - f')(1 - \dot{\tau}_a) + \dot{\phi}_d] s]} \approx \frac{N_s}{T_p} \frac{\sin(N_s \pi \dot{\phi}_d s)}{N_s \pi \dot{\phi}_d s} \delta(f - f') \quad (4.20)$$

where $\delta(f - f')$ is the Dirac delta function, given in this case by the limit

$$\delta(f - f') = T_p \text{LIM} \left[\frac{\sin[N_c \pi (f - f') T_p]}{\pi (f - f') T_p} \right], \quad N_c \rightarrow \infty \quad (4.21)$$

When Eqs. (4.16) and (4.20) are substituted in Eq. (4.15), the correlation function becomes

$$\langle u_l(t_R) \rangle = A_c e^{2\pi i \phi_d} \int_{-\infty}^{\infty} G(f) \left[\frac{\sin(\pi f T_p)}{\pi f T_p} \right]^2 e^{-2\pi i [f(\tau_r - l_s) - \phi_l]} df \quad (4.22)$$

where the amplitude factor is defined by

$$A_c \equiv N_s T_p c_1 \frac{q_M}{\sigma_\eta} \frac{\sin(\pi \phi_d T)}{\pi \phi_d T} \quad (4.23)$$

in which the expression $T = N_s s$ has been used to simplify on the basis of correlation sum length. In this expression, difference phase, ϕ_d , is defined by Eq. (4.10) and residual delay by

$$\tau_r \equiv \tau_a(t_R) - \tau_m(t_R) \quad (4.24)$$

with both time tagged at the center of the correlation interval. Note that an additional phase shift can emerge from the integral in Eq. (4.22) to contribute to phase. This result for the cross-correlation function is very similar to the form that would be obtained in analog processing and therefore indicates successful removal of discrete-sampling effects.

4.4 Discussion of the Correlation Function

As one would expect, correlation amplitude Eq. (4.22) increases in proportion to N_s , the number of sample points in the correlation sum. As discussed in Appendix B of this document, the multiplicative factor q_M and the RMS noise σ_η account for sampling quantization. The factor c_1 represents the amplitude increase due to three-level quantization of the counterrotation sinusoids. A $\sin x/x$ multiplicative factor models the amplitude loss due to feedback error in carrier-phase rate across the correlation interval. Rate feedback is accurate enough to keep amplitude loss resulting from this effect at an acceptable level. (Typically, this loss is negligible, but can reach 0.2 dB under worst-case dynamics.) A multiplicative phasor based on ϕ_d accounts for most of the feedback error in carrier phase at interval center. (A small additional carrier-phase effect can emerge from the correlation integral to contribute to the model for residual phase.) Typically, tracking error, including the contribution from the integral, is very small (< 0.02 cycle) but might reach 0.1 cycle under extreme dynamics.

The integral across the passband yields a complex correlation response that is a function of model delay τ_m and lag l and provides a measure of the alignment of the model P code with actual P code. The integrand contains the system filter in Eq. (3.12) resulting from spacecraft, antenna and receiver, and a $(\sin x/x)^2$ function representing the average power spectrum of the pure P code. This integral peaks in magnitude when the model delay, including lag offset, closely approximates the actual delay. After the correlation sums have been obtained from the correlation process, residual delay, τ_r , can be estimated through analysis of the variation of amplitude with lag, as discussed in the next section. Typically, feedback is accurate enough to keep the model P code aligned with the incoming P code to better than 0.001 P-chip so that a given lag (the "prompt") produces an amplitude very near the peak of the correlation function. Correlation amplitude for L1-P is plotted in Fig. 4-2(a) as a function of model delay on the basis of the bandpass function for the current analog front end described in Subsection 3.1. The model delay in these plots is referenced to true delay. (That is, a model delay of zero corresponds

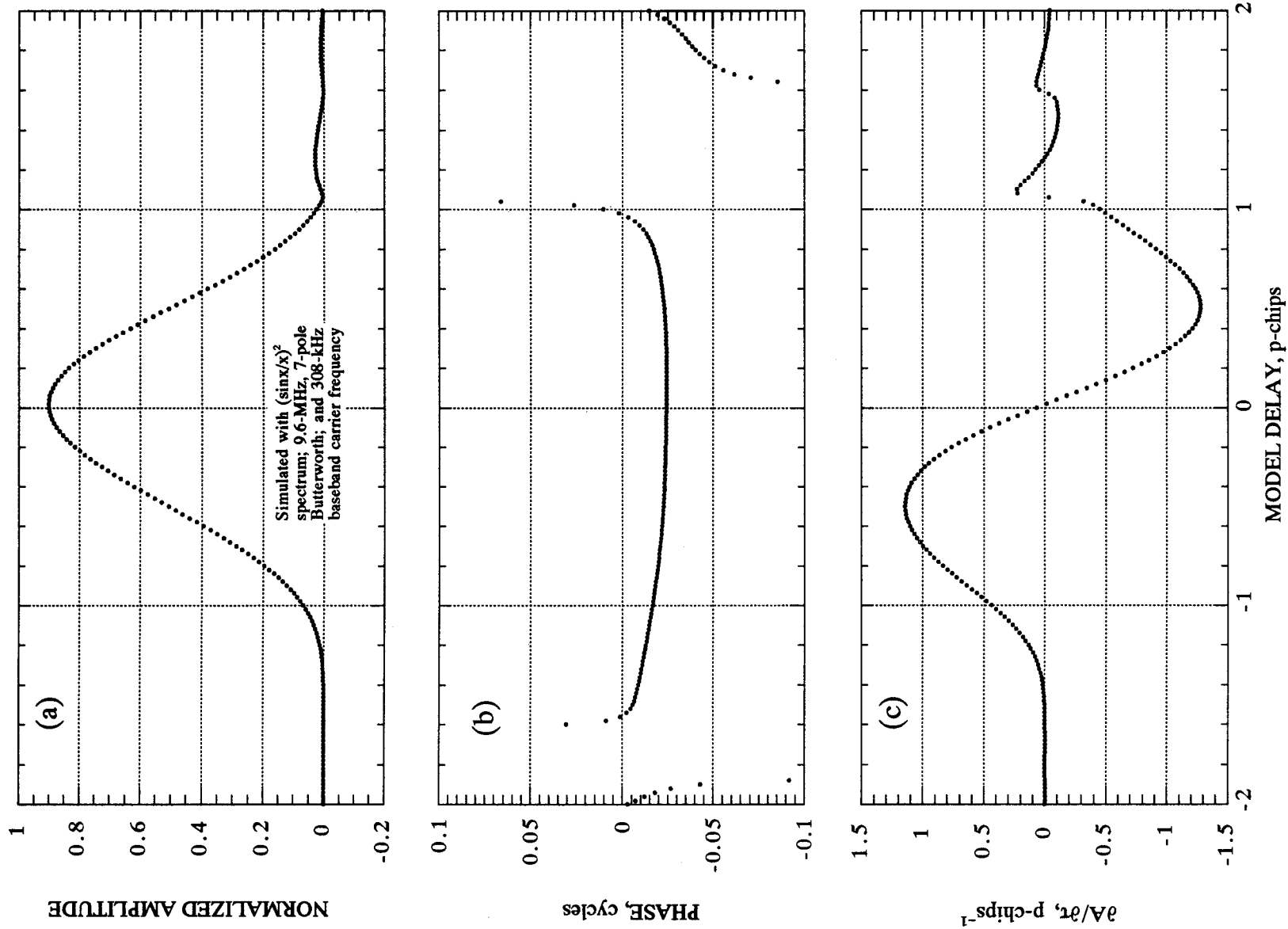


Figure 4-2. P-Code Correlation Function for the TurboRogue Receiver with the Analog Front End

approximately to zero residual delay.) Asymmetry in the amplitude-versus-delay response in this example is caused by the nonlinear phase-versus-frequency response of the receiver's baseband Butterworth filter. If the system filter passed all the frequency components of an *ideal* P code, the amplitude-versus-delay response would have the exact triangle shape shown in Fig. 2-3. Filtering rounds the sharp corners and broadens the response to the form shown in Fig. 4-2(a). Fig. 4-2(b) presents the corresponding phase-versus-delay response, which is nearly constant around zero residual delay. For purposes of illustration, the phase at zero delay in this plot has been offset from zero. In practice, this phase offset does not appear in the measured correlation sums corresponding to Eq. (4.22) since the phase-locked loop removes it along with all other phase offsets. Fig. 4-2(c), which presents the derivative of P correlation amplitude with respect to delay, is used in Subsection 6.1.2.

For comparison, Fig. 4-3(a) plots C/A correlation amplitude as a function of model delay, given a pure $(\sin x/x)^2$ power spectrum for the C/A code. (As discussed in Appendix E, code self-noise can cause significant deviations from this $(\sin x/x)^2$ spectrum.) The C/A response is almost a perfect triangle, since the Butterworth filter is so broad relative to the C/A spectrum. Slight rounding near the peak and slight ringing near +1 c-chip is barely discernible. Fig. 4-3(b) presents the corresponding phase-versus-delay response. Similar to the P result, the phase at zero residual delay has been offset from zero. Note the slight ringing caused by the loss of sidelobes above the tenth sidelobe as a result of the Butterworth filter. Fig. 4-3(c), which presents the derivative of C/A correlation amplitude with respect to delay, is analogous to Fig. 4-2(c).

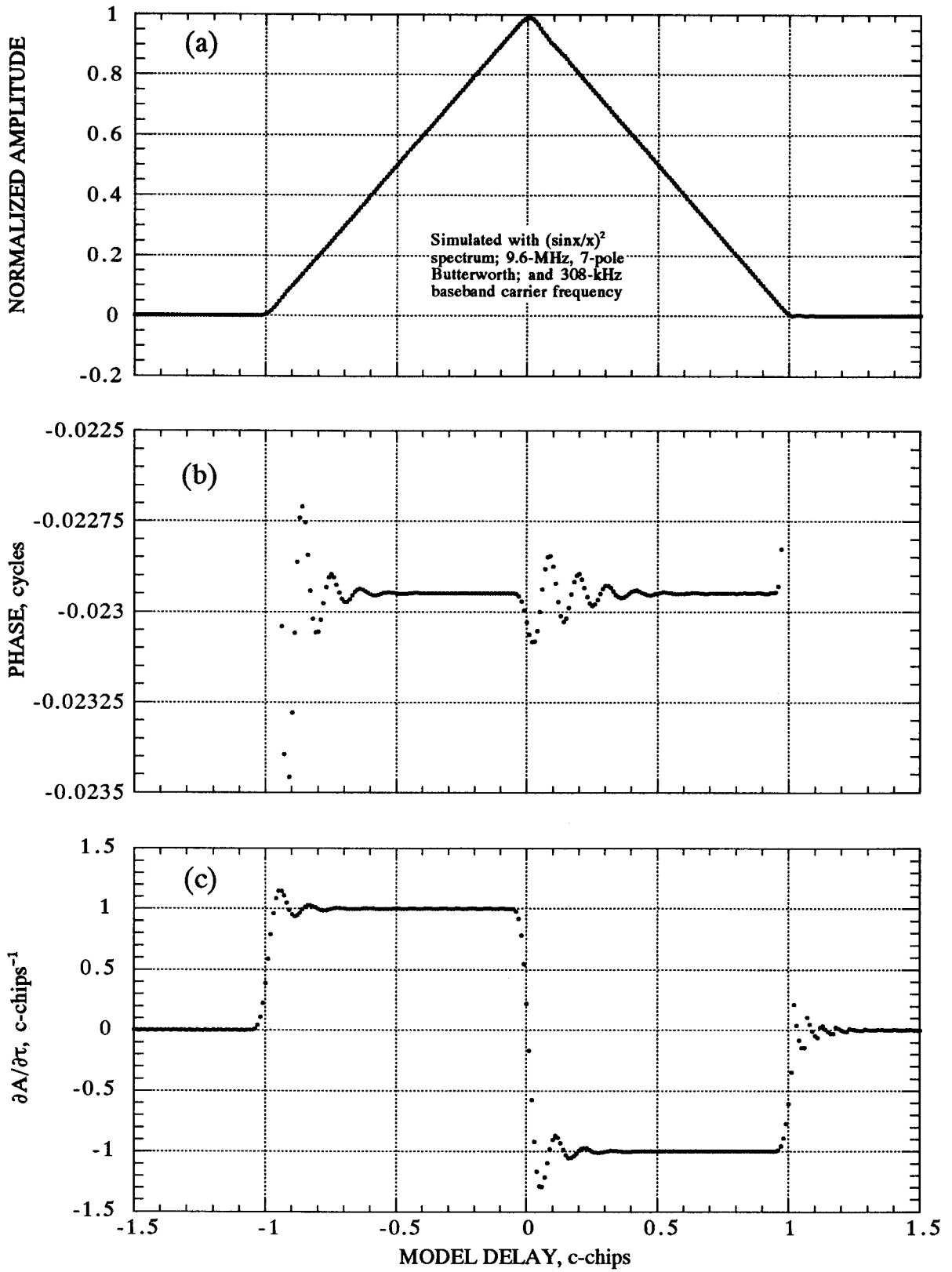


Figure 4-3. Code-Noise-Free C/A-code Correlation Function for the TurboRogue Receiver With the Analog Front End

SECTION 5

CROSS-CORRELATION IN THE P-CODELESS MODE

When the P code is encrypted, the L1-P and L2-P channels can be processed in a "P-codeless mode" that cross-correlates the two channels and thereby takes advantage of the fact the P-code sequence is the same on the two channels. In the following analysis, P-codeless operations will be denoted by L1*L2. For each sample point, the sampled voltages from the two channels are multiplied together, with one channel offset by a feedback model delay. The carrier of the product is counterrotated on the basis of feedback model phase, and the result is summed over a correlation interval of 18 ms. The resulting correlation sums are analyzed to generate the next values for phase and delay feedback and to extract the difference phase and difference delay between the L1-P and L2-P signals. The primary disadvantage of operating in the P-codeless mode is that SNR is lower and output observables are noisier.

5.1 Correlation Sum

For each lag value, the receiver generates the following cross-correlation sum over a correlation interval of length T:

$$u_l(t_R) = \sum_{k=-N}^N \tilde{V}_1(t_R + ks - L_X s - l s) \tilde{V}_2^*(t_R + ks) \tilde{C}(\varphi_m) \quad (5.1)$$

where \tilde{V}_1 and \tilde{V}_2 are the (complex) sampled voltages for the L1 and L2 channels, respectively; \tilde{C} is the counterrotation phasor in Eq. (4.2); φ_m is model phase at time $t_R + ks$; L_X is the model delay fed back by the tracking loop; and l is one of the three correlation lags (-1, 0, +1). Again, the total number of samples in the sum is odd and given by $N_s = 2N + 1$; the correlation time is given by $T = N_s s$; the time tag t_R is at the center of the sum interval; and the index k covers the points in the interval. A theoretical expression for the noise-averaged value for the L1 or L2 baseband signal can be obtained from Eq. (3.13) by attaching the appropriate channel subscript to each channel-specific symbol.

The delay difference between the L1 and L2 channels is primarily due to the ionosphere and is therefore a relatively small, slowly varying difference. Based on analysis of the amplitude-versus-lag dependence of cross-correlation sums, the receiver feeds back a slowly varying model delay, L_X , that is needed to place the maximum correlation response at the prompt lag. Because the L2 channel experiences a larger ionospheric delay than the L1 channel, the model delay is applied to the L1 channel so that lagging will be in the right direction to bring the two channels into delay alignment. Unlike the model delay applied to the code in the code mode, the model delay applied to L1 in the P-codeless mode can only be changed in steps of a sample interval, which is given by $s = (20.456 \text{ MHz})^{-1}$. Since the ionospheric delay difference between L1 and L2 is typically 100 ns or less, L_X is typically 0, 1, or 2 (in units of sample interval, s).

As shown below, phase of the $V_1 * V_2$ product is equal to L1 phase minus L2 phase. The phase-rate difference between L1 and L2 is equal to an LO term of 68 kHz plus a Doppler term that is about 1 kHz or less in magnitude for earth-fixed receivers. To track L1*L2 phase, TR first computes a rapidly varying (fast) model phase by scaling, according to frequency (i.e., by 34/154), the C/A feedback phase obtained on the basis of a phase-locked loop tracking C/A phase. Because of the influence of the ionosphere, L1*L2 phase exhibits a slow drift relative to scaled C/A phase, with a differential rate that is usually less than 0.1 Hz for an earth-fixed receiver. This slow differential drift is tracked by a secondary phase-locked loop. Total model

phase ϕ_m used for feedback is computed as the sum of the scaled C/A phase and a correction based on the output of the secondary loop.

5.2 Correlation Function

As in the case of known code, the correlation function for L1*L2 is obtained by applying an ensemble average over both noise and code to the correlation sum. Such an analysis is initiated by applying an ensemble average over noise (from both channels) to Eq. (5.1). Since noise is uncorrelated between the L1 and L2 channels, the ensemble average over the two noise components decouples, leading to separate averages for the two sampled voltages:

$$\langle u_l(t_R) \rangle_{\eta} = \sum_{k=-N}^N \langle \tilde{V}_1(t_R + kS - L_X S - lS) \rangle_{\eta_1} \langle \tilde{V}_2^*(t_R + kS) \rangle_{\eta_2} \tilde{C}(\phi_m) \quad (5.2)$$

where sum and averages have been interchanged. Eq. (3.13) can be substituted twice in Eq. (5.2), once for each averaged voltage, with appropriate labeling for channel-specific quantities. After the additional substitution of Eq. (4.3) in Eq. (5.2), the result can be averaged over code to yield

$$\langle u_l(t_R) \rangle = c_1 \frac{q_{M1} q_{M2}}{\sigma_{\eta_1} \sigma_{\eta_2}} \int_{-\infty}^{\infty} \int_{-\infty}^{\infty} G_1(f) G_2(f') \langle A_p(f) A_p^*(f') \rangle_p S_x df df' \quad (5.3)$$

where

$$S_x \equiv \sum_{k=-N}^N e^{2\pi i [\phi_{a1} - \phi_{a2} - \phi_m + (f-f')(t_R + kS) + f'\tau_{a2} - f(\tau_{a1} + L_X S + lS) + \Delta\phi_I]} \quad (5.4)$$

in which differenced instrumental phase is defined by

$$\Delta\phi_I \equiv \phi_{I1} - \phi_{I2} \quad (5.5)$$

Again, $\langle \rangle$ denotes an average over both noise and code. Phase and delay values for L1 and L2 (i.e., with subscripts a1 and a2) are evaluated at the time arguments $t_R + kS - L_X S - lS$ and $t_R + kS$, respectively. Harmonics of the counterrotation function in Eq. (4.3) have been neglected under the assumption that they will average to negligible levels after the correlation sum.

By comparing Eqs. (5.3) and (5.4) with Eqs. (4.7) and (4.8), one can see that an analysis very similar to that in the last section (5.1) can be applied to derive the following correlation function:

$$\langle u_I(t_R) \rangle = A_x e^{2\pi i \phi_d} \int_{-\infty}^{\infty} G_1(f) G_2(f) \left[\frac{\sin(\pi f T_p)}{\pi f T_p} \right]^2 e^{2\pi i [f(\tau_r - l_s) + \Delta\phi_1]} df \quad (5.6)$$

where the amplitude factor is defined by

$$A_x \equiv N_s T_p c_1 \frac{q_{M1} q_{M2}}{\sigma_{\eta 1} \sigma_{\eta 2}} \frac{\sin(\pi \dot{\phi}_d T)}{\pi \dot{\phi}_d T} \quad (5.7)$$

In this expression, the difference phase is defined by

$$\phi_d \equiv \phi_{a1}(t_R) - \phi_{a2}(t_R) - \phi_m(t_R) \quad (5.8)$$

and residual delay by

$$\tau_r \equiv \tau_{a2}(t_R) - \tau_{a1}(t_R) - L_x s \quad (5.9)$$

with both time tagged at the center of the correlation interval, as indicated. To arrive at Eq. (5.6), use has been made of the fact that τ_{a1} and τ_{a2} are nearly equal, usually differing by less than 0.1 ns/s at midlatitudes at present. In addition, a phase effect of the form $\phi_{a1}(l_s + L_x s)$ and a corresponding delay effect of the form $\tau_{a1}(l_s + L_x s)$, where both are caused by lagging of the L1 samples, have been neglected under the assumption that corrections can be applied during processing, if necessary, to remove these accurately modeled effects. (The rates in these corrections can be accurately obtained from the C/A channel.)

5.3 Discussion of the L1*L2 Correlation Function

The L1*L2 correlation function is so similar to the code correlation function in Eq. (4.22) that much of the discussion in Subsection 4.4 applies here, and only the differences need to be outlined. Note that the filters from both channels are present in the L1*L2 correlation integral, rather than the filter for a single channel. This difference in filtering is important for high-accuracy modeling but does not change the essential character of the correlation integral. Because a product of channels is involved, amplitude in the L1*L2 correlation function is scaled downward by the RMS noise from both channels rather than only one. As discussed in Subsection 7.2.1, this effect greatly reduces the SNR for the L1*L2 mode of operation relative to the known-code mode.

The residual delay in Eq. (5.9) is equal to the difference in the L1-P and L2-P delays minus the model delay, $L_x s$, applied to the L1 channel. Since this model delay must be quantized in steps of s , it is adjusted to the value that provides the best possible alignment under the circumstances, namely the alignment that places largest amplitude at the prompt (center) lag of the three correlator lags. Unlike the very small residual delay for code-mode processing, residual delay for the L1*L2 channel can be as large as half a lag (about 25 ns).

The major component of residual phase is given theoretically by Eq. (5.8) and is equal to the difference of the L1-P and L2-P phases minus the model phase. Thus, the phase being tracked consists of the various terms arising from Eqs. (3.15) and (3.16), but differenced between

channels. As in the code-mode correlation function, a small instrumental-phase component can emerge from the correlation integral as a result of the bandpass-phase effect, but this effect will be small if the receiver filters are matched between the L1 and L2 channels. That is, in the P-codeless mode, the bandpass phase $\Delta\phi_1$ is a difference between channels. If the system filters are closely matched, nonlinear phase-versus-frequency variations and receiver delays tend to cancel between channels (i.e., $\Delta\phi_1 \approx 0$ and $\Delta\tau_1 \approx 0$) and therefore are significantly reduced relative to the case of code-mode operation. Even if the filters are exactly matched, however, the difference in the baseband rates for L1 and L2 will prevent exact cancellation.

For the TR receiver, one obtains the theoretical amplitude-versus-delay response shown in Fig. 5-1(a), assuming the dominant filter shape for both the L1 and L2 channels is the baseband Butterworth filter described in Subsection 3.1. Fig. 5-1(b) presents the corresponding phase-versus-delay response. As can be seen, phase around zero delay is nearly constant. For purposes of illustration, a phase offset of about 0.0053 cycles has been introduced at zero delay, as in the corresponding code-mode plot. Again, this offset would be removed in practice by the phase-locked loop and would not appear in the correlation sums.

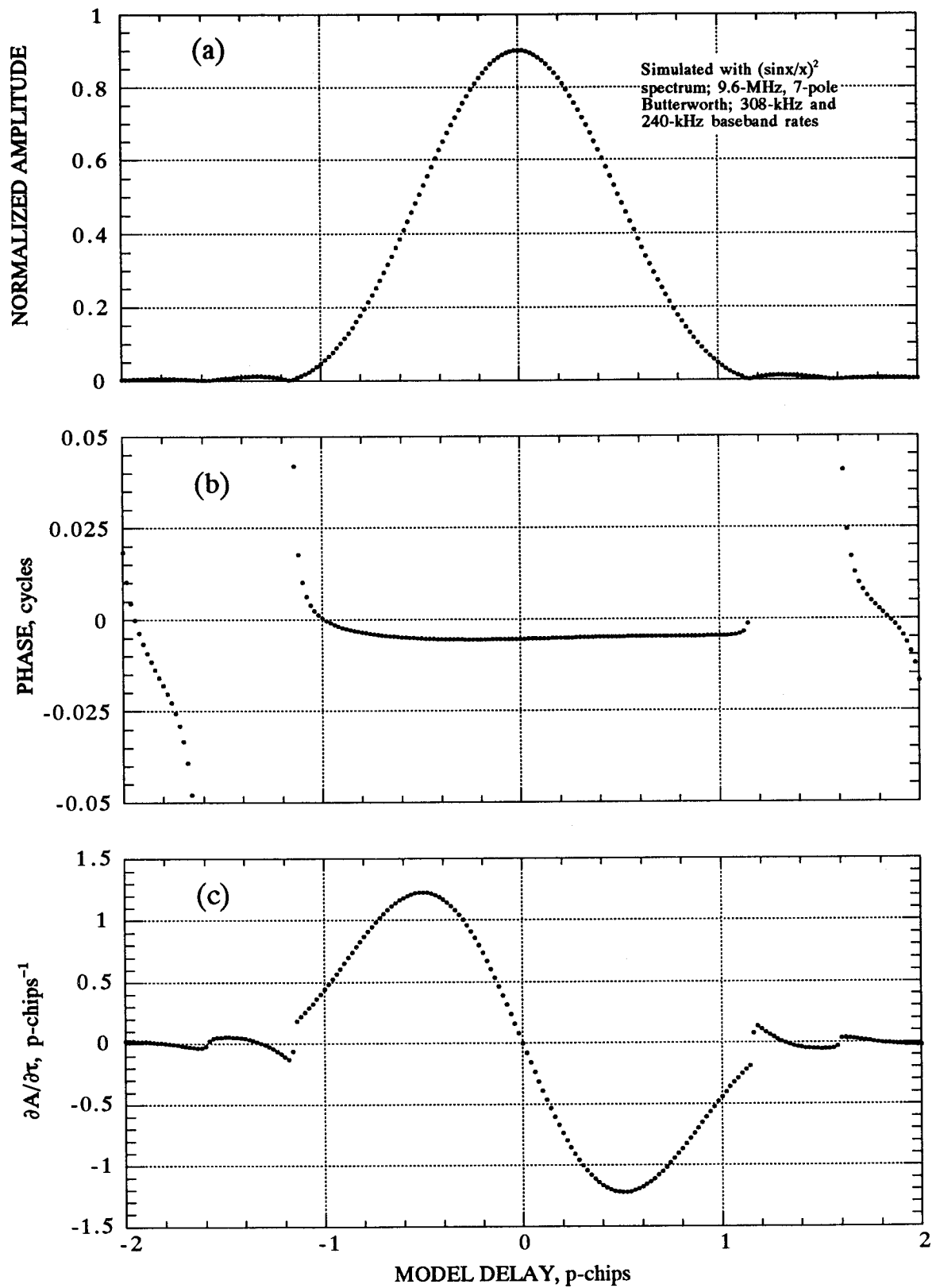


Figure 5-1. L1*L2 Correlation Function for the TurboRogue Receiver with the Analog Front End

SECTION 6

OBSERVABLE EXTRACTION

6.1 Code Mode

6.1.1 Phase Extraction

A measured value of residual phase is obtained by applying an arctangent operation to the components of the complex correlation sum for the prompt lag ($l = 0$):

$$\hat{\varphi}_r = \arctan[\text{IM}(u_0), \text{RE}(u_0)] \quad (6.1)$$

where RE and IM respectively denote real and imaginary parts, and where "hat" over φ is used in Eq. (6.1) and on other observables to denote a measured value computed on the basis of correlation data. As implied by Eq. (4.22), measured residual phase is, on average, theoretically given by

$$\langle \hat{\varphi}_r \rangle = \varphi_d + \bar{\varphi}_I \quad (6.2)$$

where φ_d is the difference phase in Eq. (4.10) and where $\bar{\varphi}_I$ is the "bandpass-averaged value" for nonlinear instrumental phase not accounted for by τ_I .

Measured phase at the center of the correlation interval is computed as the sum of measured residual phase and the model (feedback) phase at interval center:

$$\hat{\varphi}(t_R) = \varphi_m(t_R) + \hat{\varphi}_r \quad (6.3)$$

By computing measured phase in this manner, tracking error is essentially eliminated as an error source in the measured delay. The resulting 20-ms phase values are fit with a quadratic function over successive 1-s intervals in order to reduce data volume and improve statistics. Thus, an aggregate phase value is extracted every second, with a time tag at the center of the 1-s interval. For an earth-fixed antenna, dynamics over a second are typically sufficiently restrained to allow a quadratic to supply an adequate fit.

A theoretical expression for the average value of measured phase is obtained by combining Eqs. (3.1), (3.15), (3.16), (4.10), (6.2) and (6.3), which yields

$$\varphi(t_R) = \langle \hat{\varphi}(t_R) \rangle = (f_L - f_h)t_R - \varphi_{hd} - f_L(\tau_g + \tau_t - \tau_s + \tau_R) + \varphi_s + \varphi_e(f_L) + \bar{\varphi}_I \quad (6.4)$$

where all quantities are time tagged at interval center, t_R . As implied by this equation, the intentional offset in the downconversion frequency, $f_L - f_h$, which is accurately known, must be removed from measured phase in order to obtain a phase-delay estimate that is nearly free of instrumental rate offset. Measured phase delay is therefore extracted with the operation

$$\hat{\tau}_\varphi(t_R) = [(f_L - f_h)t_R - \hat{\varphi}(t_R)]/f_L \quad (6.5)$$

Based on Eqs. (6.4) and (6.5), the theoretical estimate for measured phase delay, on average, is given by

$$\tau_{\phi}(t_R) = \langle \hat{\tau}_{\phi}(t_R) \rangle = \tau_g + \tau_t - \tau_s + \tau_R + [\Phi_{hd} - \bar{\Phi}_I - \Phi_s - \Phi_e(f_L)]/f_L \quad (6.6)$$

where all quantities are evaluated at the center of the correlation interval and where the ionospheric phase, Φ_e , is evaluated at frequency f_L (i.e., at f_{L1} or f_{L2}). Thus, measured phase delay contains the following terms: geometric delay, troposphere delay, satellite-clock offset, a receiver-clock offset, a downconversion phase drift relative to nominal LO offset, bandpass-averaged receiver phase, a satellite phase offset, and ionospheric phase.

6.1.2 Delay Extraction

Correlation sums are accumulated over 1 s before being analyzed to extract residual delay. On the basis of these 1-s sums, measured residual delay can be computed from observed correlation amplitudes using the equation

$$\hat{\tau}_r = k_p \frac{A_+ - A_-}{A_0} \quad (6.7)$$

where A_- , A_0 , and A_+ are the correlation amplitudes for the early, prompt, and late lags ($l = -1, 0, +1$), respectively, and k_p is a computed constant (see next paragraph) that gives residual delay the units of chips. The amplitude for each lag is computed on the basis of the real and imaginary components of the correlation sums with the projection operation:

$$A_l = \cos \hat{\phi}_r \text{RE}[u_l] + \sin \hat{\phi}_r \text{IM}[u_l] \quad (6.8)$$

where $\hat{\phi}_r$ is residual phase computed for the prompt lag according to Eq. (6.1). Based on the assumption that residual phase is essentially the same for all lags, this algorithm estimates amplitude for the early and late lags as the projection along the "direction" in the complex plane computed from the higher-SNR prompt lag. For the prompt lag, the algorithm yields the root-sum-square (RSS) of the real and imaginary components. When residual phase is large (e.g., 45 degrees), both components of a complex correlation sum influence the computed amplitude in a weighted fashion, with the largest component possessing the greatest weight. Furthermore, for the two important side lags, the noise on those correlation sums enters the computed delay in a linear fashion, and a better estimate is therefore obtained at low SNR values.

Either observed response or theoretical calculation based on an estimated system bandpass filter can be used to calculate the constant k_p under the assumption that the residual delay is very small (i.e., small enough to make the amplitude difference in Eq. (6.7) approximately proportional to residual delay). Since the accuracy required for k_p is not demanding, the theoretical approach has been used. Based on amplitude derivatives shown in Fig. 4-2(c) at the 50-ns side lags, the P-channel result is a k_p value of 0.37 for the TurboRogue receiver. (Specifically, the theoretical value for k_p is approximately $0.9/(1.28 + 1.15)$, where 0.9 is the prompt amplitude obtained from Fig. 4-2(a) and the two values in the denominator are the derivatives at ± 50 ns.) The allowed error in this constant can be relatively large as long as the residual delay is small. For example, an error of 10% (i.e., about 0.04) causes an error of only 0.0001 p-chip (0.3 cm) in delay when the residual delay has a steady-state value of 0.001 chip. Because of the C/A-phase-driven feedback, steady-state residual delay is primarily due to the influence of the ionosphere and can reach 0.001 p-chip in extreme cases for an earth-fixed receiver, given a secondary 1-s loop of first order for tracking delay variations relative to C/A-derived fast feedback.

Residual delay values computed with Eq. (6.7) will correspond to the measure of delay that equalizes the early and late amplitudes. In the current version of the TR receiver with its unsymmetric bandpass filter in the analog front end, the resulting delay is not exactly equal to the delay that produces peak amplitude. For the highly digital front end described in Appendix A of this document, these two measures of delay would be more nearly equal due to the greater filter symmetry found in that implementation. (Either measure of delay could theoretically be used in GPS applications since they differ only by an additive constant that can be removed either by double differencing or by calibration.)

Once residual delay has been extracted, 1-s measured delay is computed as the sum of measured residual delay and model delay at interval center:

$$\hat{\tau}(t_R) = \tau_m(t_R) + \hat{\tau}_r \quad (6.9)$$

As with measured phase, this process essentially removes any tracking error in measured delay. The expectation value of measured residual delay is represented theoretically by Eq. (4.24). A theoretical expression for the average value of measured delay is obtained by combining Eqs. (3.14), (4.24), and (6.9), which yields

$$\tau(t_R) = \langle \hat{\tau} \rangle = \tau_a \equiv \tau_g + \tau_t - \tau_s + \tau_R + \tau_e + \tau_i \quad (6.10)$$

where all quantities are time tagged at the center of the 1-s interval, t_R . Thus, measured delay is the sum of the following terms: geometric delay, troposphere delay, satellite-clock offset, receiver-clock offset, ionospheric delay, and receiver delay.

To compress data volume and collect statistics, these 1-s delay values can be combined over longer time intervals by a least-squares fit or carrier-aided averaging.

6.2 P-Codeless Mode

6.2.1 Phase Extraction

In the P-codeless mode, measured residual phase, $\hat{\varphi}_r$, is estimated by first adding the imaginary components of the correlation sums across the three lags and then normalizing to units of cycles:

$$\hat{\varphi}_r = \frac{1}{2\pi A_N^x} \text{IM} \left(\sum_l^3 u_l \right) \quad (6.11)$$

where A_N^x is a 3-lag-sum amplitude mapped from C/A amplitude. Unlike the code mode, addition across lags makes sense here since the noise on the sums is uncorrelated between lags (see Subappendix C.3.2). Furthermore, unlike prompt amplitude, effective amplitude for the sum is nearly independent of residual delay, which can be as large as 0.25 p-chip when in the P-codeless mode. As a result, effective SNR on the composite is about 1.7 to 3 dB better than the SNR on the prompt lag alone. A small correction is needed to account for the slight dependence of phase on lag (about 0.015 cycles/lag, see Subsection 5.2) caused by applying lags to L1 with its sizable baseband carrier frequency (about 308 kHz). The effect of these phase shifts can be accurately modeled and removed on the basis of observed L1 carrier frequency, thereby referencing measured phase to the prompt lag.

As implied by Eq. (5.6), measured residual phase is, on average, theoretically given by

$$\langle \hat{\varphi}_r \rangle = \varphi_d + \overline{\Delta\varphi_I} \quad (6.12)$$

where φ_d is the difference phase given by Eq. (5.8) and where $\overline{\Delta\varphi_I}$ is the bandpass-averaged value for instrumental phase, exclusive of instrumental delay effects, differenced between L1 and L2. Measured phase for the L1*L2 channel at the center of the correlation interval is computed as the sum of measured residual phase and model (feedback) phase:

$$\hat{\varphi}_x(t_R) = \varphi_m(t_R) + \hat{\varphi}_r \quad (6.13)$$

Again, by computing measured phase in this manner, tracking error is essentially eliminated. A theoretical expression for the average value of measured phase is obtained by combining Eqs. (5.8), (6.12), and (6.13), which yields

$$\varphi_x(t_R) = \langle \hat{\varphi}_x \rangle = \varphi_{a1}(t_R) - \varphi_{a2}(t_R) + \overline{\Delta\varphi_I} \quad (6.14)$$

This equation can be reformulated through use of Eqs. (3.1), (3.15), and (3.16):

$$\varphi_x(t_R) = (\Delta f_L - \Delta f_h)t_R - \Delta\varphi_{hd} - \Delta f_L(\tau_g + \tau_t) + f_{L2}(\tau_{R2}^p - \tau_{S2}^p) - f_{L1}(\tau_{R1}^p - \tau_{S1}^p) + \Delta\varphi_s + \Delta\varphi_e + \overline{\Delta\varphi_I} \quad (6.15)$$

where the superscript p refers to P channel, where all quantities are time tagged at interval center, and where Δ denotes a difference between the L1-P and L2-P channels, in the order L1 minus L2. As one would expect, differenced phase is the same general form as the single-channel phase in Eq. (6.4) but with each term differenced between channels.

To obtain an estimate of L2 phase, the measured difference phase obtained from the operation in Eq. (6.13) is subtracted from the L1 phase simultaneously measured in the C/A channel:

$$\hat{\varphi}_{L2}^x = \hat{\varphi}_{L1}^c - \hat{\varphi}_x \quad (6.16)$$

where c denotes C/A channel and x denotes L1*L2 processing. Based on Eq. (6.4) as applied to the C/A channel and on Eq. (6.15), this measured phase, on average, is represented theoretically by

$$\varphi_{L2}^x = \langle \hat{\varphi}_{L2}^x \rangle = (f_{L2} - f_{h2})t_R - \varphi_{hd2} - f_{L2}(\tau_g + \tau_t - \tau_{S2}^p + \tau_{R2}^p) + \varphi_{S2}^p + \varphi_e(f_{L2}) + \overline{\varphi_{I2}^p} + \psi \quad (6.17)$$

where the "correction" term is defined by

$$\psi = -f_{L1}(\tau_{S1}^p - \tau_{S1}^c) + (\varphi_{S1}^c - \varphi_{S1}^p) + (\overline{\varphi_{I1}^c} - \overline{\varphi_{I2}^p} - \overline{\Delta\varphi_I}) \quad (6.18)$$

All quantities are evaluated at interval center, t_R , and it has been assumed that the following quantities are essentially identical for the L1-C/A and the L1-P channels: carrier frequency, receiver LO phase, receiver-clock error, geometric delay, tropospheric delay, and ionospheric phase. In practice, the satellite-clock error and satellite phase offset will be different for L1-C/A and L1-P, and these differences have been accounted for in Eq. (6.18), with a superscript to denote C/A or P channel. Similarly, Eq. (6.18) accounts for receiver instrumental phase.

Comparison of the theoretical expressions for L2 phase in the code mode, Eq. (6.4), and in the P-codeless mode, Eq. (6.17), shows that, under the specified assumptions, measured L2 phase should be identical in the two modes except for the terms in ψ .

L2 phase delay is calculated as prescribed by Eq. (6.5), with L2 values for f_L and f_h . The resulting phase delay, on average, is represented theoretically by

$$\tau_{\phi}^x(t_R) = \langle \hat{\tau}_{\phi}^x(t_R) \rangle = \tau_g + \tau_t - \tau_{S2}^p + \tau_{R2}^p + [\varphi_{hd2} - \overline{\varphi}_{12}^p - \varphi_{S2}^p - \varphi_e(f_{L2}) - \psi]/f_{L2} \quad (6.19)$$

where all quantities are evaluated at interval center. Except for the instrumental terms, this expression is identical to Eq. (6.6).

6.2.2 Delay Extraction

The P-codeless technique extracts early, prompt, and late amplitudes from the correlation sums on the basis of the algorithm described in Subsection 6.1.2. Fig. 5-1 presents the theoretical dependence of amplitude on delay for L1*L2, given a 9.6-MHz Butterworth filter. Residual delay for L1*L2 cannot be extracted with sufficient accuracy by means of the algorithm, Eq. (6.7), used in the code mode because the misalignment of the L1-P and L2-P correlation is not necessarily small and can be as large as 0.5 sample interval (about 25 ns). Instead, as illustrated in Fig. 6-1, a normalized difference of the early and late amplitudes (defined as the balance ratio) drives a table lookup of the residual delay. The numerical values in the table can be obtained through modeling and/or calibration of the amplitude response. For highest accuracy, separate calibration of this table is required for each receiver. The calibration is carried out by forcing the table lookup to produce the same measured values for P2 - P1 delay as the code mode. To illustrate the shape of the table-lookup function, Fig. 6-2 presents theoretical results for residual delay as a function of the balance ratio, given the 9.6-MHz Butterworth filter defined in Subsection 3.1. It is estimated that the accuracy of this table lookup can fall between 2 and 10 cm, depending on the effort applied to calibrate the table.

Total measured P2 - P1 delay with a time tag at interval center is computed by adding the resulting residual delay to the feedback model delay L_x :

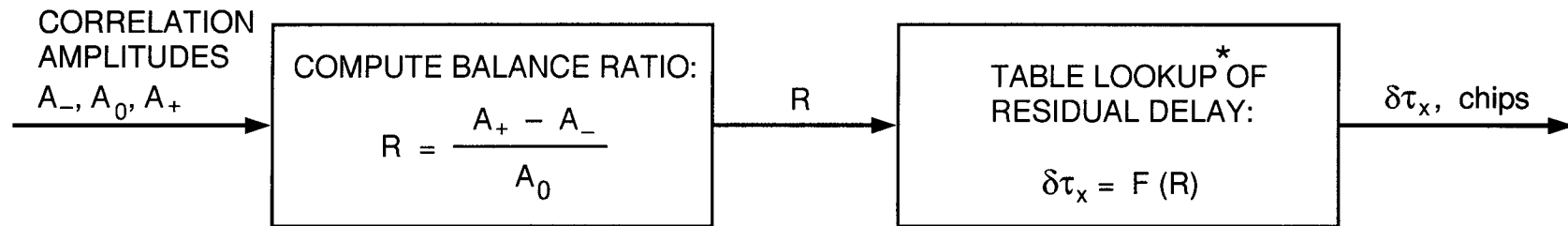
$$\hat{\tau}_x = \hat{\tau}_r + L_x s \quad (6.20)$$

A theoretical expression for the averaged value of measured difference delay is obtained by combining Eqs. (5.9) and (6.20), which yields

$$\tau_x = \langle \hat{\tau}_x \rangle = \tau_{a2}(t_R) - \tau_{a1}(t_R) \quad (6.21)$$

Substituting Eq. (3.14) twice, each time with appropriate subscript, yields

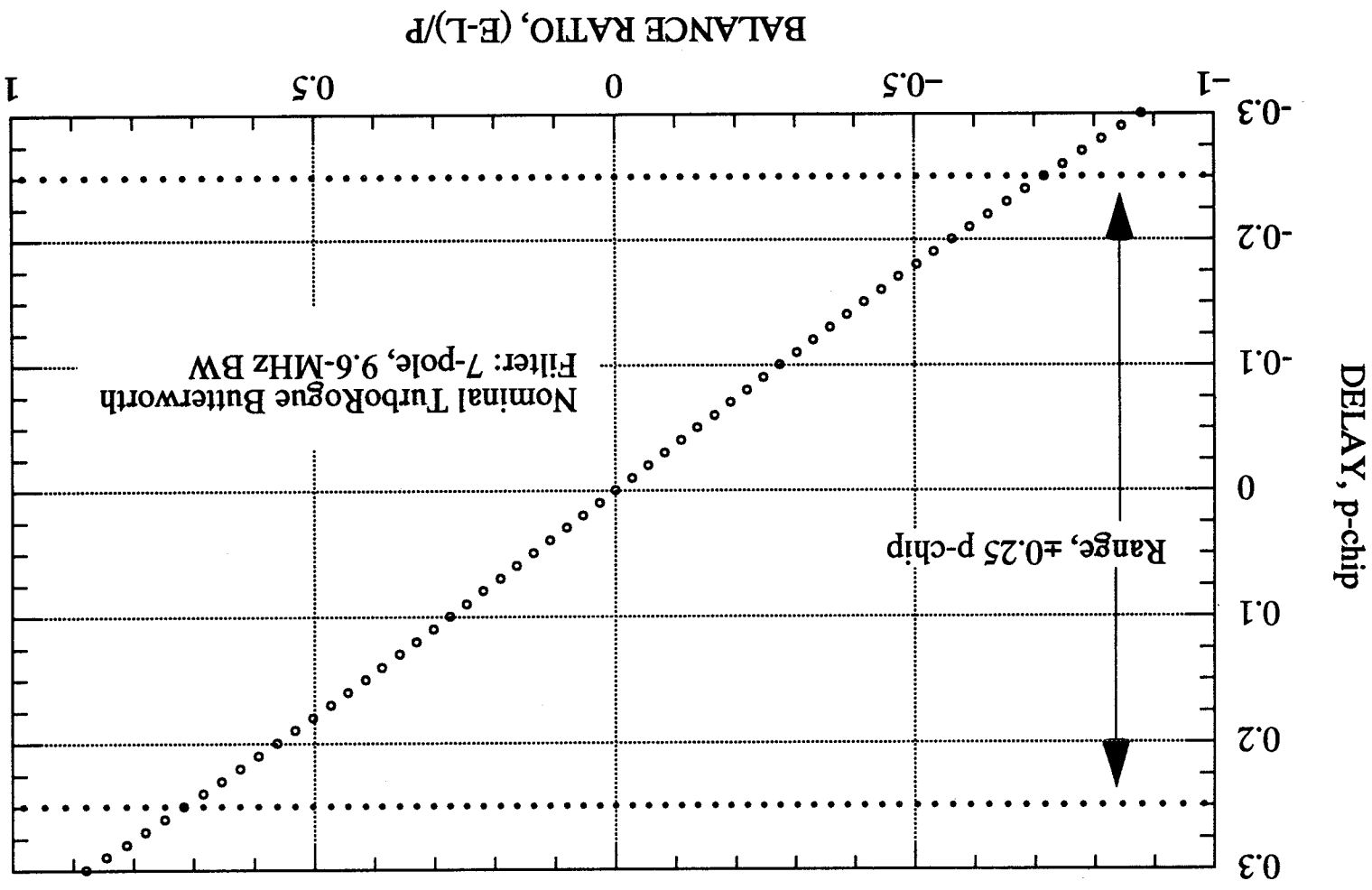
$$\tau_x = \tau_{S1}^p - \tau_{S2}^p + \tau_{R2}^p - \tau_{R1}^p + \tau_{e2} - \tau_{e1} + \tau_{12}^p - \tau_{11}^p \quad (6.22)$$



* CALIBRATED TABLE-LOOKUP FUNCTION F DEPENDS ON BANDPASS SHAPE

Figure 6-1. Table Lookup Operations for the L1*L2 Delay

Figure 6-2. Table Lookup Function for the L1*L2 Delay



6-7

16

where the superscript p refers to P channel and where all quantities are evaluated at interval center, t_R . It is assumed the geometric and tropospheric delays are identical for the two channels and have differenced out. In order, the remaining terms are the difference delays due to satellite code clocks, receiver sampler clocks, ionosphere, and instrumental delays. For accurate measurements of the ionospheric delay difference, calibrations are generally required to remove the overall delay contributed by terms other than the ionosphere.

L2-P group delay is estimated by adding the measured L1*L2 delay to the concurrently measured C/A group delay:

$$\hat{\tau}_{p2} = \hat{\tau}_{c/a} + \hat{\tau}_x \quad (6.23)$$

A theoretical expression for this measured delay is obtained by combining Eqs. (6.22) and (6.10) (with a subscript to represent L1-C/A):

$$\tau_{p2} = \langle \hat{\tau}_{p2} \rangle = \tau_g + \tau_t - \tau_{s2}^p + \tau_{k2}^p + \tau_{e2} + \tau_{i2}^p + \tau_\Delta \quad (6.24)$$

where the correction term is defined by

$$\tau_\Delta = (\tau_{s1}^p - \tau_{s1}^c) - (\tau_{i1}^p - \tau_{i1}^c) \quad (6.25)$$

All quantities are evaluated at interval center, t_R . It has been assumed that the receiver-clock error and ionospheric delay are the same for L1-C/A and L1-P. Note that the P-codeless group delay for L2-P in Eq. (6.24) has the same form as the code-mode measurement of the same quantity in Eq. (6.10), except for the differences in Eq. (6.25) due to satellite clocks and receiver delays. In practice, the L1-C/A and L1-P codes (i.e., "satellite clocks") can be misaligned by a few nanoseconds as they leave the satellite, and the TR instrumental delay can be on the order of 1-ns smaller for C/A than for P. In practice, careful calibration of these two offsets should be carried out if one requires an accurate correspondence between the L2-P delay from the code mode and the L2-P delay from the P-codeless mode.

SECTION 7

SYSTEM-NOISE ANALYSIS

7.1 Code Mode

7.1.1 Signal-to-Noise Ratio

The signal-to-noise-ratio analysis presented in this section is based on the analog front end described in Section 3, with two-level sampling. The voltage SNR for a complex correlation sum is defined as the maximum correlation amplitude (i.e., RSS of components for prompt lag) divided by the RMS noise on either component. For perfect lock in phase and delay in which residual phase, phase rate, and delay are all equal to zero, Eq. (4.22) predicts that the maximum amplitude A_M at the prompt lag is given by

$$A_M = N_s T_p c_1 \frac{q_M}{\sigma_\eta} \int_{-\infty}^{\infty} G(f) \left[\frac{\sin(\pi f T_p)}{\pi f T_p} \right]^2 e^{2\pi i \delta\phi_1} df \quad (7.1)$$

where $\delta\phi_1$ is the nonlinear phase-frequency response of the receiver filter but with an integral-averaged value subtracted (by the DPLL) so that the integral is real.

The integral, which is a measure of the maximum correlation of the filtered baseband signal with the pure P-code sequence generated by the receiver, is approximately proportional to the square root of signal power at baseband. Based on this proportionality, one can set up the following relationship between the correlation integral and signal power:

$$\frac{T_p}{\sigma_\eta} \int_{-\infty}^{\infty} G(f) \left[\frac{\sin(\pi f T_p)}{\pi f T_p} \right]^2 e^{2\pi i \delta\phi_1} df = \sqrt{\frac{2\alpha_f P_s}{P_N}} \quad (7.2)$$

where σ_η^2 is proportional to the average noise power P_N entering the sampler *after* receiver filtering, and where P_s is the signal power per quadrature component that would have entered the sampler if the receiver had not filtered out any frequency components of the signal. The factor of 2 under the square root accounts for the two quadrature components, while the factor α_f accounts for loss in signal power due to receiver filtering. Numerical calculations indicate that α_f is approximately 0.9 for the P channels and 0.99 for the C/A channel, given the analog front end described in Section 3. This method of representing the maximum correlation has been adopted in order to explicitly formulate Eq. (7.1) in terms of a measure of signal power that is independent of the shape of TR filters and to explicitly account for the loss due to receiver filtering.

When Eq. (7.2) is substituted in Eq. (7.1), the maximum amplitude becomes

$$A_M = N_s c_1 q_M \sqrt{2 \frac{\alpha_f P_s}{P_N}} \quad (7.3)$$

The ratio, $\alpha_f P_s/P_N$, can be thought of as the single-sample power SNR per quadrature component at baseband after accounting for filtering but neglecting quantization loss.

Maximum voltage SNR is computed by dividing maximum amplitude by the RMS noise, σ_u , on the either component of the complex sum:

$$\text{SNR}_V = \frac{A_M}{\sigma_u} \quad (7.4)$$

Based on Eqs. (7.3) and (C.25), the maximum voltage SNR in the case of quadrature sampling becomes

$$\boxed{\text{SNR}_V = L_c L_s \sqrt{2 N_s \frac{\alpha_f P_s}{P_N}}} \quad (7.5)$$

where N_s is the number of samples correlated, not counting samples lost during the dead time between correlation intervals, and where the factors L_c and L_s are the losses due to quantization of counterrotation sinusoids and sampling quantization, respectively. The loss caused by three-level quantization of the counterrotation sinusoids is defined as

$$L_c \equiv \frac{c_1}{\sqrt{1.5}} = \frac{1.176}{\sqrt{1.5}} = 0.96 \quad (7.6)$$

or 0.35 dB. The sampling quantization loss is defined by

$$L_s \equiv \frac{q_M}{\sigma_{\tilde{\eta}}} \quad (7.7)$$

Based on Eqs. (B.15) and (B.16), this loss is

$$L_s = \sqrt{\frac{2}{\pi}} = 0.798 \quad (7.8)$$

or 2 dB for the two-level sampling implemented in the current TR receiver.

The term N_s in Eq. (7.5) can be thought of as the SNR increase due to N_s independent samples. Ideal sampling is assumed; i.e., the sample rate and bandpass are such that the noise on sample points is essentially independent between points. For nonquadrature sampling, the result in Eq. (7.5) decreases by $\sqrt{2}$. Total processing loss due to the receiver is approximately equal to $L_c L_s \sqrt{\alpha_f} \sqrt{18/20}$ or $0.96 \times 0.798 \times \sqrt{0.9} \times \sqrt{18/20} = 0.69$ (3.2 dB), where 18/20 accounts for samples lost during the dead time.

A *nominal* SNR for the TurboRogue receiver in the L1-P channel is calculated as follows: The total noise power *at RF* at insertion (i.e., including antenna gain but before front-end amplification) is given by

$$P'_N = k_B T_s W \quad (7.9)$$

where k_B is Boltzmann's constant, T_s is system (total) noise temperature, and W is the effective double-sided noise bandwidth. For a *nominal* system temperature of 200 K and a noise bandwidth of 19.2 MHz, the noise power becomes

$$P'_N = 1.38 \times 10^{-23} \text{ w/K-Hz} \times 200 \text{ K} \times 19.2 \text{ MHz} \quad (7.10)$$

or

$$P'_N = 5.3 \times 10^{-14} \text{ watts} \quad (7.11)$$

The noise bandwidth of $2 \times 9.6 \text{ MHz} = 19.2 \text{ MHz}$ reflects the ultimate double-sided passband of the front end.

According to GPS specifications, *nominal* signal power collected by an antenna with 0-dB gain is -163 dBW for the L1-P signal so that the signal power at insertion at RF for a 3-dB-gain antenna is

$$P'_S = 10^{-16} \text{ watts} \quad (7.12)$$

Since the receiver amplifies signal and noise by the same factor in transit from RF to baseband, and since downconversion does not change the ratio of signal to noise, the baseband power ratio in Eq. (7.5) is the ratio of the numbers from Eqs. (7.11) and (7.12):

$$\frac{P_S}{P_N} = \frac{P'_S}{P'_N} = 0.0019 \quad (7.13)$$

For a 1-s integration time consisting of 50 intervals of 18-s duration and a sample rate of about 20 MS/s, Eq. (7.5) predicts a *nominal* TurboRogue voltage SNR of about 190, given the losses specified above. For the latest version of TurboRogue, typical zenith SNRs for L1-P are about 600, which is larger due to the effect of a 7-dB antenna gain at zenith, 110-K system temperature, and higher-than-nominal signal strength. (Signal strengths are reportedly 3 to 5 dB greater than nominal.)

Similar calculations can be carried out for the C/A and P2 channels. As a consequence of differences in transmitted power, the *nominal* C/A SNR is approximately $\sqrt{2}$ higher and the nominal L2-P SNR approximately $\sqrt{2}$ lower than the L1-P result.

7.1.2 System-Noise Error in Phase

The noise on the correlation sums propagates to noise in extracted phase. By propagating noise through the arctangent operation in Eq. (6.1), one can show that the system-noise error in phase (1σ , in cycles) is given by

$$\sigma_\phi \approx \frac{1}{2\pi \text{SNR}_{20}} \quad (7.14)$$

where SNR_{20} , as computed in Eq. (7.5), is the 18-ms voltage SNR entering the arctangent. For a 1-s observable, the phase error can be computed by substituting the SNR from Eq. (7.5) in Eq. (7.14) but increasing the error by an additional factor of 1.5. The factor of 1.5 is the degradation suffered relative to a straight average when a quadratic fit is applied to fifty 20-ms phase values extracted by the phase-locked loop over the second. Based on the *nominal* 1-s SNR of 190 presented in the Subsection 7.1.1, the system-noise error in L1-P phase therefore becomes 0.00126 mcycles (0.024 cm) for a 1-s integration time.

After further increasing the integration time by means of an additional quadratic fit over N_T seconds ($N_T > 2$), the system-noise error is decreased by a factor of $\sqrt{N_T} / 1.5$. The additional factor of 1.5 is the degradation due to the second quadratic fit.

7.1.3 System -Noise Error in Group Delay

System-noise error in delay is calculated by propagating errors through Eqs. (6.7) and (6.8). To first order, one can easily show on the basis of Eq. (6.8) that the amplitude errors for the side lags are independent of the error in $\hat{\phi}_r$, with RMS values given by

$$\sigma_A^2 = (\sin \hat{\phi}_r)^2 \sigma_u^2 + (\cos \hat{\phi}_r)^2 \sigma_u^2 \quad (7.15)$$

which leads to

$$\sigma_A^2 = \sigma_u^2 \quad (7.16)$$

where σ_u is the 1- σ error in either component of the complex correlation sum. This result assumes negligible correlation between the noise on the quadrature components of the correlation sums as derived in Eq. (C.23).

Noise on the three amplitudes propagates through Eq. (6.7) to create a delay error given by

$$\delta\tau_r = k_p \frac{\delta A_+ - \delta A_-}{A_0} - \tau_r \frac{\delta A_0}{A_0} \quad (7.17)$$

where δ denotes deviation from the actual value. Because residual delay, τ_r , is small during in-lock code-mode operation, the δA_0 term in this expression can be neglected. The RMS of the delay error in Eq. (7.17) becomes

$$\sigma_\tau = \sqrt{2} k_p \frac{\sigma_A}{A_0} [1 - \Lambda(2)]^{1/2} \quad (7.18)$$

where Λ is the correlation of noise between lags with $l - l' = 2$ (see Eq. (C-26)). If the prompt lag has peak amplitude, Eqs. (7.4), (7.16), and (7.18) can be used to show

$$\sigma_\tau = \frac{\sqrt{2} k_p}{\text{SNR}_v} \quad (7.19)$$

again with units of chips. The correlation, $\Lambda(2)$ has been set to zero, as explained in Subsection C.2.2. For the *nominal* 1-s SNR of 190 obtained above for L1-P and $k_p = 0.37$, the delay error is equal to approximately 0.0028 p-chip (8.3 cm) for the L1-P channel for a 1-s integration time. For the aforementioned observed zenith SNR of 600, the delay error is 2.6 cm.

If delay is averaged over a longer time interval of length N_T seconds by means of carrier-aided averaging, the error decreases by a factor of $\sqrt{N_T}$. For 5 min, the error is a factor of $\sqrt{300}$ smaller or 0.15 cm for the maximum observed SNR.

7.2 P-Codeless Mode

7.2.1 Signal-to-Noise Ratio

The definition of signal-to-noise ratio for the L1*L2 channel is the same as that for the code channels presented in Subsection 7.1.1. By using an analysis that parallels the steps in that subsection, one can derive a corresponding expression for L1*L2 voltage SNR. Based on Eqs. (5.6) and (5.7), maximum correlation amplitude is given by

$$A_M = N_s T_p c_1 \frac{q_{M1} q_{M2}}{\sigma_{\eta 1} \sigma_{\eta 2}} \int_{-\infty}^{\infty} G_1(f) G_2(f) \left[\frac{\sin(\pi f T_p)}{\pi f T_p} \right]^2 e^{2\pi i \delta \phi_1} df \quad (7.20)$$

Analogous to Eq. (7.2), the correlation integral is related to satellite power by

$$\frac{T_p}{\sigma_{\eta 1} \sigma_{\eta 2}} \int_{-\infty}^{\infty} G_1(f) G_2(f) \left[\frac{\sin(\pi f T_p)}{\pi f T_p} \right]^2 e^{2\pi i \delta \phi_1} df = \sqrt{\frac{4 \alpha_f P_{S1} P_{S2}}{P_{N1} P_{N2}}} \quad (7.21)$$

where $\sigma_{\eta k}^2$ is proportional to the average noise power P_{NK} entering the sampler for channel Lk after receiver filtering, where P_{sk} is the average signal power at baseband for the P signal in channel Lk, as defined following Eq. (7.3). The phase, $\delta \phi_1$, corresponds to the definition for Eq. (7.1) but is based here on the difference of receiver phase between P channels. Again, α_f represents the loss due to receiver filtering. Numerical evaluation based on the adopted Butterworth filter described in Subsection 3.1 indicates that α_f is approximately equal to 0.9.

When Eq. (7.21) is substituted in Eq. (7.20), the maximum amplitude becomes

$$A_M = N_s c_1 q_{M1} q_{M2} \sqrt{4 \alpha_f \frac{P_{S1} P_{S2}}{P_{N1} P_{N2}}} \quad (7.22)$$

Note that Eq. (7.22) has a factor of 4 under the square root rather than the factor of 2 in Eq. (7.3). This increase accounts for the fact that four quadrature components contribute to the L1*L2 correlation rather than two.

Maximum voltage SNR found at perfect alignment of the L1 and L2 signals is obtained by substituting Eqs. (7.22) and (C.35) in Eq. (7.4), which yields

$$\boxed{\text{SNR}_x = L_c L'_s \sqrt{2 N_s \alpha_f \frac{P_{S1} P_{S2}}{P_{N1} P_{N2}}}} \quad (7.23)$$

where all quantities have the same definitions as in Subsection 7.1.1, and the subscript numbers refer to the L1-P and L2-P channels. Since the counterrotation sinusoids are again quantized to three levels, the quantization loss, L_c , again has the value derived in Eq. (7.6). The sampling quantization loss, however, is given by

$$L'_s \equiv \frac{q_{M1} q_{M2}}{\sigma_{\tilde{\eta} 1} \sigma_{\tilde{\eta} 2}} \quad (7.24)$$

Based on the results in Eqs. (B.15) and (B.16), this loss becomes

$$L'_s = \frac{2}{\pi} = 0.637 \quad (7.25)$$

given two-level sampling quantization in both the L1 and L2 channels.

The *nominal* L1*L2 SNR for the TurboRogue receiver with the analog front end can be calculated on the basis of the parameter values in Subsection 7.1.1. When the power ratio for P1 in Eq. (7.13) and the above losses are substituted in Eq. (7.23), the maximum voltage SNR on the prompt lag for a 1-s integration is approximately 4.7 where the value for P_{S2}/P_{N2} has been set equal to 1/2 of the same quantity for L1 to reflect the nominal decrease in transmitted power for L2. Three-lag combining improves the effective SNR by 1.8 dB for phase (see Subsection 7.2.2), which changes the above SNR value to 5.8 for phase tracking and estimation.

Actual SNRs are considerably better than these nominal SNRs. With the current version of TR, the peak observed 1-s SNRs are approximately 75 instead of 4.7, and 90 instead of 5.8. As mentioned in Subsection 7.1.1, the increase is a result of lower system temperature, higher antenna gain, and larger-than-nominal source strength than assumed in the nominal calculation.

A useful ratio of SNRs is defined by

$$R_{cx} \equiv \frac{SNR_{v1} SNR_{v2}}{SNR_x} \quad (7.26)$$

where SNR_{vk} is the 1-s voltage SNR at the prompt lag for channel Lk in the code mode and SNR_x is the 1-s voltage SNR at the prompt lag in the P-codeless mode. This ratio, which is a good check of receiver health, should be nearly constant over a satellite pass. Eqs. (7.5) and (7.23) lead to the expression

$$R_{cx} = L_c \sqrt{2 \alpha_f N_s} \quad (7.27)$$

which becomes

$$R_{cx} = 0.96 \sqrt{2 \times 0.9 \times 20.456 \times 10^6 \text{ MS/s} \times 0.018 \text{ s} \times 50} \approx 5500 \quad (7.28)$$

for the TurboRogue receiver. It has been assumed that a 1-s integration contains fifty 18-ms intervals. Observed ratios will deviate slightly from this approximate value. Unlike the assumption behind this result, noise is slightly correlated between 20.456-MHz sample points. Further, the observed ratio is based on an estimate of peak prompt L1*L2 amplitude, which is obtained by combining correlation amplitudes for the three lags and is therefore corrupted by errors in modeling amplitude dependence on lag. (In practice, the amplitude at the prompt lag in the L1*L2 channel is not peak amplitude; peak amplitude must be inferred from the three amplitudes.) Preliminary measurements have produced an observed ratio of approximately 5000 (C.E. Dunn, 1994).

7.2.2 System-Noise Error in Phase

As discussed in Subsection 6.2.1, residual phase is extracted by means of a sine phase extractor applied to the sum of the Q correlation sums for the three lags. Relative to peak amplitude, the combined amplitude is approximately $1.0 + 2 \cdot 0.563 = 2.13$, given side amplitudes of about 0.563, as suggested in Fig. 5-1. Since noise on the correlation sums is uncorrelated between lags (see Subappendix C.3.2 of this document), noise on the combined sums is $\sqrt{3}$ larger than the noise for any given lag. Thus, combining lags improves voltage SNR by about $2.13/1.732 = 1.23$, or 1.8 dB, relative to the phase error at the peak amplitude alone. (Since the prompt lag is not necessarily at peak amplitude, combining lags generally improves SNR by even more than 1.8 dB relative to the prompt-lag SNR—by as much as another 1.2 dB for a total gain as large as 3 dB.) To compute system-noise error in phase, voltage SNR from Eq. (7.23) can be substituted in Eq. (7.14) and adjusted by the 1.8-dB SNR increase. Based on the *nominal* 1-s SNR of 4.7 computed at the correlation peak amplitude in Subsection 7.2.1, the 1-s system-noise error in $L1 \cdot L2$ phase becomes 0.028 cycle or 0.67 cm for a 1-s integration time, after the aforementioned 1.8-dB increase in SNR. (There is no loss of 1.5 for $L1 \cdot L2$ phase since C/A-aided averaging compresses $L1 \cdot L2$ phase rather than a quadratic fit.) Again, in practice, actual errors are considerably smaller than this nominal error. For the zenith SNR of 90 quoted in Subsection 7.2.1 for phase, the 1-s error is approximately 0.04 cm.

7.2.3 System-Noise Error in Delay

As discussed in Subsection 6.2.2 and illustrated in Fig. 6-1, delay extraction is based on a prompt-amplitude-normalized difference of early and late amplitudes. For the purpose of estimating system-noise error in delay, the table lookup in Fig. 6-1 can be approximated by Eq. (6.7) with a k_p value of 0.37. When the system-noise errors in amplitude are propagated through Eq. (6.7), one obtains the error presented in Eq. (7.17). The RMS (i.e., $1-\sigma$) error is obtained by squaring the error in Eq. (7.17), averaging over noise, and taking the square root. Since the amplitude errors due to the system noise are uncorrelated between lags, the $1-\sigma$ delay error becomes

$$\sigma_\tau \approx k_p \frac{\sigma_A}{A_0} \sqrt{2 + \left[\frac{A_+ - A_-}{A_0} \right]^2} \quad (7.29)$$

in units of p-chips.

This expression for delay error is a weak function of the imbalance between early and late amplitudes. An upper limit for a given SNR is obtained by letting $A_+ = A_0$. Based on the amplitude-versus-delay plot in Fig. 5-1, the delay error in this case becomes

$$\sigma_\tau \leq k_p \frac{1.15}{\text{SNR}_x} \sqrt{2 + 0.51} \quad (7.30)$$

in units of p-chips, where 1.15 accounts for the decrease of the prompt amplitude relative to peak amplitude and 0.51 is approximately the maximum value for the normalized difference of the early and late amplitudes. Eqs. (7.4) and (7.16) have been used to convert to SNR_x , the peak 1-s SNR. Thus, an upper limit on delay error is given by

$$\sigma_\tau \leq \frac{0.67}{\text{SNR}_x} \quad (7.31)$$

in units of p-chips. The approximate k_p value of 0.37 has been assumed.

When the averaging interval has a length of N_T seconds, the error is reduced by a factor of $\sqrt{N_T}$. For a 5-min integration and the *nominal* 1-s SNR of 4.7 computed in Subsection 7.2.1, this upper limit for system-noise error in delay becomes

$$\sigma_\tau \leq \frac{0.67}{4.7} \frac{1}{\sqrt{300}} \quad (7.32)$$

or

$$\sigma_\tau \leq 0.0082 \text{ p-chip (25 cm)} \quad (7.33)$$

The corresponding lower limit on delay error (i.e., when early amplitude equals late amplitude) is about 29% smaller than this value. When computed on the basis of the aforementioned observed maximum delay SNR of 75, this nominal delay error reduces to 1.6 cm.

APPENDIX A

EXAMPLE OF A HIGHLY DIGITAL FRONT END

The front end presented in the text can be improved through greater use of digital processing to offer greater stability, lower cost, improved delay accuracy, smaller size, and less weight. As an example of a possible future improvement relative to the analog front end, therefore, a highly digital front end has been designed for the TurboRogue receiver. This appendix functionally and analytically describes for that particular front-end design the processing that takes the signal from reception at RF down to its sampled form at baseband. The proposed front end is based on downconversion sampling, a technique in which the signal is sampled at RF with a rate commensurate with a selected midband RF frequency, thereby causing that particular frequency component to be aliased to zero frequency. The spectrum surrounding the selected component is aliased to baseband as though it had been downconverted with a mixing signal having the selected frequency. In this manner, sampling and downconversion from RF are carried out in one step, avoiding the mixer and filter associated with standard downconversion. In the design proposed here, the effective LO frequencies and the final baseband sample rates are the same as those in the analog front end described in the text.

A.1 Functional Description of a Highly Digital Front End

A high-level functional block diagram of the example front end is shown in Fig. A-1. The RF signal collected by the antenna is passed through an "anti-RFI" filter that is sufficiently wide to pass both the L1 and the L2 bands. After broadband amplification, the signal is power-divided into L1 and L2 branches, and each branch is passed through a filter (defined as channel filter) centered at the appropriate L-band carrier. Width of these filters depends on the application, with narrow widths selected to provide good RFI rejection and wider widths to allow better delay calibration. (The narrower widths will also provide slightly better SNR performance because of the "oversampling effect" (Beaulieu, 1988) in the case of 1-bit sampling.) Figure A-1 is an example of a wide filter where the width is set equal to the largest advisable value, namely, the sample rate for each quadrature channel. After filtering, each channel is sign sampled (1-bit quantization) at RF at a very high rate (900.064 MHz for L1 and about 981.888 MHz for L2)

The sample points are passed to an alternate-sample demultiplexer (demux) that separates the C (defined as cosine) samples from the S (defined as sine) samples, thereby producing two data streams, each at half the original rate. A sign correction is applied to alternate samples on each stream to remove the sign flips described below. A sum-and-dump operation (22 points for L1 and 24 points for L2) is then applied to reduce the data rate to 20.456 MHz per quadrature component for both the L1 channel and the L2 channel. As a result of the sum-and-dump operation, the number of bits required to represent the samples is increased from 1 to 6. For example, sum-output values can range between -22 and +22 for the L1 channel, in principle. Since the TR baseband processor is designed to accept only two- or three-level samples, the 6-bit samples are requantized to three levels: (-1, 0, +1). This requantization requires specification of two integer discriminator values that set the decision levels for transforming each sum value to -1, 0, or +1. These discriminator values are set to values that minimize SNR loss and are consequently a function of channel bandwidth. When the largest advisable channel bandwidth is selected (e.g., 450 MHz for L2), the SNR loss due to requantization is minimized when the discriminator levels are set so that $\Sigma \leq -3 \Rightarrow -1$; $|\Sigma| < 3 \Rightarrow 0$ and $\Sigma \geq 3 \Rightarrow +1$.

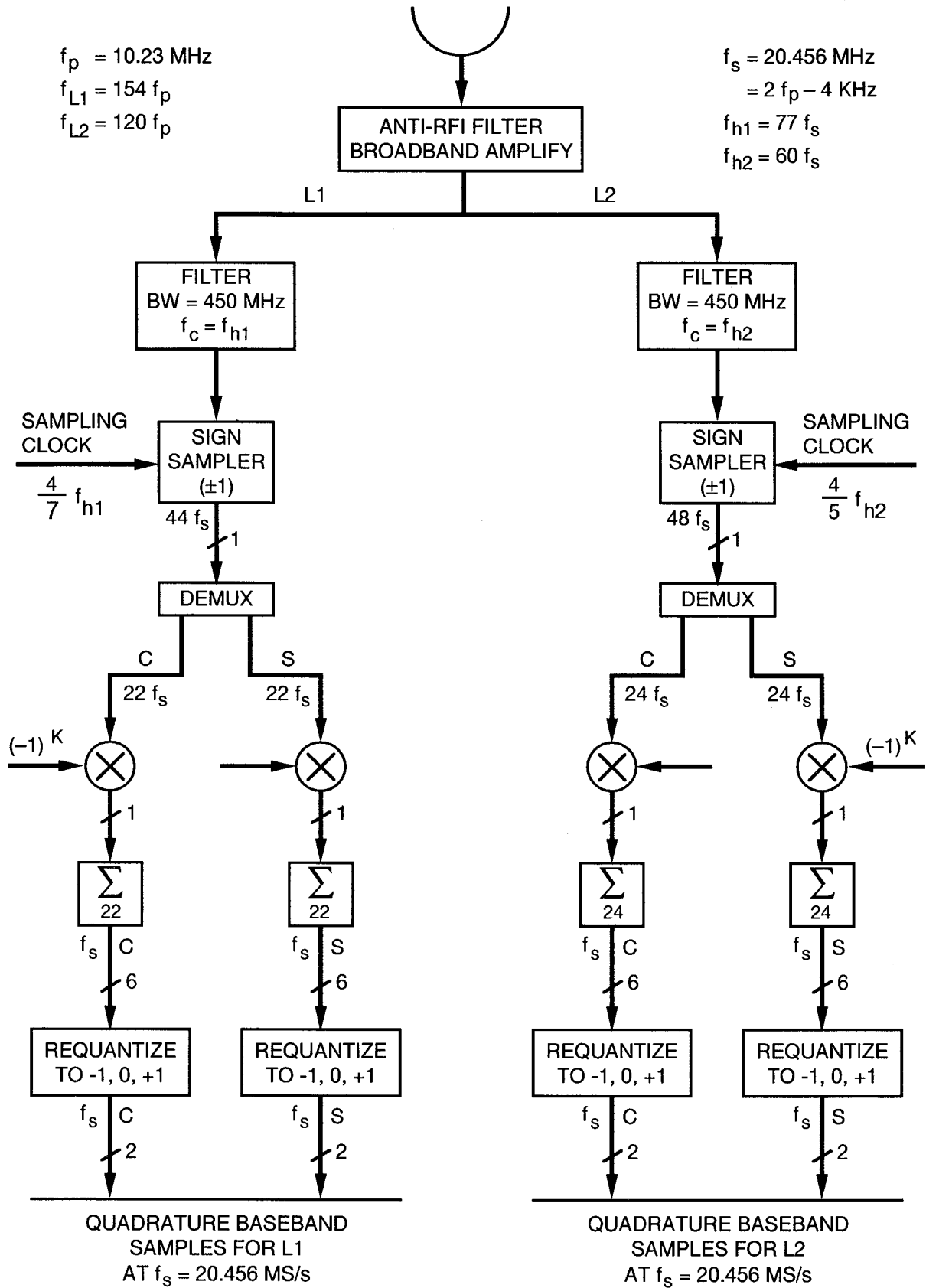


Figure A-1. Block Diagram for the Example of a Highly Digital Front End

A.2 Explanation of the Highly Digital Front End

As mentioned above, the two RF sample rates are set to values nearly commensurate with their respective carriers so that each carrier will alias to nearly zero frequency as a result of sampling. Thus, the sampling process also is a downconversion process. In addition to being nearly commensurate with the carrier, the sample rate is selected so that the sample points alternate between quadrature components of the signal.

These features of sampling downconversion are schematically illustrated in Fig. A-2 for the L2 channel. In this example, the sample clock has a rate of $F_s = 4/5 f_h$, where f_h is the desired effective downconversion frequency. (In TR, the effective downconversion frequency is close to the carrier frequency, with an offset of 308 kHz for L1 and 240 kHz for L2, as in the analog front end.) Figure A-2 shows the location of several sample points on a sinusoid with a frequency of f_h . For that particular frequency, the alternate points labeled "C" for cosine all have the same amplitude value except for an alternating sign flip. Thus, after a correction for the sign flips, the C samples for the f_h component are equal to a constant or, as commonly described, alias to zero frequency. The same observations can be made for the indicated alternate sine ("S") points. Figure A-2 also illustrates the quadrature relationship of alternate points. Note that adjacent C and S points differ by a quarter of a cycle in the fractional cycle. This relative phase of a quarter cycle reveals the quadrature relationship between pairs of adjacent sample points, as mathematically shown in the next subsection (A.3). In this manner, RF sampling produces the two quadrature channels as interleaved samples.

A similar graphical analysis can be applied to a frequency component displaced from f_h . For the (zero-Doppler) carrier frequency f_L , for example, such an analysis would show the sample points shifting in phase relative the cycle boundaries in a way that makes the frequency based on observed sample values appear to be $f_L - f_h$. Thus, all frequency components in the sampled band will effectively be lowered in value by f_h . A schematic illustration of the frequency-domain consequences of sampling downconversion is shown in Fig. A-3. (This figure neglects the distortion inflicted on the noise spectrum by the subsequent two-level amplitude quantization described below.) Note that this method results in a so-called "double-sideband" downconversion, in which half of the baseband spectrum has negative frequency. These characteristics of sampling downconversion are demonstrated mathematically in the next subsection.

As implied by Fig. A-1, the frequency subsystem has to generate only three frequencies, the ultimate baseband sample rate (commonly referred to as sample clock) of $f_s = 20.456$ MHz and two RF sample clocks obtained by simple multiplication of f_s : $F_s = 44f_s$ for L1 and $48f_s$ for L2. As in the analog front end, f_s is offset from 20.46 MHz by 4 kHz in order to ensure effective incommensurability with the P chip rate. Also paralleling the analog implementation, the 4-kHz offset produces an offset in both of the effective downconversion frequencies (relative to the zero-Doppler carrier). Again, the three required offsets can all be changed by one adjustment in f_s , without changing any multipliers.

The example implementation shown in Fig. A-1 assigns each channel filter the largest advisable width, namely a width approximately equal to the RF sample rate per quadrature channel. In selecting these filter widths, one finds that there is a trade-off between RFI rejection and receiver-induced errors in phase and delay. If the L1 filter width is reduced from 450 MHz to 50 MHz, for example, then the effects of RFI outside that 50-MHz band will be greatly reduced. (In addition, subsequent oversampling at a 450-MHz rate would help to recover some of the SNR loss caused by two-level quantization.) Accuracy, on the other hand, would be degraded, since analog filters introduce errors and instabilities in phase and delay that increase as bandwidth decreases. Such errors can be reduced by stable designs and calibration, but they can

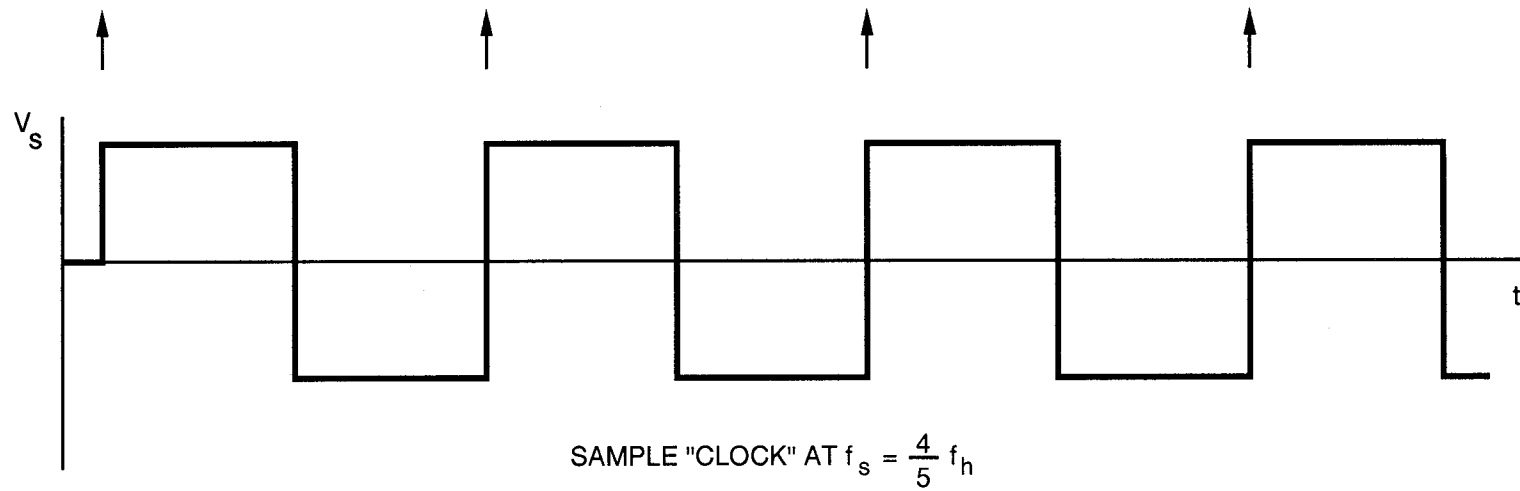
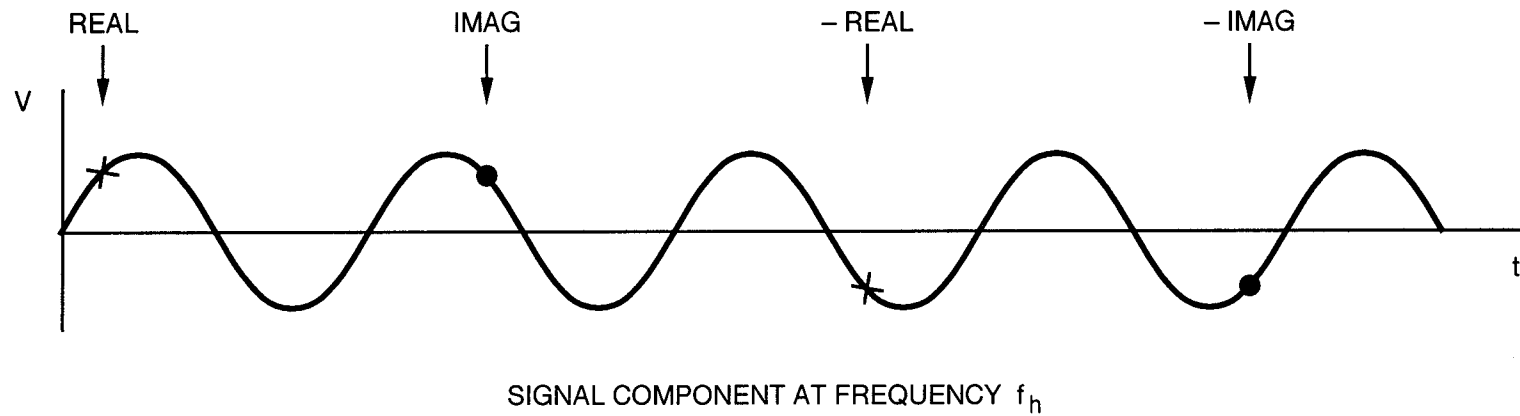


Figure A-2. Schematic Illustration of Quadrature Sampling Downconversion of a Sinusoid

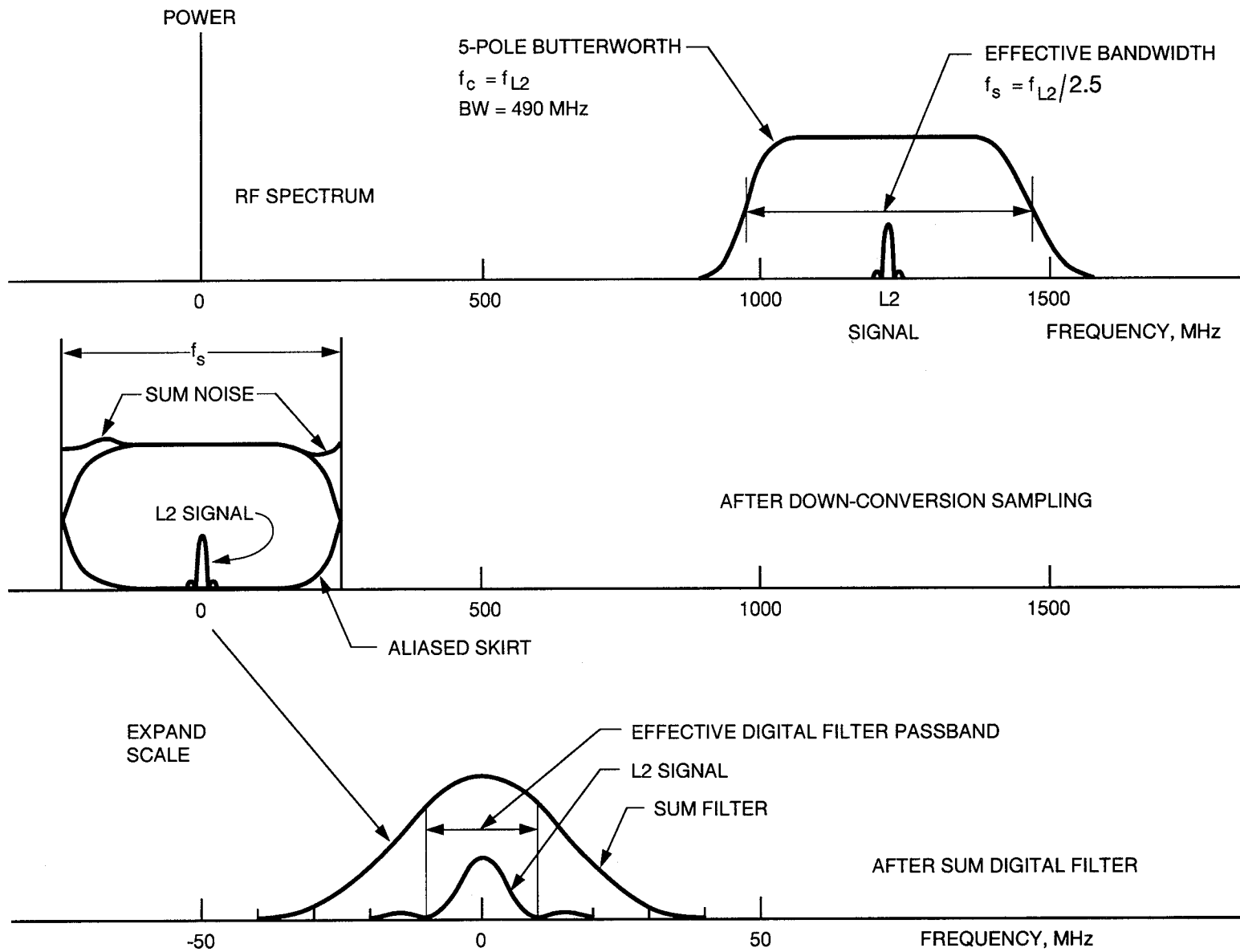


Figure A-3. Schematic Illustration of Sampling Downconversion in the Frequency Domain

be more reliably reduced by increasing the bandwidth. For example, the delay through a 450-MHz Butterworth filter is a few nanoseconds, depending on the number of poles. Given the reasonable goal of 5% calibration and stability, one could reduce the channel-filter delay error to the order of 0.2 ns. In contrast, the delay error would be about nine times larger for a 50-MHz filter.

A.3 Mathematical Model for Sampling Downconversion

This subsection presents a mathematical formulation of the sampling downconversion process outlined in the previous subsections. After application of the antenna filter and the complex channel filter, G_C , to the received signal in Eq. (2.19), the RF voltage becomes

$$V_F(t) = e^{2\pi i(f_L t - f_L \tau)} \int_{-\infty}^{\infty} G_C(v_d) G_A(v_d) G_S(f) A_p(f) e^{2\pi i[f(t-\tau) + \varphi_s + \varphi_e]} df + c.c. + \eta_F \quad (A.1)$$

where η_F is the RF noise passed by the channel filter and where the argument, v_d , given by Eq. (3.3), is the Doppler-shifted frequency component at RF corresponding to f . The carrier factor has been pulled outside of the integral so that it can be reformulated in a manner that anticipates downconversion:

$$V_F(t) = e^{2\pi i[f_h t + (f_L - f_h)t - f_L \tau]} \int_{-\infty}^{\infty} G_C(v_d) G_A G_S(f) A_p(f) e^{2\pi i[f(t-\tau) + \varphi_s + \varphi_e]} df + c.c. + \eta_F \quad (A.2)$$

where f_h is the anticipated effective downconversion frequency for either L1 or L2 as discussed in the preceding subsection and as defined in Fig. A-1.

The next step in processing is to sign-sample each of the two channels at RF. Following the analysis in Subsection 3.3 for sign sampling in the analog front end, one obtains the following expression for a sample after an ensemble average over noise:

$$\langle \tilde{V}_F(t_{rk}) \rangle_{\eta} \approx \frac{q_M}{\sigma_{\eta}} e^{2\pi i[f_h t_{rk} + (f_L - f_h)t_{rk} - f_L \tau]} \int_{-\infty}^{\infty} G_C(v_d) G_A G_S(f) A_p(f) e^{2\pi i[f(t_{rk} - \tau) + \varphi_s + \varphi_e]} df + c.c. \quad (A.3)$$

where t_{rk} represents the k th sample time according to the RF sampler clock. The approximately equal sign denotes the neglect of the higher order terms produced by sign sampling, as discussed in Appendix B of this document. For the example design in Fig. A-1, omission of the higher order terms is an excellent approximation since the wide noise bandwidth results in a very small single-sample SNR (e.g., $S/\sigma < 0.04$). Again, delay has been redefined, as in Eq. (3.7), to incorporate the sampler clock error that enters when true time is replaced with sampler time.

Only the L2 samples will be analyzed in detail since the L1 analysis follows an identical course. In the proposed implementation, the RF sample rate for L2 is $4/5 f_h$. The sample rate becomes 981.888 MHz since $f_h = 60 * 20.456$ MHz. The sample times can be represented in terms of this sample rate by

$$t_{Rk} = k \frac{5}{4} \frac{1}{f_h}, \quad k = 1, 2, 3, \dots \quad (\text{A.4})$$

These sample times will be separated into alternate points:

$$t_{Rn}^c = 2n \frac{5}{4} \frac{1}{f_h} \quad (\text{A.5})$$

and

$$t_{Rn}^s = (2n-1) \frac{5}{4} \frac{1}{f_h} \quad (\text{A.6})$$

in which $n = 1, 2, 3, \dots$, and where the superscript C denotes cosine (real component) and the superscript S denotes sine (imaginary component).

For the C samples, t_{Rk} is replaced with t_{Rn}^c in Eq. (A.3) to yield

$$\begin{aligned} \langle \tilde{V}_F(t_{Rn}^c) \rangle_{\eta} &\approx \frac{q_M}{\sigma_{\eta}} e^{2\pi i [2.5n + (f_L - f_h)t_{Rn}^c - f_L \tau']} \int_{-\infty}^{\infty} G_C(v_d) G_A G_S(f) A_p(f) e^{2\pi i [f(t_{Rn}^c - \tau') + \phi_s + \phi_e]} df \\ &+ \text{c.c.} \end{aligned} \quad (\text{A.7})$$

which can be rewritten as

$$\begin{aligned} \langle \tilde{V}_F(t_{Rn}^c) \rangle_{\eta} &\approx (-1)^n \frac{q_M}{\sigma_{\eta}} e^{2\pi i [(f_L - f_h)t_{Rn}^c - f_L \tau']} \int_{-\infty}^{\infty} G_C(v_d) G_A G_S(f) A_p(f) e^{2\pi i [f(t_{Rn}^c - \tau') + \phi_s + \phi_e]} df \\ &+ \text{c.c.} \end{aligned} \quad (\text{A.8})$$

where τ' and ϕ_e are evaluated at time t_{Rn}^c . Thus, except for a sign flip on alternate samples, the carrier of the C samples is effectively downconverted by frequency f_h , as indicated by the disappearance of the $f_h t$ term in phase. After the receiver removes the sign flip, the C samples can be rewritten as

$$\langle \tilde{V}_F(t_{Rn}^c) \rangle_{\eta} \approx 2 \frac{q_M}{\sigma_{\eta}} \int_{-\infty}^{\infty} \text{Re} \left[G_C(v_d) G_A G_S(f) A_p(f) e^{2\pi i [(f_L - f_h)t_{Rn}^c - f_L \tau' + f(t_{Rn}^c - \tau') + \phi_s + \phi_e]} \right] df \quad (\text{A.9})$$

where $\text{Re}[\]$ denotes real component.

In a similar fashion, one can show that the S samples are given by

$$\begin{aligned} \langle \tilde{V}_F(t_{Rn}^s) \rangle_\eta &\approx (-1)^n \frac{q_M}{\sigma_\eta} e^{2\pi i [(f_L - f_h)t_{Rn}^s - f_L \tau' - 1.25]} \int_{-\infty}^{\infty} G_C(v_d) G_A G_S(f) A_p(f) e^{2\pi i [f(t_{Rn}^s - \tau') + \varphi_s + \varphi_e]} df \\ &+ \text{c.c.} \end{aligned} \quad (\text{A.10})$$

where τ' and φ_e are evaluated at time t_{Rn}^s . Since sign flips, $(-1)^n$, are removed in processing and since

$$e^{2\pi i (-1.25)} = -i \quad (\text{A.11})$$

Eq. (A.10) becomes

$$\langle \tilde{V}_F(t_{Rn}^s) \rangle_\eta \approx 2 \frac{q_M}{\sigma_\eta} \int_{-\infty}^{\infty} \text{Im} \left[G_C(v_d) G_A G_S(f) A_p(f) e^{2\pi i [(f_L - f_h)t_{Rn}^s - f_L \tau' + f(t_{Rn}^s - \tau') + \varphi_s + \varphi_e]} \right] df \quad (\text{A.12})$$

where $\text{Im}[\]$ denotes imaginary part.

Except for the small separation of the C and S sample times, Eqs. (A.9) and (A.12) are the real and imaginary parts of the same quantity. This time separation, Δt_F , is equal in magnitude to the sample spacing at the initial RF sample rate ($f_s = 4 f_h / 5 = 48 * 20.456$ MHz for L2) and is close to a nanosecond (about 1.0184 ns for L2) for the proposed implementation. As shown in the next two paragraphs, the effect of the time difference is negligible in carrier phase and is known and removable in group delay. Thus, when the samples represented by Eqs. (A.9) and (A.12) are combined as a complex number, they can be regarded as a complex sample of the baseband signal, with a sample rate of $24 * 20.456$ MHz per quadrature component for L2.

The effects of the time separation of the C and S components can be modeled as follows: The carrier phase terms in the S-sample expression in Eq. (A.12) are defined by

$$\varphi_c(t_{Rn}^s) \equiv (f_L - f_h)t_{Rn}^s - f_L \tau'(t_{Rn}^s) + \varphi_s(t_{Rn}^s) + \varphi_e(t_{Rn}^s) \quad (\text{A.13})$$

and can be rewritten in terms of the C-sample times as

$$\varphi_c(t_{Rn}^s) \approx \varphi_c(t_{Rn}^c) - \Delta\varphi_F \quad (\text{A.14})$$

where the S "phase error" is given by

$$\Delta\varphi_F \equiv (f_L - f_h - f_L \tau' + \varphi_s + \varphi_e) \Delta t_F \quad (\text{A.15})$$

Since f_h is offset by 240 kHz from the carrier for the L2 channel, since the maximum Doppler shift for an Earth-orbiting satellite is on the order of 50 kHz, and since the maximum ionosphere rate is on the order of 1 Hz at L band, this phase error for L2 is bounded by

$$\Delta\varphi_F < (240 \text{ kHz} \pm 50 \text{ kHz} \pm 1 \text{ Hz}) \times 1 \text{ ns} \quad (\text{A.16})$$

which gives the upper limit

$$|\Delta\phi_F| < 3 \times 10^{-4} \text{ cycles (0.07 mm)} \quad (\text{A.17})$$

Note that this phase error is nearly constant, with a time-varying component on the order of $50 \text{ kHz} \cdot 1 \text{ ns} = 50 \mu\text{cyc} = 0.012 \text{ mm}$ or less. A similar negligible error characterizes the L1 channel. Thus, the C and S samples are essentially simultaneous with respect to phase.

The terms in the phase of Eq. (A.12) that can potentially effect measured group delay can be rewritten in terms of C-sample times as

$$t_{Rn}^s - \tau'(t_{Rn}^s) \approx t_{Rn}^c - \tau'(t_{Rn}^c) - \Delta\tau_F \quad (\text{A.18})$$

where the S "delay error" is given by

$$\Delta\tau_F \equiv (1 - \dot{\tau}') \Delta t_F \quad (\text{A.19})$$

Since maximum delay rate is on the order of $40 \mu\text{s/s}$ for the extreme case of an Earth-orbiting receiver, the contribution of the delay-rate term to this error is negligible (on the order of 4×10^{-14} seconds). Thus, the S delay error is a constant bias equal to the sample spacing ($\sim 1 \text{ ns}$). This is the delay error that would be present in the S data if one processed the S samples as though they had been recorded at the C-sample times. As explained below, the C and S sample pair is processed as though both components were recorded at the C sample time. The single delay value that is extracted from this combined data will be an average of the C-sample delay and the biased S-sample delay. Consequently, the measured delay will be offset from "true delay" by a constant bias equal to $\Delta\tau_F/2$ (0.5555 ns for L1 and 0.5092 ns for L2). In applications involving extremely accurate clock synchronization, this delay bias might be important, but it can be accurately corrected, if necessary. In applications using double differencing to remove receiver "clock" effects, this error differences out and is of no consequence.

The above analysis shows that C and S sample pairs can be processed as simultaneous quadrature samples at time t_{Rn}^c , provided a small, accurately known delay correction is applied to measured group delay after the data is processed. Thus, in the analysis that follows, adjacent C and S samples will be modeled as simultaneous quadrature samples. A composite expression for the complex sampled signal is obtained by replacing t_{Rn}^s by t_{Rn}^c in Eq. (A.12) and forming a complex quantity with the real part occupied by Eq. (A.9) and the imaginary part occupied by the adjusted version of Eq. (A.12). Such a combination yields

$$\langle \tilde{V}_F(t_{Rn}^c) \rangle_{\eta} = \frac{q_M}{\sigma_{\eta}} \int_{-\infty}^{\infty} G_C(v_d) G_A G_S(f) A_p(f) e^{2\pi i [(f_L + f)(t_{Rn}^c - \tau') + \phi_s + \phi_e - \phi_h]} df \quad (\text{A.20})$$

where the factor of two has been absorbed in the receiver filter term G_C . The downconversion phase containing f_h has been placed in ϕ_h , as defined in Eq. (3.1), but evaluated at time t_{Rn}^c with ϕ_{hd} set equal to zero.

By comparing Eq. (A.20) and Eq. (3.6), one sees that sampling downconversion can produce a sampled signal that has the same basic form as a signal subjected to the analog downconversion, filtering, and sampling described in Subsection 3.3. In the proposed sampling

downconversion approach, however, the **noise bandwidth** and the sample rate are much larger (e.g., 490.944 MHz per component for L2 versus 20.456 MHz). The next subsection models the sum-and-dump operation used to reduce the high initial data rate to 20.456 MHz.

A.4 Mathematical Model for the Sum-and-Dump Operation

The sum-and-dump step compresses successive groups of N_R points (22 for L1 and 24 for L2) to one point using the operation

$$\tilde{V}(t_R) \equiv \sum_{k=0}^{N_R-1} \tilde{V}_F(t_{Rk}^c) \quad (\text{A.21})$$

where t_R is the center of the sum interval. The average value of this sum is found by taking an ensemble average over noise:

$$\langle \tilde{V}(t_R) \rangle_{\eta} = \sum_{k=0}^{N_R-1} \langle \tilde{V}_F(t_{Rk}^c) \rangle_{\eta} \quad (\text{A.22})$$

Next, represent time relative to interval center, t_R , by

$$t_{Rk}^c = t_R + (k - N_R/2 + 1/2)s' \quad (\text{A.23})$$

where s' is the RF sample separation given by $s' = 2/F_s$ (approximately 2 ns). Now expand the time-dependent phase quantities in Eq. (A.20) about center time to obtain

$$\begin{aligned} (f_L + f)(t_{Rk}^c - \tau') + \varphi_s + \varphi_e - \varphi_h &\approx \\ [f_L + f][t_R - \tau'(t_R)] + \varphi_s(t_R) + \varphi_e(t_R) - \varphi_h(t_R) + f_d[k - N_R/2 + 1/2]s' &\quad (\text{A.24}) \end{aligned}$$

where f_d is the Doppler-shifted baseband frequency defined in Eq. (3.4). When Eq. (A.20) and (A.24) are substituted in Eq. (A.22) and the sum and integral interchanged, one can show

$$\langle \tilde{V}(t_R) \rangle_{\eta} = N_R \frac{q_M}{\sigma_{\eta}} \int_{-\infty}^{\infty} G_R(f_d) G_A G_S(f) A_p(f) e^{2\pi i [(f_L + f)(t_R - \tau') + \varphi_s + \varphi_e - \varphi_h]} df \quad (\text{A.25})$$

where all phase terms are now evaluated at time t_R and where the receiver filter is defined for this implementation by

$$G_R(f_d) \equiv G_C(v_d) \frac{\sin[N_R \pi f_d s']}{N_R \sin[\pi f_d s']} \quad (\text{A.26})$$

The relation

$$\sum_{k=0}^{N_R-1} e^{2\pi i f_s (k - N_R/2 + 1/2)} = \frac{\sin[N_R \pi f_s]}{\sin[\pi f_s]} \quad (\text{A.27})$$

has been used to evaluate the sum over time.

The sum over N_R samples increases the range of sample values from two possible values (-1 and +1) to $-N_R$ to $+N_R$, thereby increasing the number of bits required to represent a sample from 1 to 6. Since the TR digital signal processor will only accept two- or three-level quantization, the sum output is requantized to three levels (-1, 0, +1), as described in Subappendix B.1.4. In the low-SNR limit that applies to TR processing, this requantization does not change the ensemble-averaged form for the signal found in Eq. (A.25), except for a scale factor. Three-level requantization causes a loss in voltage SNR of about 10% (0.9 dB).

Note that the theoretical expression for the ensemble-averaged baseband samples is the same form for the analog front end modeled by Eq. (3.6) and the digital front end modeled by Eq. (A.25) except for a scale factor. For this reason, the analysis in the text applies directly to digital-front-end samples.

APPENDIX B

QUANTIZATION EFFECTS

B.1 Sampling Quantization

Amplitude quantization carried out during the analog-to-digital conversion of the signal can introduce distortions and decrease SNR. Two-level and three-level quantization are analyzed in this appendix.

B.1.1 Basic Principles

The complex analog voltage at baseband in Eq. (3.2) can be expressed in terms of its real and imaginary parts by

$$V = V_x + iV_y \quad (\text{B.1})$$

and in terms of signal and noise by

$$V = (S_x + \eta_x) + i(S_y + \eta_y) \quad (\text{B.2})$$

where S and η represent the signal component and noise components, respectively, with x and y denoting real and imaginary parts, respectively. The following analysis applies to both real or imaginary parts but will be labeled x .

In its ideal form, sampler quantization of voltage can be modeled by a quantization function $Q(V_x)$ that is a piecewise-constant function of input voltage V_x . Illustrations of the quantization function are shown in Fig. B-1 for two-level and three-level quantization, with quantized output voltage \tilde{V}_x plotted as a function of input voltage. Discriminator levels that determine quantization boundaries are placed at the voltage values that cause the minimum SNR loss, based on the assumptions of low single-sample SNR (e.g., <0.1) and Gaussian noise. For two-level sampling, the single discriminator level is at zero voltage. For three-level sampling, the two required levels are approximately $-0.61 \sigma_\eta$ and $+0.61 \sigma_\eta$, as illustrated in Fig. B-1 and discussed in Subsection B.1.3, where σ_η^2 is the variance of either noise component.

In the presence of Gaussian noise with a standard deviation of σ_η for each quadrature component, the expectation value for the quantized voltage at a particular sample point can be computed as

$$\langle \tilde{V}_x \rangle_\eta = \int_{-\infty}^{\infty} Q(V_x) P(V_x, S_x) dV_x \quad (\text{B.3})$$

where $\langle \rangle_\eta$ denotes the ensemble average over noise, and where the probability density function is given by

$$P(V_x, S_x) = \frac{1}{\sqrt{2\pi} \sigma_\eta} e^{-(V_x - S_x)^2 / 2\sigma_\eta^2} \quad (\text{B.4})$$

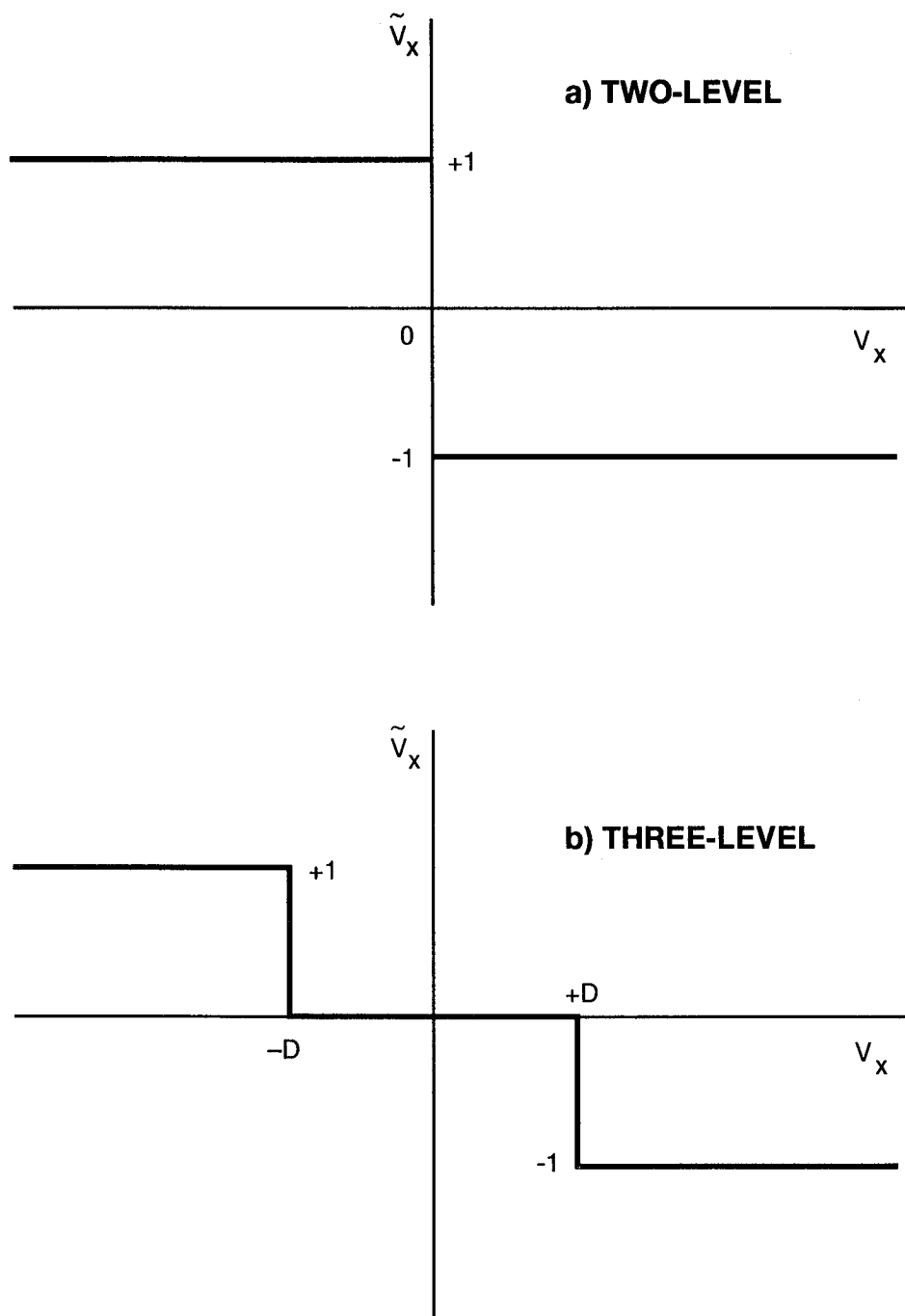


Figure B-1. Quantization Function for Two-level and Three-level Quantization

in which S_x is the value of the real component of the signal at the particular sample point under consideration. For the low single-sample SNRs, S_x/σ_η , expected for the TR receiver, the expectation value of a quantized sample is linear with respect to the signal S_x and can be approximated by

$$\langle \tilde{V}_x \rangle_\eta \approx q_M \frac{S_x}{\sigma_\eta} \quad (\text{B.5})$$

where the proportionality factor q_M is specific to the quantization function. Values for q_M are derived below for two-level and three-level quantization.

The variance of the noise on the quantized voltage is defined by

$$\sigma_{\tilde{V}}^2 \equiv \langle (\tilde{V}_x - \langle \tilde{V}_x \rangle_\eta)^2 \rangle_\eta \quad (\text{B.6})$$

which, in the case of low SNR, can be approximated by

$$\sigma_{\tilde{V}}^2 \approx \sigma_{\tilde{\eta}}^2 \equiv \langle \tilde{\eta}_x^2 \rangle_\eta \quad (\text{B.7})$$

where $\tilde{\eta}_x$ is sampled noise. Thus, the variance of the noise on the sampled voltage is approximately equal to the variance of the noise sampled without signal and is given by

$$\sigma_{\tilde{\eta}}^2 = \int_{-\infty}^{\infty} Q^2(V_x) P(V_x, 0) dV_x \quad (\text{B.8})$$

where S_x has been set to zero.

The single-sample voltage SNR after quantization is defined by

$$\text{SNR}_s \equiv \frac{\langle \tilde{V}_x \rangle_\eta}{\sigma_{\tilde{V}}} \quad (\text{B.9})$$

which is approximately given by

$$\text{SNR}_s \approx \frac{\langle \tilde{V}_x \rangle_\eta}{\sigma_{\tilde{\eta}}} \quad (\text{B.10})$$

in the low-SNR limit. Expressions for SNR are developed below for two-level and three-level quantization.

B.1.2 Two-Level Quantization

The sampler converts the filtered baseband signal to a two-level (1-bit) form, with a quantization function defined by

$$Q(V) = +1, \quad V > 0 \quad (\text{B.11})$$

$$Q(V) = -1, \quad V < 0 \quad (\text{B.12})$$

This quantization algorithm is sometimes referred to as sign sampling since the single bit representing the sample is the sign of the voltage at the sample point. When system noise greatly exceeds the signal, two-level sampling causes negligible distortion on average, of the signal component of the sampled voltage, but does decrease SNR by approximately 20%, as outlined in the next paragraph.

For two-level quantization, Eq. (B.3) reduces to

$$\langle \tilde{V}_x \rangle_\eta = \sqrt{\frac{2}{\pi}} \int_0^{\frac{S_x}{\sigma_\eta}} e^{-z^2/2} dz \quad (\text{B.13})$$

If the SNR is low (i.e., $S_x/\sigma_\eta < 1$), this integral can be expanded in the form

$$\langle \tilde{V}_x \rangle_\eta = \sqrt{\frac{2}{\pi}} \left[\frac{S_x}{\sigma_\eta} - \frac{1}{6} \left(\frac{S_x}{\sigma_\eta} \right)^3 + \dots \right] \quad (\text{B.14})$$

When SNR is so low that the S^3 term can be ignored, the sampled signal will be given on average by the linear form of Eq. (B.5) with

$$q_M = \sqrt{\frac{2}{\pi}} \quad (\text{B.15})$$

Since the quantization level is either +1 or -1, the variance of the sampled noise computed in Eq. (B.8) becomes

$$\sigma_{\tilde{\eta}}^2 \approx 1 \quad (\text{B.16})$$

Substitution of these results in Eq. (B.10) shows that the single-sample SNR after sampling is related to the SNR before sampling, S_x/σ_η , by

$$\text{SNR}_s \approx \sqrt{\frac{2}{\pi}} \frac{S_x}{\sigma_\eta} \quad (\text{B.17})$$

Thus, the voltage SNR is decreased by approximately 20% by two-level sampling.

In the strongest P channel, L1-P, the largest analog SNR, S_x/σ_η , is approximately 0.17 near maximum antenna gain (about 7 dB with the choke-ring antenna). Thus, the cubic term in Eq. (B.14) contributes less than 0.5 % to the sampled signal. Tests and theory indicate that this worst-case cubic term leads to negligible errors in phase and to less than 1-cm errors in P delays. If necessary, the S^3 delay error could be further reduced on the basis of concurrently observed SNR.

For the C/A channel, S_x/σ_η can be as large as 0.25 for the TR receiver, so that the cubic term becomes relatively large (e.g., 1% of the linear term). A calibration attempt has suggested

that the worst-case S^3 error in delay for C/A delay is less than 2 cm, but the effect was too small to measure in the attempted scheme. Again, the S^3 error in phase is negligible. In principle, a correction based on concurrently observed SNR could be applied to reduce the S^3 delay error, but such a correction is not applied in the current software.

B.1.3 Three-Level Quantization

When an analog signal is subjected to three-level sampling, the quantization function is given by

$$Q(V) = +1, \quad V > D \quad (\text{B.18})$$

$$Q(V) = 0, \quad |V| < D \quad (\text{B.19})$$

$$Q(V) = -1, \quad V < -D \quad (\text{B.20})$$

where D is a positive discriminator parameter. For this quantization function, the expectation of the sampled voltage in Eq. (B.3) reduces to

$$\langle \tilde{V}_x \rangle_\eta = \frac{1}{\sqrt{2\pi}} \left[\int_{z_U}^{\infty} e^{-z^2/2} dz - \int_{-\infty}^{z_L} e^{-z^2/2} dz \right] \quad (\text{B.21})$$

where

$$z_U \equiv \frac{D - S_x}{\sigma_\eta} \quad (\text{B.22})$$

and

$$z_L \equiv \frac{-D - S_x}{\sigma_\eta} \quad (\text{B.23})$$

Calculation of the first, second, and third derivatives of Eq. (B.21) with respect to S/σ_η leads to the expansion

$$\langle \tilde{V}_x \rangle_\eta \approx \sqrt{\frac{2}{\pi}} e^{-u^2/2} \left[\frac{S_x}{\sigma_\eta} - \frac{(1-u^2)}{6} \left(\frac{S_x}{\sigma_\eta} \right)^3 \right] \quad (\text{B.24})$$

where

$$u \equiv \frac{D}{\sigma_\eta} \quad (\text{B.25})$$

Thus, the proportionality factor in Eq. (B.5) becomes

$$q_M = \sqrt{\frac{2}{\pi}} e^{-u^2/2} \quad (\text{B.26})$$

Note that Eq. (B.24) reduces to Eq. (B.4) for $u = 0$, as one would expect. For the discriminator level that corresponds to $u = 0.612$, Eq. (B.24) becomes

$$\langle \tilde{V}_x \rangle_\eta \approx 0.662 \left[\frac{S_x}{\sigma_\eta} - 0.105 \left(\frac{S_x}{\sigma_\eta} \right)^3 \right] \quad (\text{B.27})$$

which indicates that the proportionality factor becomes $q_M = 0.662$.

Comparison of Eq. (B.27) with Eq. (B.14) indicates that the linear term is 17% smaller for three-level sampling than for two-level sampling. As shown below, this loss in amplitude is more than offset by a decrease in RMS noise. In addition, the cubic term is a factor of 1.6 less corrupting for three-level sampling, which indicates that the resulting phase and delay errors will be correspondingly lower.

For three-level sampling, the variance of the sampled noise in Eq. (B.8) reduces to

$$\sigma_\eta^2 = \frac{2}{\sqrt{2\pi}} \int_u^\infty e^{-z^2/2} dz \quad (\text{B.28})$$

When $u = 0.612$, one obtains

$$\sigma_\eta^2 = 0.5405 \quad (\text{B.29})$$

By combining the linear term in Eq. (B.27) and this estimate of noise, as prescribed in Eq. (B.10), one obtains the single-sample SNR

$$\text{SNR}_s = 0.900 \frac{S_x}{\sigma_\eta} \quad (\text{B.30})$$

This result shows that three-level sampling of an analog signal causes a voltage SNR loss of approximately 10% in the case of low SNR. Thus, as indicated by Eqs. (B.17) and (B.30), three-level sampling provides about 13% better voltage SNR (approximately 1 dB) than two-level sampling.

By using the above expressions, one can show that the assumed discriminator level of $u = 0.612$ minimizes SNR loss. Form the single-sample SNR by extracting the leading term of Eq. (B.24) and dividing by the square root of Eq. (B.28). The resulting function is maximized when u is approximately equal to 0.612.

B.1.4 Highly Digital Front End

In the highly digital front end presented in Appendix A, two-level sampling is carried out at RF at a very high rate (about 450 MS/s for L1 and about 490 for L2). The samples are then subjected to a sum-and-dump operation to reduce the rate to 20.456 MS/s and increase SNR. The sum, which covers 22 points for the L1 channel and 24 for L2, increases the number of bits required to represent a sample to a relatively high value (6 bits). To keep a minimum-bit design in the digital baseband processor, the sum output values can be requantized to three levels, -1, 0,

and +1, with the integer discriminator level set as closely as possible to the value that minimizes SNR loss. As mentioned above, the optimum discriminator level settings are approximately -0.61σ and $+0.61\sigma$ for ordinary three-level sampling of an analog voltage. Integer discriminator levels can be set in analogy with ordinary sampling. Given the RF-filter bandwidths in Fig. A-1, for example, noise is uncorrelated between samples, the RMS value for noise leaving the sum is \sqrt{N} , where N is the number of points (22 or 24) in the sum. As an approximation, therefore, the requantization discriminator parameter can be computed as $0.612\sqrt{N}$, which equals 2.871 for L1 and 2.998 for L2. These values are both rounded to 3, the nearest integer, which leads to discriminator values of -3 and +3 for both the L1 and the L2 channels, given the implementation in Fig. A-1. Since the number of points in the sum is even for both L1 and L2, all sum values are even, and only the sum values of -2, 0, +2 are requantized to zero; all other sum values become either -1 or +1.

The cubic effect introduced by the initial two-level sampling at RF is very small for both channels due to the very low single-sample SNR caused by the very wide noise bandwidth (e.g., 450 MHz) entering the RF sampler. Thus, even though the initial two-level sampling degrades the SNR by 20%, the initial 1-bit samples are, on average, essentially linear with respect to the input signal. To first approximation, the N -point sum, on average, preserves this linearity. As an approximation, therefore, the effects of integer requantization can be modeled as a three-level quantization of an analog signal with an SNR equal to the SNR of the integer samples leaving the sum. This model should closely approximate the amplitude and noise effects of requantization.

When the effects of three-level requantization are combined with the effects of the initial two-level sampling at RF, therefore, one obtains the following approximate expression for the SNR for each 20.456-MHz sample:

$$\text{SNR}_s \approx 0.900 \sqrt{\frac{2}{\pi}} \frac{S_x}{\sigma_\eta} \quad (\text{B.31})$$

where S_x/σ_η is the single-sample SNR that would have been obtained by sampling at 20.456 MHz with an "infinite" number of quantization levels, $\sqrt{2/\pi}$ is the loss due to the initial two-level sampling, and 0.900 is the loss caused by three-level requantization. The combined effect becomes

$$\text{SNR}_s \approx 0.72 \frac{S_x}{\sigma_\eta} \quad (\text{B.32})$$

Thus, the combined SNR loss due to both quantization steps in the example digital front end is about 28% in voltage SNR or 2.9 dB. If the bandwidth of the filter preceding the RF sampler is greatly reduced (e.g., from 450 MHz to 90 MHz) so that the signal is greatly oversampled, much of the SNR loss caused by the initial two-level sampling can be "regained."

In analogy with the initial two-level quantization, a cubic term is introduced by the three-level requantization. An approximate analysis will be carried out through analogy with the results presented in the preceding subsections. Since the single-sample SNR at requantization is about the same as the single-sample SNR at the point of two-level quantization in the analog front end (see Subsection B.1.3), the S^3 effect is about 1.6 times smaller for the digital front end due to the smaller coefficient of the cubic term at requantization (compare Eqs. B.14 and B.27). Thus, the S^3 error is estimated to be about a factor of 1.6 smaller for the digital front end than for the analog front end (see Subsection B.1.2).

B.2 Three-Level Quantization of Counter-Rotation Sinusoids

The model phasor of Eq. (4.2) is quantized on each component to three levels in the TurboRogue receiver. As illustrated in Fig. B-2, the quantization consists of amplitude values equal to -1, 0, or +1 with subcycle divisions of 1/8, 3/8, 1/8, 3/8 cycle. This quantized form for a sinusoid greatly simplifies the hardware but causes a slight increase in SNR. If one Fourier decomposes the three-level sinusoid, the coefficient of the fundamental (i.e., the desired counterrotation sinusoid) is 1.176, which is 17.6% higher than for an unquantized sinusoid. This increase in amplitude is canceled by greater effective noise, which increases by a factor of $\sqrt{1.5}$ (see Subappendix C.2.1). The net effect is a decrease in voltage SNR of about 4% (-0.35 dB) due to three-level quantization. Greatly reduced complexity in the hardware justifies this small sacrifice in SNR.

Higher harmonics are introduced by three-level quantization of the counterrotation sinusoids. If the baseband carrier frequency is sufficiently high, these unwanted harmonics are reduced to a negligible level by the filtering effect of the correlation sum. A high baseband frequency is produced by offsetting the downconversion frequency. For example, the L1 baseband frequency is on the order of 300 kHz, and its third harmonic is on the order of 900 kHz. This harmonic is counterrotated to about 600 kHz by the baseband processor. A 20-ms correlation sum would then reduce its amplitude by a factor greater than $2 \times 600 \text{ kHz} \times 0.02 \text{ s} = 24,000$ relative to the primary signal. At this reduced level, the third-harmonic term would introduce a phase error less than 7 μ cycles. Even greater reduction in error will result from averaging over longer time intervals (e.g., 1 s). Thus, harmonics introduced by three-level quantization are reduced to negligible levels in measured phase. It is assumed that the incoming signal has no tones at the harmonic frequencies.

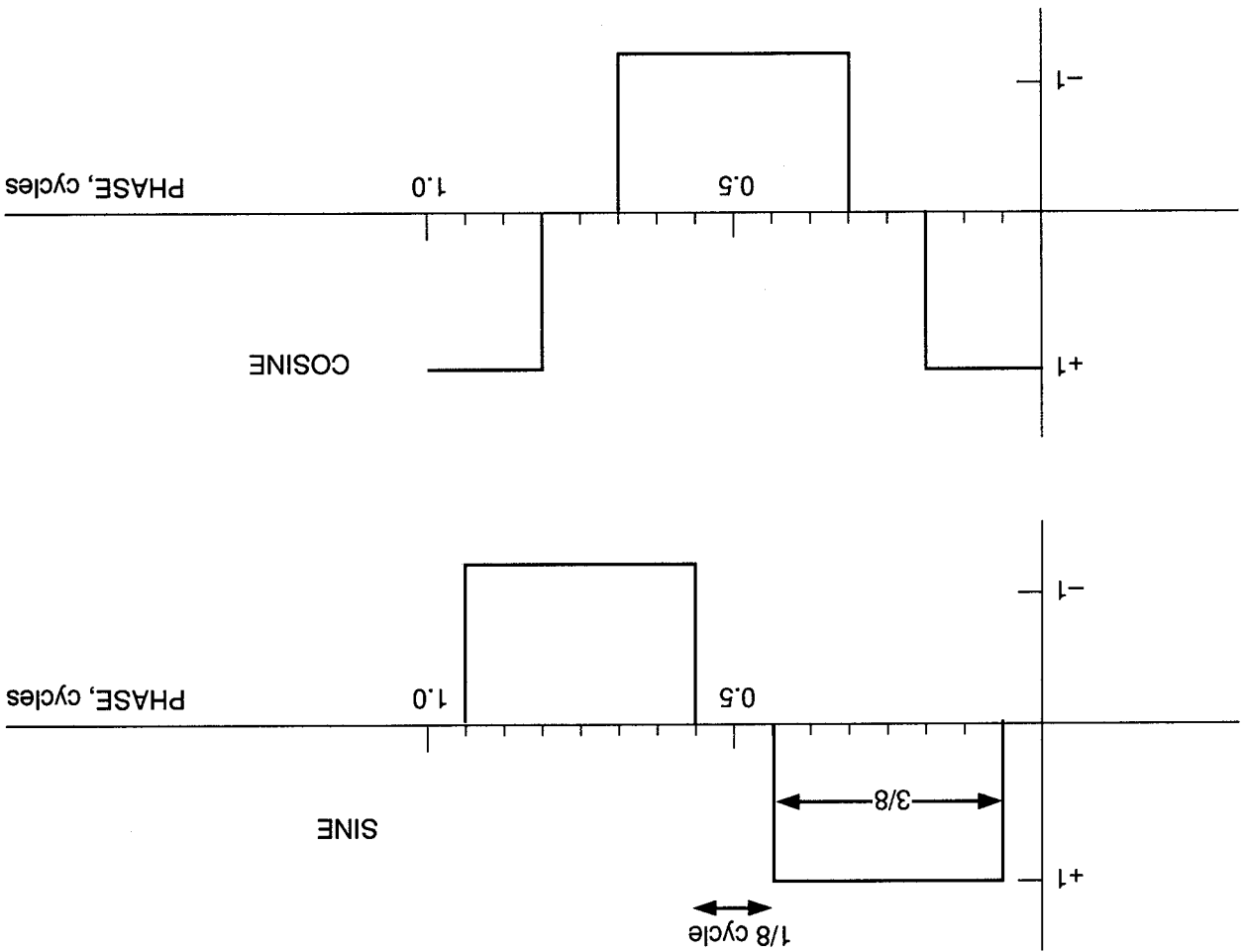


Figure B-2. The Three-level Counterrotation Sinusoids

APPENDIX C

NOISE-CORRELATION ANALYSIS

C.1 Correlation of Noise Between Samples

Let $R_\eta(\tau)$ be the analog autocorrelation function for each of the two components of the complex noise, η , on the baseband signal in Eq. (3.2). If the receiver in the ideal case is characterized by a rectangular bandpass with a two-sided bandwidth equal to W , the analog autocorrelation function of the noise produced by double-sideband downconversion will be given by

$$R_\eta(\tau) = \frac{\sin[\pi W\tau]}{\pi W\tau} \quad (\text{C.1})$$

after normalization to one at $\tau = 0$. For this ideal configuration, the sample rate f_s is equal to W in a Nyquist implementation, and the zeros of the analog autocorrelation fall at sample-interval separations of $\delta\tau = 1/W = 1/f_s$. Thus, the ideal autocorrelation function is equal to one at the origin and zero at other sample spacings, indicating that noise on a given sample is uncorrelated with the noise on any other sample. The actual bandpass is not rectangular, but the system implementation is sufficiently close to ideal to allow this model to serve as an approximation for noise analysis.

The autocorrelation function for two-level sampled noise (van Vleck and Middleton, 1966) can be expressed in terms of the analog autocorrelation function as

$$\tilde{R}_\eta(\tau) = \frac{2}{\pi} \sin^{-1}[R_\eta(\tau)] \quad (\text{C.2})$$

This relation shows that the digital autocorrelation is equal to one at the origin, with nulls at the same points as in the analog case. Thus, the noise is still uncorrelated between different samples after two-level sampling. A similar conclusion applies to three-level quantization.

As analyzed in Appendix D of this document, the two quadrature noise components are assumed to be uncorrelated with one another and to have the same noise characteristics. With these assumptions and the features of the digital autocorrelation functions described above, one can easily show that the sampled complex noise satisfies the relations

$$\langle \tilde{\eta}(t_j) \tilde{\eta}^*(t_k) \rangle_\eta = 2\sigma_{\tilde{\eta}}^2 \delta_{jk} \quad (\text{C.3})$$

$$\langle \tilde{\eta}(t_j) \tilde{\eta}(t_k) \rangle_\eta = 0 \quad (\text{C.4})$$

where the tilde denotes sampling quantization of each component and $\sigma_{\tilde{\eta}}$ is the RMS value of sampled noise for each component. Expressions for $\sigma_{\tilde{\eta}}$ can be found in Eqs. (B.16) and (B.29) for two- and three-level quantization, respectively.

C.2 Code Mode

C.2.1 Two Complementary Correlations for the Noise on the Correlation Sums

Two complementary correlations are derived to begin assessment of the noise on the complex correlation sums. The first calculation determines the complex interlag correlation

$$\rho_1(l, l') \equiv \langle (u_l - \langle u_l \rangle)(u_{l'}^* - \langle u_{l'}^* \rangle) \rangle \quad (\text{C.5})$$

and the second the complementary correlation

$$\rho_2(l, l') \equiv \langle (u_l - \langle u_l \rangle)(u_{l'} - \langle u_{l'} \rangle) \rangle \quad (\text{C.6})$$

where $\langle \rangle$ indicates an ensemble average over both noise and code.

For weak signals, the first correlation is approximated by

$$\rho_1(l, l') \approx \langle u_l u_{l'}^* \rangle \quad (\text{C.7})$$

Substituting the definition of correlation sum in Eq. (4.5), one obtains

$$\rho_1(l, l') \approx \sum_{j, k} \langle \tilde{V}(t_j) \tilde{V}^*(t_k) V_m(t_j, l) V_m^*(t_k, l') \rangle \quad (\text{C.8})$$

where, for brevity, t_k refers to $t_R + ks$. For a small single-sample SNR, the sampled voltage is mostly noise, and Eq. (C.8) becomes

$$\rho_1(l, l') \approx \sum_{j, k} \langle \tilde{\eta}(t_j) \tilde{\eta}^*(t_k) \rangle_{\eta} \langle V_m(t_j, l) V_m^*(t_k, l') \rangle_p \quad (\text{C.9})$$

where the noise and code averages have now decoupled. In the case of ideal sampling, Eq. (C.3) reduces this equation to

$$\rho_1(l, l') \approx 2\sigma_{\tilde{\eta}}^2 \sum_k \langle V_m(t_k, l) V_m^*(t_k, l') \rangle_p \quad (\text{C.10})$$

When the correlator model in Eq. (4.1) is substituted, one obtains

$$\rho_1(l, l') \approx 2\sigma_{\tilde{\eta}}^2 \sum_k |\tilde{C}(\varphi_m)|^2 \langle P(t_k - \tau_m - ls) P(t_k - \tau_m - l's) \rangle_p \quad (\text{C.11})$$

The expectation value in this equation can be expressed in terms of the P-code autocorrelation function as defined in Eq. (2.12), which yields

$$\rho_1(l, l') \approx 2\sigma_{\tilde{\eta}}^2 \sum_k |\tilde{C}(\varphi_m)|^2 R_p(t_k - \tau_m - ls, ls - l's) \quad (\text{C.12})$$

For three-level quantization, one can easily show that the magnitude of the quantized counter-rotation phasor is equal to

$$|\tilde{C}(\phi_m)|^2 = 1.5 + \text{square wave} \quad (\text{C.13})$$

where the square wave has a frequency equal to four times the carrier rate. In the sum over time, this square wave with a frequency on the order of 1.2 MHz is typically orthogonal to the autocorrelation function with its frequency of about 10.23 MHz, particularly when Doppler shifting is incorporated. Thus, Eq. (C.12) becomes

$$\rho_1(l, l') \approx 3\sigma_{\tilde{\eta}}^2 \sum_k R_p(t_k - \tau_m - ls, ls - l's) \quad (\text{C.14})$$

As indicated in Eq. (2.14), the time average of the P-code autocorrelation function is a triangle function, so that Eq. (C.14) becomes

$$\rho_1(l, l') \approx 3N_s \sigma_{\tilde{\eta}}^2 \Lambda(l - l') \quad (\text{C.15})$$

where N_s is the number of samples in the correlation sum, and Λ is the triangle function shown in Fig. 2-3.

If the counterrotation phasor were not quantized, the phasor magnitude in Eq. (C.13) would be equal to one for all time points and the coefficient in Eq. (C.15) would be 2 rather than 3. This comparison shows that three-level quantization of the counterrotation sinusoids increases the variance of the sum noise by a factor of 1.5.

Analogous to the preceding analysis, the second interlag correlation in Eq. (C.6) reduces to

$$\rho_2(l, l') \approx \sum_{j, k} \langle \tilde{\eta}(t_j) \tilde{\eta}(t_k) \rangle_{\tilde{\eta}} \langle V_m(t_j, l) V_m(t_k, l') \rangle_p \quad (\text{C.16})$$

Because of Eq. (C.4), one obtains

$$\rho_2(l, l') = 0 \quad (\text{C.17})$$

which shows that this correlation is zero for all lag combinations.

C.2.2 Interlag Correlations and RMS Sum Noise

Let x_l and y_l be the real and imaginary components of the complex sum noise, $u_l = \langle u_l \rangle$. Eqs. (C.5) and (C.15) show that averages of the products of these components satisfy the following two relations:

$$\langle x_l x_{l'} \rangle + \langle y_l y_{l'} \rangle \approx 3N_s \sigma_{\tilde{\eta}}^2 \Lambda(l - l') \quad (\text{C.18})$$

$$\langle x_{l'} y_l \rangle - \langle x_l y_{l'} \rangle \approx 0 \quad (\text{C.19})$$

while Eqs. (C.6) and (C.17) show

$$\langle x_l x_{l'} \rangle - \langle y_l y_{l'} \rangle \approx 0 \quad (\text{C.20})$$

$$\langle x_{l'} y_l \rangle + \langle x_l y_{l'} \rangle \approx 0 \quad (\text{C.21})$$

Eqs. (C.18) and (C.20) can be combined to yield

$$\langle x_l x_{l'} \rangle \approx \langle y_l y_{l'} \rangle \approx 1.5 N_s \sigma_{\tilde{\eta}}^2 \Lambda(l - l') \quad (\text{C.22})$$

while Eqs. (C.19) and (C.21) show

$$\langle x_l y_{l'} \rangle = 0 \quad (\text{C.23})$$

This last equation indicates that the noise on the complex correlation sum is uncorrelated between real and imaginary components, regardless of lag.

For $l = l'$, Eq. (C.22) leads to the result that the variance of the noise on either component of the correlation sum, which is defined by

$$\sigma_u^2 \equiv \langle x_l^2 \rangle = \langle y_l^2 \rangle \quad (\text{C.24})$$

is given by

$$\sigma_u^2 = 1.5 \sigma_{\tilde{\eta}}^2 N_s \quad (\text{C.25})$$

and is therefore the same for all lags. The RMS sampled noise $\sigma_{\tilde{\eta}}$ is given by either Eq. (B.16) or Eq. (B.29), depending on the number of quantization levels. N_s is the total number of samples in the correlation sum. As mentioned above, the factor of 1.5 represents the increase in noise variance due to three-level quantization of the counterrotation sinusoids.

For either component, the normalized correlation of noise between lags is obtained by dividing Eq. (C.22) by Eq. (C.25), which gives

$$\frac{1}{\sigma_u^2} \langle x_l x_{l'} \rangle \approx \frac{1}{\sigma_u^2} \langle y_l y_{l'} \rangle \approx \Lambda(l - l') \quad (\text{C.26})$$

Thus, the normalized correlation of the sum noise between lags is given by the triangle function obtained by autocorrelating the pure P-code (see Subsection 2.3). Consequently, the normalized correlation of noise between adjacent lags is approximately 0.5; for a lag separation of 2 or greater, the correlation is nearly zero.

C.3 P-Codeless Mode

C.3.1 Two Complementary Correlations for the Noise on the Correlation Sums

The two complementary correlations in Eqs. (C.5) and (C.6) derived above for code-mode operation must be rederived for P-codeless operation. Based on Eq. (5.1), the correlation in Eq. (C.7) becomes

$$\rho_1(l, l') \approx \left\langle \sum_{j, k} \tilde{V}_1(t_j - l s) \tilde{V}_2^*(t_j) \tilde{C}(t_j) \tilde{V}_1^*(t_k - l' s) \tilde{V}_2(t_k) \tilde{C}^*(t_k) \right\rangle \quad (\text{C.27})$$

where the ensemble average is over noise on L1 and L2 and over the P code. For brevity, t_k refers to $t_R + k s$ and l represents $L + l$. The counterrotation phasor, C , has now been explicitly labeled with the appropriate time argument instead of the corresponding phase argument. Since noise dominates in the limit of low single-sample SNR, this expression becomes

$$\rho_1(l, l') \approx \left\langle \sum_{j, k} \tilde{\eta}_1(t_j - l s) \tilde{\eta}_2^*(t_j) \tilde{C}(t_j) \tilde{\eta}_1^*(t_k - l' s) \tilde{\eta}_2(t_k) \tilde{C}^*(t_k) \right\rangle_{\eta} \quad (\text{C.28})$$

where the ensemble average is now only over noise. Separating the ensemble averages for L1 noise and L2 noise leads to

$$\rho_1(l, l') \approx \sum_{j, k} \left\langle \tilde{\eta}_1(t_j - l s) \tilde{\eta}_1^*(t_k - l' s) \right\rangle_{\eta_1} \left\langle \tilde{\eta}_2^*(t_j) \tilde{\eta}_2(t_k) \right\rangle_{\eta_2} \tilde{C}(t_j) \tilde{C}^*(t_k) \quad (\text{C.29})$$

By substituting Eq. (C.3) twice with appropriate subscripts, one obtains

$$\rho_1(l, l') \approx \sum_{j, k} 2\sigma_{\tilde{\eta}_1}^2 \delta_{j-l, k-l'} 2\sigma_{\tilde{\eta}_2}^2 \delta_{k, j} \tilde{C}(t_j) \tilde{C}^*(t_k) \quad (\text{C.30})$$

Because of the Kronecker delta functions, this expression is nonzero only when l is equal to l' , and in that case, the double sum collapses to a single sum:

$$\rho_1(l, l') \approx 4 \delta_{l, l'} \sigma_{\tilde{\eta}_1}^2 \sigma_{\tilde{\eta}_2}^2 \sum_k |\tilde{C}(t_k)|^2 \quad (\text{C.31})$$

If one uses Eq. (C.13) and assumes the square wave averages to zero, one obtains

$$\rho_1(l, l') \approx 6 N_s \sigma_{\tilde{\eta}_1}^2 \sigma_{\tilde{\eta}_2}^2 \delta_{l, l'} \quad (\text{C.32})$$

where N_s is again the number of points in the correlation sum.

In analogy with the derivation in Subsection C.2.1, one can easily show that the second correlation, ρ_2 , defined in Eq. (C.6), is equal to zero for all lag combinations, as in Eq. (C.17).

C.3.2 Interlag Correlations and RMS Sum Noise

By using Eqs. (C.17) and (C.32), and following the derivation in Subsection C.2.2, one can show that the components of the complex sum noise for L1*L2 satisfy the following relations:

$$\langle x_l x_{l'} \rangle \approx \langle y_l y_{l'} \rangle \approx 3 N_s \sigma_{\tilde{\eta}_1}^2 \sigma_{\tilde{\eta}_2}^2 \delta_{l,l'} \quad (\text{C.33})$$

and

$$\langle x_l y_{l'} \rangle = 0 \quad (\text{C.34})$$

This last equation indicates that the noise on the complex correlation sum is uncorrelated between real and imaginary components, regardless of lag. Equation (C.33) shows that the noise on the real and imaginary components of the correlation sums is respectively uncorrelated between lags and that the variance of the noise on either component of a correlation sum is given by

$$\sigma_u^2 = 3 N_s \sigma_{\tilde{\eta}_1}^2 \sigma_{\tilde{\eta}_2}^2 \quad (\text{C.35})$$

Again, the RMS sampled noise $\sigma_{\tilde{\eta}}$ is given by either Eq. (B.16) or Eq. (B.29), depending on the number of quantization levels. As in Eq. (C.25), this variance is increased by a factor of 1.5 by the three-level quantization of the counterrotation sinusoids. A factor of 2 is introduced by correlating one quadrature signal with another, as opposed to correlating a quadrature signal with a model code.

For either component, the normalized correlation of noise between lags is obtained by dividing Eq. (C.33) by Eq. (C.35), which gives

$$\frac{1}{\sigma_u^2} \langle x_l x_{l'} \rangle \approx \frac{1}{\sigma_u^2} \langle y_l y_{l'} \rangle \approx \delta_{l,l'} \quad (\text{C.36})$$

These results allow a comparison of sum-noise correlations in the P-codeless mode and code mode. Equation (C.36) shows that sum noise is uncorrelated between any two separate lags in the P-codeless mode. In the code mode, on the other hand, Eq. (C.26) shows that sum noise is uncorrelated between any two lags with a separation greater than one sample but is strongly correlated (0.5) between adjacent lags.

APPENDIX D

QUADRATURE NOISE STATISTICS

This appendix analyzes the statistics of the noise on the two quadrature components of the baseband signal, including the correlation between those components.

Analogous to Eq. (2.17), the noise at RF before filtering can be written as

$$N_R(t) = \int_0^{\infty} A_{\eta}(v) e^{2\pi i v t} dv + c.c. \quad (D.1)$$

where c.c. denotes the complex conjugate of the first term, v is the RF frequency (i.e., $f_L + f$ in Section 2), and A_{η} is the Fourier distribution of the noise at RF before any receiver filtering. Note that v instead of f is now used as the independent frequency variable. In the front-end processing that takes the signal to baseband, the noise component is subjected to the same filtering and downconversion as the signal, as modeled in Subsection 3.1. After front-end processing, the (real) RF noise in Eq. (D.1) is transformed to complex baseband noise given by

$$\eta(t) = \int_0^{\infty} G_R(v) A_{\eta}(v) e^{2\pi i [v t - \phi_h]} dv \quad (D.2)$$

where ϕ_h is downconversion phase and G_R is the complex system filter for the receiver. The same operations that transformed Eq. (2.19) to Eq. (3.2) have been applied to the noise in Eq. (D.1), except for the antenna filter. This equation implicitly assumes that sine downconversion phase is exactly 90° out of phase with the cosine phase. An offset error in sine phase can be modeled as described below.

The cosine component of the baseband noise in Eq. (D.2) can be modeled as

$$\eta_c(t) = \frac{1}{2} \int_0^{\infty} G_R(v) A_{\eta}(v) e^{2\pi i (v t - \phi_h)} dv + c.c. \quad (D.3)$$

Similarly, the sine component of the baseband noise can be modeled as

$$\eta_s(t) = \frac{1}{2} \int_0^{\infty} G_R(v) A_{\eta}(v) e^{2\pi i (v t - \phi_h + \theta)} dv + c.c. \quad (D.4)$$

where θ is a phase offset ideally equal to 0.25 cycles when the downconversion phase for the sine component is exactly 90° away from the downconversion phase for the cosine component.

The normalized cross-correlation function for the two components is defined by

$$R_x(t-t') \equiv \frac{1}{\sigma_{\eta}^2} \langle \eta_c(t) \eta_s(t') \rangle_{\eta} \quad (D.5)$$

where it is assumed that the noise power is the same for the two components and where σ_η is the RMS noise for either component. (In practice, the RMS noise can be different for the two components, but such a difference has no effect on the final result from code correlation as long as the receiver amplitude-versus-frequency and phase-versus-frequency profiles along the two component paths are the same. This insensitivity to relative gain is a consequence of two-level sampling, which makes the per-sample SNR the important quantity in TR digital signal processing.) If Eqs. (D.3) and (D.4) are substituted in Eq. (D.5) and the averaging operation and the integrals are interchanged, one obtains

$$\begin{aligned}
R_x(t-t') &= \frac{1}{4\sigma_\eta^2} \int_0^\infty \int_0^\infty G_R(v) G_R(v') \langle A_\eta(v) A_\eta(v') \rangle_\eta e^{2\pi i(vt - \phi_h + v't' - \phi_h + \theta)} dv dv' \\
&+ \frac{1}{4\sigma_\eta^2} \int_0^\infty \int_0^\infty G_R(v) G_R^*(v') \langle A_\eta(v) A_\eta^*(v') \rangle_\eta e^{2\pi i(vt - \phi_h - v't' + \phi_h - \theta)} dv dv' \\
&+ \text{c.c.}
\end{aligned} \tag{D.6}$$

where c.c. denotes complex conjugation of both of the first two terms. If the RF noise is stationary, one can show

$$\langle A_\eta(v) A_\eta(v') \rangle_\eta = 0 \quad \text{when } v, v' > 0 \tag{D.7}$$

and

$$\langle A_\eta(v) A_\eta^*(v') \rangle_\eta \approx \frac{1}{2} N_0(v) \delta(v-v') \tag{D.8}$$

where N_0 is the noise power spectrum at RF before receiver filtering. With this definition of N_0 , the total noise power at RF, including both positive and negative frequencies, is N_0W , where W is the full noise bandwidth.

When Eqs. (3.1), (D.7), and (D.8) are substituted in Eq. (D.6), one obtains

$$R_x(t-t') = \frac{1}{4\sigma_\eta^2} \int_0^\infty |G_R(v)|^2 N_0(v) \cos[2\pi(v-f_h)(t-t') - \theta] dv \tag{D.9}$$

The use of the linear form of downconversion phase in Eq. (D.9) assumes that, over a correlation interval, nonlinear time variations in downconversion phase are negligible, so that the "drift," ϕ_{hd} , disappears in the difference even when t is not equal to t' . Define the quadrature phase error $\Delta\theta$ as the deviation of the quadrature phase shift θ from 90° :

$$\theta = 0.25 + \Delta\theta \tag{D.10}$$

Eq. (D.9) can now be rewritten in terms of this phase error as

$$R_x(t-t') = \frac{1}{4\sigma_\eta^2} \int_0^\infty |G_R(v)|^2 N_0(v) \sin[2\pi(v-f_h)(t-t') + \Delta\theta] dv \quad (D.11)$$

When the quadrature channels are exactly 90° out of phase ($\Delta\theta = 0$), Eq. (D.11) shows that the two quadrature components will be uncorrelated for all values of t and t' if and only if the noise spectrum after receiver filtering is symmetric about the downconversion frequency. For example, if the noise spectrum is flat and the composite filter of the receiver is symmetric about f_h , the two quadrature components will have independent statistics, and processing both components will improve SNR by 3 dB relative to processing only one.

A similar analysis shows that the variance for either of the baseband quadrature noise components is given by

$$\sigma_\eta^2 \equiv \langle \eta_c^2 \rangle = \langle \eta_s^2 \rangle = \frac{1}{4} \int_0^\infty |G_R(v)|^2 N_0(v) dv \quad (D.12)$$

When the spectrum after receiver filtering can be approximated by a rectangle with a double-sided noise bandwidth of W , the noise variance on each quadrature component becomes

$$\sigma_\eta^2 = \frac{1}{4} |G_R|^2 N_0 W \quad (D.13)$$

The factor of 1/4 (or 1/2 for σ_η) arises from quadrature-component extraction in Eqs. (D.3) and (D.4) and is of no ultimate consequence since the same factor would enter both the signal and the noise.

Given Eq. (D.13) and the assumption of a rectangular spectrum, the correlation between quadrature components in Eq. (D.11) becomes

$$R_x(t-t') = \frac{\sin[\pi W(t-t')]}{\pi W(t-t')} \sin(\Delta\theta) \quad (D.14)$$

where it is assumed that the downconversion frequency f_h is at passband center. This result can be used to place an upper limit on quadrature phase error. For the worst case of $t - t' = 0$, the correlation is equal to $\Delta\theta$ (in radians) when $\Delta\theta$ is small. For example, to keep intercomponent correlation below 0.05, the quadrature phase error must be less than 0.05 radians (about 3 degrees).

When the digital front end discussed in Appendix A is analyzed, one finds by a similar analysis that the correlation between the noise on the quadrature components can be reduced to a negligible level by making the composite bandpass, including digital filtering, symmetric about the effective downconversion frequency. However, because the quadrature components are generated through sampling rather than by downconversion through use of an LO signal, quadrature phase error, $\Delta\theta$, is not a problem in the digital front end.

APPENDIX E

THE C/A CORRELATION FUNCTION

Derivation of the C/A correlation function closely parallels the derivation for P. Differences are a result of the cyclic nature of the C/A code. The spacecraft generates the C/A code at a rate of 1.023×10^6 c-chips/s by filling every millisecond with the same sequence of 1023 chips, where each 1-ms sequence begins at an integer multiple of 1 ms, GPS satellite time. The ideal unfiltered C/A code can be modeled as

$$C(t) = \int C_s(t-t') \text{III}(t') dt' \quad (\text{E.1})$$

where $C_s(t)$ is the sequence of 1023 chips. $C_s(t)$ can be represented by a form similar to Eq. (2.1):

$$C_s(t) = \sum_{j=-512}^{512} b_j B'(t-t_j) \quad (\text{E.2})$$

where B' is a function like that in Fig. 2-2, but with a width of $T_c = (1.023)^{-1} \mu\text{s}$; where the coefficients b_j are the ostensibly random chip values of -1 or $+1$, and where

$$t_j = j T_c \quad (\text{E.3})$$

Note that the center chip, 513, has been placed at $t_j = 0$. The sampling function is defined by

$$\text{III}(t) \equiv \sum_{k=-\infty}^{+\infty} \delta(t - (k + 0.5)T_1) \quad (\text{E.4})$$

where $T_1 = 1$ ms, and $\delta(t)$ is the Dirac delta function.

Paralleling the P-code derivation, the Fourier transform of the ideal C/A code over an accumulation interval of width T and center t is given by

$$A(f) = \int_{t-T/2}^{t+T/2} C(t) e^{-2\pi i f t} dt \quad (\text{E.5})$$

The Fourier transform of the single 1023 sequence is given by

$$A_s(f) = \int_{-T_1/2}^{T_1/2} C_s(t) e^{-2\pi i f t} dt \quad (\text{E.6})$$

which becomes

$$A_s(f) = T_c \frac{\sin \pi f T_c}{\pi f T_c} \sum_j b_j e^{-2\pi i f t_j} \quad (\text{E.7})$$

where t_j is at the center of the j th chip given by Eq. (E.2). The Fourier transform of the sampling function is given by

$$W(f) = \int_{-T/2}^{T/2} \text{III}(t) e^{-2\pi i f t} dt \quad (\text{E.8})$$

which becomes

$$W(f) = e^{-2\pi i f \bar{t}} \frac{\sin(N_1 \pi f T_1)}{\sin(\pi f T_1)} \quad (\text{E.9})$$

where $N_1 \equiv T/T_1$ is the number of 1023 sequences repeated over the transform interval T .

Based on the convolution theorem, the Fourier transform of the C/A code is given by

$$A(f) = A_s(f) W(f) \quad (\text{E.10})$$

so that the power spectrum becomes

$$|A(f)|^2 = |A_s(f)|^2 \left[\frac{\sin(N_1 \pi f T_1)}{\sin(\pi f T_1)} \right]^2 \quad (\text{E.11})$$

In the limit of large N_1 , one can show

$$\left[\frac{\sin(N_1 \pi f T_1)}{\sin(\pi f T_1)} \right]^2 \approx \frac{N_1}{T_1} \sum_n \delta(f - n/T_1) \quad (\text{E.12})$$

so that the power spectrum becomes

$$|A(f)|^2 \approx |A_s(f)|^2 \frac{N_1}{T_1} \sum_n \delta(f - n/T_1) \quad (\text{E.13})$$

where $A_s(f)$ is given by Eq. (E.7). Thus, the C/A power spectrum is approximately equal to the power spectrum of the 1023 sequence multiplied by a sum of delta functions that select points at multiples of 1 kHz.

The ideal, unfiltered C/A signal at RF can be represented by

$$S_1(t) = C(t) \sin(2\pi f_L t) \quad (\text{E.14})$$

From this point, modeling of spacecraft and receiver-front-end processing parallels the analysis of Subsection 2.4 and Section 3 and will not be repeated here.

Correlation analysis, however, should take into account "code noise", defined as the deviation of results from the C/A code from the results from a long random sequence. Unlike the P code, the short repetition interval and nature of the C/A code makes the long random-sequence approximation fairly inaccurate for the C/A code, at least with respect to the amplitude-vs-lag dependence of the correlation function. Since the C/A code has only 1023 separate chips for any correlation interval greater than 1 ms, one would expect the code noise effect to be much larger for C/A than for P. For example, if the C/A chips were independent of one another, C/A code noise would theoretically cause a fractional amplitude error at the early or late lag on the order of $0.5/\sqrt{1023} \approx 0.015$, on average, relative to peak amplitude, given an accumulation interval greater than 1 ms and 500-ns lags. (In practice, since the C/A code is not a truly random sequence, the magnitude of this correlation turns out to be approximately equal to either 0.03 or 0.0007, depending on the C/A sequence.) On the other hand, for the P code with 50-ns lags, the corresponding fractional amplitude error is on the order of $0.5/\sqrt{200,000} \approx 0.001$, given an 18-ms accumulation interval and 50-ns lags. Since the maximum voltage SNR obtained by TR for an 18-ms interval is about 100, the minimum fractional amplitude error due to system noise is about 0.01. Thus, while P-code self noise is very small compared to system noise and is therefore negligible, C/A-code self noise potentially can be an important error source.

To obtain a correlation function for C/A that accounts for code noise, one can perform an analysis similar to the analysis in Section 4, including an ensemble average over noise, but omitting the ensemble average over code. Such an analysis yields the following approximation for the C/A correlation function:

$$u_I(t_R) \approx A'_c e^{2\pi i \phi_d} \int_{-\infty}^{+\infty} G(f) \frac{|A(f)|^2}{T T_c} e^{-2\pi i [f(\tau_r - lb) - \phi_1]} df \quad (E.15)$$

where b is the lag-offset interval for C/A and

$$A'_c \equiv N_s T_c c_1 \frac{q_M}{\sigma_n} \frac{\sin(\pi \dot{\phi}_d T)}{\pi \dot{\phi}_d T} \quad (E.16)$$

and where the power spectrum $|A(f)|^2$ is given by Eq. (E.11). As suggested by Eq. (2.11), the product, $T T_c$, dividing $|A(f)|^2$ in Eq. (E.15), normalizes the power spectrum so that it corresponds to a $(\sin x/x)^2$ function that equals 1.0 at the origin. Note that this equation is the same as Eq. (4.22) for the P code if the normalized power spectrum corresponds to a $(\sin x/x)^2$ function.

Substitution of Eq. (E.13) in Eq. (E.15) yields

$$u_I(t_R) \approx \frac{A'_c}{T_1} e^{2\pi i \phi_d} \sum_n G(f_n) \frac{|A_s(f_n)|^2}{T_1 T_c} e^{-2\pi i [f_n(\tau_r - lb) - \phi_1(f_n)]} \quad (E.17)$$

where $f_n \equiv n/T_1$ and where the satellite-specific "1023" Fourier component A_s is given by Eq. (E.7) in terms of specific C chips. The power spectrum is again normalized to correspond to a $(\sin x/x)^2$ function that equals 1.0 at the origin. Thus, the C/A correlation function can be computed as a sum over frequency points with 1-kHz spacing. The factor of $1/T_1$, which is equal to the 1-kHz separation between frequency points, can be viewed as a replacement for df in the conversion from integral to sum.

Based on the preceding equations, one can use each satellite-specific 1023 code sequence to accurately model the effects of C/A code noise. For example, if one uses Eq. (E.13) to obtain the power spectrum of satellite 1 based on 1-ms of code, one obtains the profusion of noisy 1-kHz points shown in Fig. E-1. Based on the normalization for $|A_s(f)|^2$ shown in Eq. (E.17), this spectrum has been normalized so that the power would approach 1.0 at zero frequency, were it not for code noise. A more informative picture is gained by averaging this noisy spectrum over larger frequency bins. For an averaging interval of 35 kHz, for example, one obtains the spectra plotted in Figs. E-2(a), E-2(b), and E-2(c) for satellites 1, 15, and 22, respectively. These satellite examples each correspond to one of only three values for the code-induced fractional amplitude errors found at the early and late lags, namely, the *Butterworth-filtered* values approximately equal to -0.0007 (satellite PRNs 1, 2, 3, 4, 5, 6, 9, 10, 11, 12, 13, 14, 16, 18, 19, 20, 23, 25 through 32); $+0.0315$ (7, 15, 17, 21, 24); and -0.0318 (8, 22), with all based on "500-ns" lags. (Alternately expressed, the correlation of adjacent chips across 1023 chips is approximately equal to twice the respective values just quoted.)

The spectra in Figs. E-2(a), (b), and (c) can be substituted in Eq. (E.17) to produce the amplitude-versus-delay responses plotted in Figs. E-3(a), (b), and (c). To better display the code-induced amplitude error, however, these responses are each plotted relative to the code-noise-free response (i.e., long-random-sequence approximation) in Fig. 4-3(a). The three aforementioned fractional amplitude errors are evident at delay values of ± 0.25 c-chip ("500 ns").

For TR, C/A code noise is not a significant error source for phase and delay measurements. Code noise has a negligible effect on phase since phase is extracted from the prompt lag, where signal and model are very nearly aligned to eliminate code sign. Furthermore, given the early-minus-late algorithm for extracting C/A delay, as shown in Eq. (6.7), code noise has no effect on delay either, since it changes the amplitude of the early and late lags by the same amount. Thus, although code noise is potentially an important error source for C/A, it causes no degradation in phase and delay when TR uses the processing algorithms presented in this report.

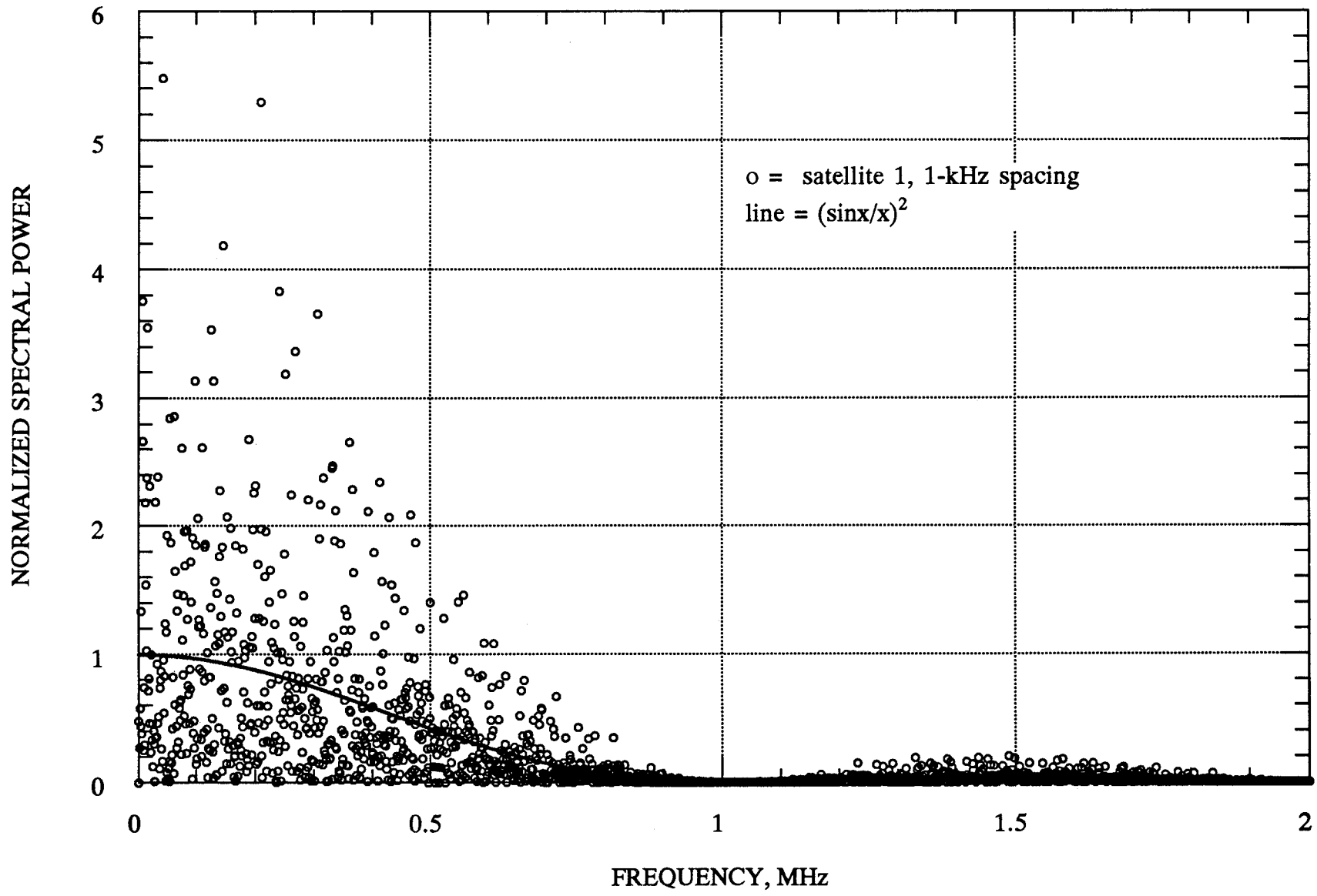


Figure E-1. Power Spectrum of the C/A Code for Satellite 1, with 1-kHz Spacing

~~E-5~~

E-5

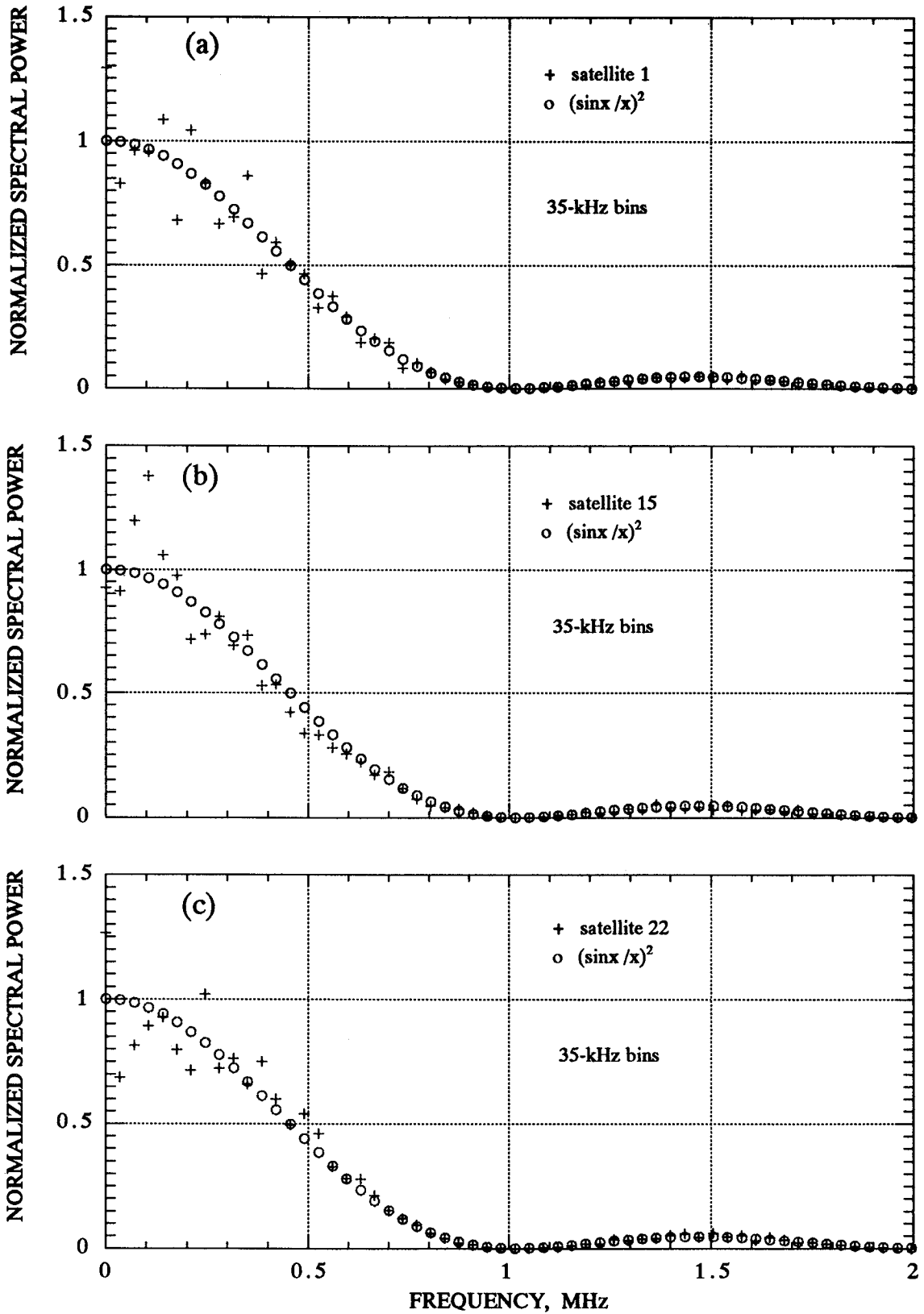


Figure E-2. Power Spectra of the C/A Code for Satellites 1, 15, and 22, with 35-kHz Resolution

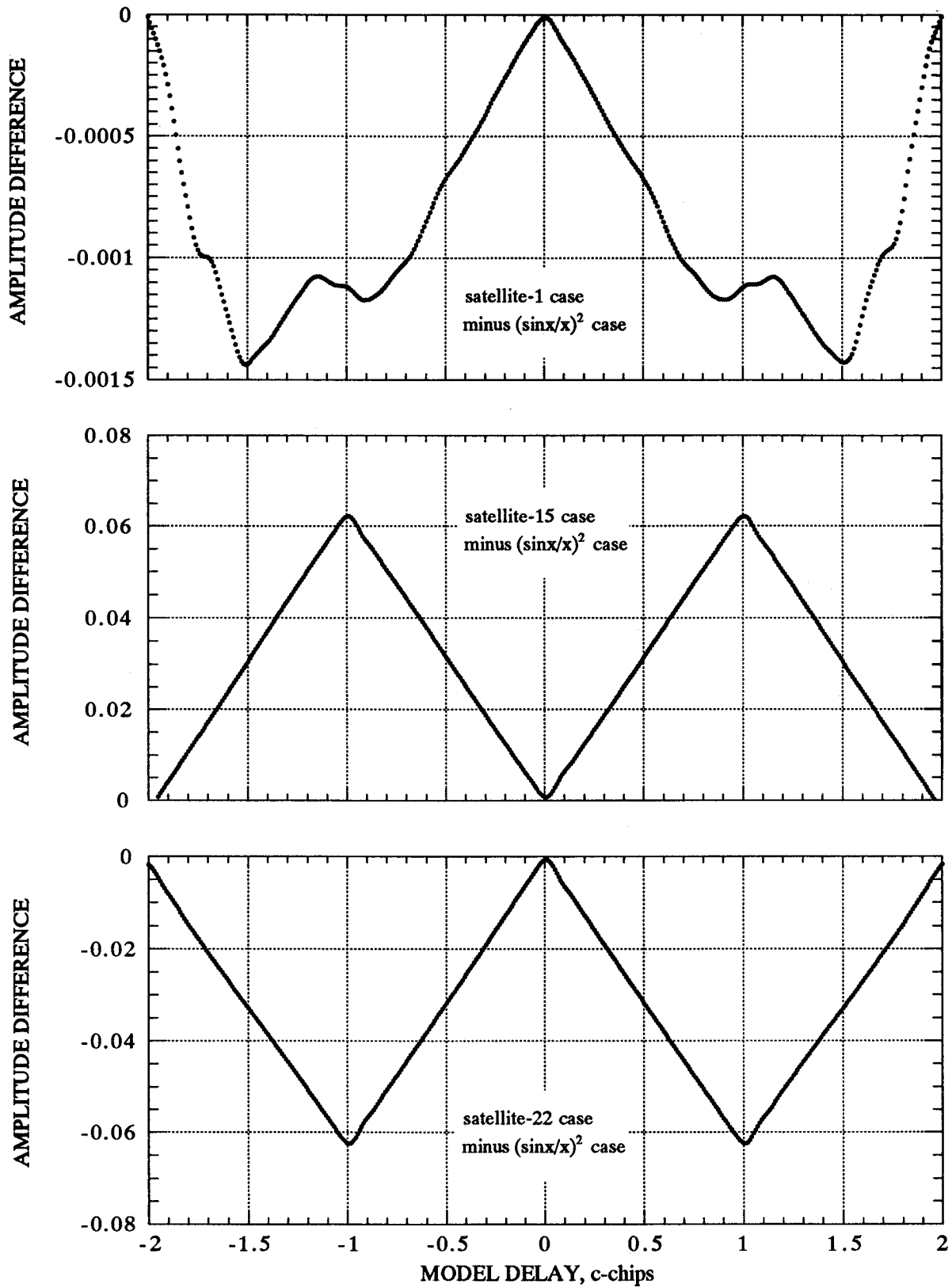


Figure E-3. C/A Correlation Amplitude versus Lag for Satellites 1, 15, and 22, Referenced to Code-Noise Free Response

REFERENCES

N. C. Beaulieu, "On the Performance of Digital Detectors with Dependent Samples," *IEEE Transactions on Communications*, vol. 36, no. 11, 1988.

C. E. Dunn, private communication, 1994.

D. J. Spitzmesser, private conversations, 1994.

J. H. van Vleck and D. Middleton, "The Spectrum of Clipped Noise," *Proc. IEEE*, vol. 54, no. 1, 1966.

TECHNICAL REPORT STANDARD TITLE PAGE

1. Report No. 95-6		2. Government Accession No.		3. Recipient's Catalog No.	
4. Title and Subtitle Signal-Processing Theory for the TurboRogue Receiver				5. Report Date April 1, 1995	
				6. Performing Organization Code	
7. Author(s) J. B. Thomas				8. Performing Organization Report No.	
9. Performing Organization Name and Address JET PROPULSION LABORATORY California Institute of Technology 4800 Oak Grove Drive Pasadena, California 91109				10. Work Unit No.	
				11. Contract or Grant No. XXXXXXXX NAS7-1260	
				13. Type of Report and Period Covered JPL Publication	
12. Sponsoring Agency Name and Address NATIONAL AERONAUTICS AND SPACE ADMINISTRATION Washington, D.C. 20546				14. Sponsoring Agency Code	
15. Supplementary Notes					
16. Abstract Signal-processing theory for the TurboRogue receiver is presented. The signal form is traced from its formation at the GPS satellite, to the receiver antenna, and then through the various stages of the receiver, including extraction of phase and delay. The analysis treats the effects of ionosphere, troposphere, signal quantization, receiver components, and system noise, covering processing in both the "code mode" when the P code is not encrypted and in the "P-codeless mode" when the P code is encrypted. As a possible future improvement to the current analog front end, an example of a highly digital front end is analyzed.					
17. Key Words (Selected by Author(s)) Electronics and Electrical Engineering, Geodesy, Geophysics, Navigation and Guidance			18. Distribution Statement Unclassified - Unlimited		
19. Security Classif. (of this report) Unclassified		20. Security Classif. (of this page) Unclassified		21. No. of Pages 94	22. Price

C-2

